Thermal emission from magnetised neutron stars

Denis González-Caniulef

Supervisors:

Prof. Silvia Zane, Prof. Kinwah Wu and Prof. Roberto Turolla (external)

Thesis submitted for the degree of

Doctor of Philosophy (PhD)

of

University College London.

Mullard Space Science Laboratory

Department of Space and Climate Physics

University College London

May 8, 2019

I, **Denis González-Caniulef**, confirm that the work presented in this thesis is my own. Where information has been derived from other sources, I confirm that this has been indicated in the Thesis.

Abstract

X-ray dim isolated neutron stars and magnetars are neutron stars with strong magnetic fields, $B \sim 10^{13} - 10^{15}$ G. Under these magnetic fields, the properties of the matter and the vacuum are expected to change dramatically. As such, these sources are (unique) natural laboratories for studying fundamental physics in the strong magnetic field regime. In this thesis, I study the polarised thermal emission from both X-ray dim isolated neutron stars and magnetars. First, I developed a ray tracing code that allows me to compute the polarisation properties of X-ray dim isolated neutron stars by considering different surface emission models and by accounting for QED vacuum birefringence effects. I show that combined optical and X-ray polarimetric observations can allow us to infer the state of the matter at the surface of X-ray dim isolated neutron stars. Then, these models are confronted with the optical VLT polarimetric observation of RX J1856.5-3754, the nearest and brightest X-ray dim isolated neutron star. I found that the observed polarisation fraction, $16 \pm 5\%$, can be explained if vacuum birefringence is present, the first ever evidence for this QED effect. In order to confirm this measurement by future missions of X-ray polarimetry, I model the polarisation properties of magnetars, active sources with outburst activity in which the X-ray flux decay is explained in the context of an untwisting magnetosphere. I show that if both vacuum birefringence and an untwisting magnetosphere are present, then during the X-ray flux decay of the source, the polarisation angle can change up to 23° (for an untwisting of $\Delta\Phi = 0.5$ rad). Finally, I model the atmosphere of magnetars heated by a particle bombardment. I compute the thermal emission in the case of a grey atmosphere and discuss the potential spectrum of the source and polarisation signal.

Acknowledgements

Firstly, I am deeply grateful to Prof. Silvia Zane for guiding my thesis. Her constant encouragement, scientific inputs, and deep involvement in my research helped me to overcome the difficulties of the PhD. Under her supervision I have learned valuable lessons, from those associated to the development of hard skills, required to approach to astrophysical problems, to the soft ones, required to communicate my research and work in collaboration. I also thank her for introducing me to large international collaborations such as the eXTP and XIPE missions. I extend my gratitude to Prof. Kinwah Wu for the number of scientific discussions, teaching, career advice and for being always available to address any question. I also thank Prof. Roberto Turolla for the all the valuable feedback provided to this research and for hosting my visit to the Department of Physics and Astronomy "Galileo Galilei" at University of Padova, Italy.

Many people have been involved in different aspect of my research. I thank Dr. Roberto Taverna for his collaboration and for many interesting scientific discussions. I also thank him for his hospitality during my visit to University of Padova. I thank Prof. Roberto Mignani and Prof. Vincenzo Testa for the collaboration on the observational study of RX J1856.5−3754, which is part of the core of this thesis. I enjoyed the collaboration with Xiaoxi Song, who visited MSSL as a UCL Dean's summer student and helped in carrying-on the research on transient magnetars.

UCL MSSL has been a great place where I have met many people to whom I am grateful. I thank the academic of the Astro group, particularly Prof. Daisuke Kawata for his advice, and Prof. Mark Cropper, who suggested me to chair the Astro Journal Club, which was a great learning experience. I also thank my fellow

student Ravindra Desai for his friendship and all the evening talks and teaching about Saturn's moon Titan which resulted in an unexpected and fruitful scientific collaboration. I would also like to thank my flatmates Georgina Graham, Mónica Tress, Zoe Vallis and Sally Dacie for the introduction to British and Mexican culture while I was living in Guildford. All of you will stay in my best memories of the UK. I also thank Jeniffer Chan, Lang Feng, Siting Xiong, and Zachry Tsiga, for the good moments that we shared in Ariel House and the Stable Block. I thank the generosity of Peter Taylor, Sam Emery, Myrto Symeonidis, Ellis Owen, Ahlam Al Qasim, and Theo Brochant De Villiers, who permanently gave me lifts to the laboratory.

I also have to mention the people from Chile that have supported me and helped me in my academic path. In my previous institution, Pontifical Catholic University of Chile, I would like to thank my former supervisor Prof. Andreas Reisenegger for his inspiring teaching and for introducing me to the research in astrophysics. I also thank him for hosting me at the Institute of Astrophysics (IA) during my visits to Chile. I extend my gratitude to Dr. Sebastien Guillot for his help and the fantastic collaboration we had on the study of PSR J0437–4715. I also thank my friends Nicolas González, for the chats about binaries and the invitations to the Argelander-Institute of Astronomy and Max Planck institute in Bonn, and Mohamed El Sheikh for the chats about physics and life in general.

This research was funded by CONICYT Becas-Chile fellowship 72150555. I also acknowledge the funding support by the Royal Astronomical Society, MSSL, COSPAR, and PHAROS, that enabled me to attend important conferences and present my work in Rome, St. Petersburg, California and multiple cities in UK.

This thesis is dedicated to my parents, María and Denis, and my sister, Gabriela. There are no words to express my gratitude for their love and support during all these years.

Impact Statement

The impact of this research can be summarized on the following levels.

- **Scientific impact:** The models developed in this research show that polarimetric observations of *X–ray dim isolated neutron stars* and *magnetars* can give us insights about the properties of matter and vacuum under super strong magnetic fields. The results of this investigation were reported in specialised journals. The models can be confronted with future *optical* and *X–ray* polarimetric observation of strongly magnetised neutron stars performed by the community of scientists working in this research field.

  In fact, during the course of this research, time was allocated to perform an optical polarimetric observation of the neutron star RX J1856.5–3754 with the *Very Large Telescope* in Chile. By comparing the theoretical models with the observation of this source it was possible to identify a potential signal of *vacuum birefringence*. The result brought the attention of the physicists/astrophysicists community as it may represent the first evidence for this *quantum electrodynamic effect*, which has been searched for by a number of experiments in terrestrial laboratories.

  A state-of-the-art model for atmospheres under particle bombardment is presented in this thesis. This work is a step forward to the development of theoretical expectations for the spectrum of magnetars, which is not yet available. This is a long sought-after goal for the community as it will allow us to perform better analysis and interpretation of the observations of these extreme astrophysical objects. In particular, this research is also relevant in view of

the next generation of space telescopes that will be able to perform spectral and polarimetric observations in the X–ray band.

- **Public impact:** The potential detection of the signal of *vacuum birefringence* mentioned above, not only brought the attention of the scientific community, but also the attention of the general public. In fact, the impact of this study is also reflected in a dedicated press coverage by ESO (European Southern Observatory). This press release was worldwide reproduced (in different languages) by magazines dedicated to communicate the latest scientific news to the broad public.

- **Future space missions:** The results of this research provided new scientific cases for future X–ray polarimetry missions. Currently, there are two missions that are planned to be launched over the next few years: IXPE and eXTP, which are under development by NASA and CAS, respectively. These missions will be operative in the $2-10$ keV band, which is suitable to observe magnetars and eventually provide a further confirmation of the signal of vacuum birefringence. Furthermore, the models developed in this research show that polarimetric observations of X–ray dim isolated neutron stars using detectors in the $0.1-0.4$ keV band can help us to infer whether these sources have a gaseous or condensed surface. These kind of observations require polarimeters able to observe very faint sources at lower energies, pushing the development of new technology.

Publications

First-authored

* **González-Caniulef D.**, Guillot S., Reisenegger A. (2019), *Neutron star radius measurement from the ultraviolet and soft X–ray thermal emission of PSR J0437–4715*, arXiv:1904.12114, submitted to MNRAS.

González-Caniulef D., Zane S., Turolla R., and Wu K. (2018), *Atmosphere of strongly magnetized neutron stars heated by particle bombardment*, MNRAS, 483, 599-613.

González-Caniulef D., Zane S., Taverna R., Turolla R. and Wu K. (2017), *Vacuum birefringence and X-ray polarimetry in transient magnetars*, Journal of Physics Conference Series, 932, 012024

González-Caniulef D., Zane S., Taverna R., Turolla R., and Wu K. (2016), *Polarized thermal emission from X-ray dim isolated neutron stars: the case of RX J1856.5–3754*, MNRAS, 459, 3585

Co-authored

Mignani R. P., Testa V., **González Caniulef D.**, Taverna R., Zane S., Wu K. and Lo Curto G. (2017), *Evidence of vacuum birefringence from the polarisation of the optical emission from an Isolated Neutron Star*, Contributed to the 13th Patras Workshop on Axions, WIMPs and WISPs, Thessaloniki, May 15 to 19, 2017, arXiv:1710.08709

Mignani R. P., Testa V., **González Caniulef D.**, Taverna R., Turolla R., Zane S. and Wu K. (2017), *Evidence for vacuum birefringence from the first optical-polarimetry measurement of the isolated neutron star RX J1856.5-3754*, MNRAS, 465, 492

* Desai R. T., Coates A. J., Wellbrock A., Vuitton V., Crary F. J., **González-Caniulef D.**, et al. (2017), *Carbon Chain Anions and the Growth of Complex Organic Molecules in Titan's Ionosphere*, ApJL, 844, L18

Turolla R., Zane S., Taverna R., **González Caniulef D.**, Mignani R. P., Testa V. and Wu, K. (2017), *A Comment on "A note on polarized light from Magnetars: QED effects and axion-like particles" by L.M. Capparelli, L. Maiani and A.D. Polosa*, arXiv:1706.02505

Taverna R., Turolla R., **González Caniulef D.**, Zane S and Wu K. (2015), *Polarization of neutron star surface emission: a systematic analysis*, MNRAS, 454, 3254

Co-authored (involvement in space missions)

eXTP mission: Santangelo A., Zane S., Feng H., Xu R., ... **González-Caniulef D.**, et al. (2017), *Physics and Astrophysics of Strong Magnetic Field systems with eXTP*, Sci. China-Phys. Mech. Astron, 60, 1

XIPE mission: Soffitta P., Bellazzini R., Bozzo E., Burwitz V., ... **González-Caniulef D.**, et al. (2016), *XIPE: the X-ray imaging polarimetry explorer*, Proceedings of the SPIE, 9905, 990515

Press coverage

First Signs of Weird Quantum Property of Empty Space? ESO press release (from *Mignani, Testa, González-Caniulef, et al., 2017*)

* New Insights into Titan's Complex Chemistry. NASA-ESA press release (from *Desai, ..., González-Caniulef, et al., 2017*)

Note: (*) paper or press coverage unrelated to the thesis.

Contents

List of Figures

List of Tables

Chapter 1

Introduction

1.1 Overview

Neutron Stars (NSs), among the most exotic objects in the Universe, are ubiquitous in the galaxies, as they are the end result of the evolution of massive stars. Their extreme physical properties make them unique tools for studying the laws of Nature: gravity in the relativistic domain, nuclear forces in ultra-dense matter and ultra-strong magnetic fields. Notably, NSs can be also primary sources of gravitational waves, as predicted by general relativity and confirmed (recently) by gravitational wave detectors. NSs are observed in almost the whole electromagnetic spectrum, from radio waves up to gamma rays. They can be found as isolated sources or with a binary companion, either in a quiescent or active state.

In particular, the study of the thermal emission from isolated, magnetised NSs holds the potential to answer key questions regarding the surface properties of these sources: what is the state of the matter in the NS surface? Do they have mainly a hydrogen, or heavier elements surface composition? What is the topology of the magnetic field in the crust and NS exterior? Even more fundamental, for NSs with measured distances, by confronting the theoretical spectrum with observations we may infer the NS radius. This, combined with measurements of the NS mass, can be used to constrain the Equation of State (EoS) of ultra-dense matter, the holy grail of NS research.

This thesis is devoted to the study of two classes of isolated NSs, from which

thermal emission is routinely observed: the X–ray Dim Isolated NSs (XDINSs) and the magnetars. The former are the best candidates to study the surface of the compact object, since they are close-by and their spectrum is purely thermal, without contamination from an active magnetosphere or a surrounding nebula. The latter are, instead, active sources with bursting activity and their spectra have a non-thermal (magnetospheric) component. Theoretical arguments and observational evidences support the idea that these sources have surface magnetic fields as strong as $B \sim 10^{13} - 10^{15}$ G. Interestingly, under those magnetic fields **a)** the properties of matter and vacuum are expected to change dramatically and **b)** quantum electrodynamics (QED) can be tested in the strong field regime. Furthermore, due to the strong magnetic field, the NS thermal emission is expected to be substantially polarised.

The aim of this thesis is to address a series of important open questions. In particular

- Can we discriminate whether the thermal emission observed from XDINSs originates in a gaseous atmosphere or in a condensed metallic surface? Is it possible to measure a potential signal of QED vacuum birefringence in XDINSs and magnetars?

- What is the thermal spectrum of a magnetar source? To which extent the surface emission is affected by their strong magnetospheric activity?

This thesis is organised as follow. In this introductory chapter I review the theory (formation, structure, cooling and rotational evolution) and observation of isolated NSs. Special emphasis is placed on the discussion of the X–ray emission detected from XDINSs and magnetars. Then, I proceed with a review of the current theoretical modelling of the thermal emission from magnetised NSs, either in the case in which an atmosphere is present or the surface is in a condensed state.

The second, third and fourth chapters are devoted to the study of the polarisation properties of the thermal emission from magnetised NSs. The aim is to investigate if polarisation measurements can provide insight about the properties of

the matter and vacuum under strong magnetic fields. In order to do that, in Chapter §2, I model the thermal emission from XDINSs in the case of gaseous atmosphere and condensed metallic surface, accounting for QED effects in the magnetised vacuum around the star. Then, in Chapter §3, theoretical models are confronted with the optical, polarimetric observation of the XDINS RX J1856.5–3754 performed with the Very Large Telescope. In Chapter §4, an extension of the models used to study the polarisation properties of the thermal emission from XDINSs is presented for the case of transient magnetars, sources in which the X–ray luminosity changes by orders of magnitude. Special emphasis is placed in the search for the signal of QED vacuum birefringence.

In Chapter §5, I study the thermal emission from the atmosphere of magnetars. In particular, I model the transport of radiation in magnetised atmosphere under a particle bombardment (from returning magnetospheric currents), accounting for the polarisation induced by the strong magnetic field. Finally, a summary of this thesis and future work is presented in Chapter §6.

1.2 Generalities about NSs

NSs are compact objects with radii $R \sim 10$ km and masses $M \sim 1.4\ \mathrm{M}_{\odot}$. They are sustained against their own strong gravity by degenerate pressure (Pauli exclusion principle forbids to fermions to be in the same quantum state). The average density of NSs, $\sim 10^{14}$ g cm^{-3}, is comparable to that of an atomic nucleus $\rho_0 = 2.8 \times 10^{14}$ g cm^{-3}. In the center, the density of NSs can be even larger, reaching several times the nuclear density, $\rho \sim (3-9)\,\rho_0$. They can also have very strong magnetic fields, up to $\sim 10^{15}$ G. Because of this, NSs are considered natural laboratories for the study of fundamental physics.

Historically, NSs were first proposed by Baade and Zwicky (1934), who suggested that these compacts objects can be formed in a supernova explosion, at the end of the stellar evolution of a massive star. They proposed the existence of NSs shortly after the discovery of the neutron (Chadwick, 1932). The rationale behind this idea was that neutrons, that do not interact electrically, could be more confined

than ordinary nuclei or electrons. Therefore, if nature's physical laws allow for the existence of very compact objects composed only by neutrons, the implosion from a normal star to a NS may provide enough gravitational energy to power a supernova event (the mechanism for supernova explosion itself was not understood and it was developed years later). Due to the observational difficulties to detect such compact objects, however, for many year NSs were considered rather a speculative idea. More than thirty years had to pass to find the first observational evidence of NSs. By performing radio observation, Hewish et al. (1968) detected a source, so called *pulsar*, producing periodical radio emission at intervals of 1.3 s. Remarkably, by the the same time Pacini (1967) and Gold (1968) developed and established the theory that explained radio pulsars as fast rotating, magnetised NSs.

1.2.1 Single stellar evolution and formation of NSs

In the theory of single stellar evolution, the precursors of NSs are massive stars, with $M \gtrsim 8M_{\odot}$ (Lyne and Graham-Smith, 1998). During main sequence, these stars convert hydrogen into helium via nuclear reactions. Once the hydrogen ends, and the star leaves the main sequence, the core begins to burn helium and convert it into carbon. This process accelerates as the core successively burns more massive nuclei up to iron group (also Ni and Co). However, since the iron nuclei have the highest binding energies per nucleon, fusion reactions involving iron group nuclei do not release energy. Then, if the star core is more massive than $\sim 1.4\,M_{\odot}$, the core contracts but neither thermal pressure nor degenerate electron pressure can stop its collapse.

As the core collapses and increases its density, the sum of the Fermi energies of an electron–proton pair is higher than the mass of a neutron. Therefore, a fast neutronisation process occurs in the core. Inverse beta decay, $p + e \rightarrow n + \nu_e$, turns a proton ($p$), and an electron ($e$), into a neutron ($n$), and a neutrino ($\nu_e$). If the mass of the core is lower than $\sim 3\,M_{\odot}$, the implosion is stopped by the pressure of degenerate neutrons, which balances the strong gravitational force. Thus, the resulting remnant of the supernova explosion is a very compact and hot NS.

The newly formed NS is not composed only by neutrons. It is known that in

vacuum neutrons are unstable and decay in ~ 15 min (mean lifetime) through a beta decay, $n \rightarrow p + e + \bar{\nu}_e$, into a proton, electron and an anti-neutrino. However, in the interior of a NS, Pauli exclusion principle stops the decay of neutrons: a neutron in fact cannot decay if the energy level for the resulting proton and electron are already occupied. Similarly, an energetic electron and proton can create a neutron only if there is a energy level available in the system. In other words, in the interior of a NS, beta and inverse beta decay are in equilibrium. This is quantified via the balance of the chemical potentials[1], $\mu_n = \mu_p + \mu_e$, of neutrons μ_n, protons μ_p, and electrons μ_e. Thus, beta equilibrium requires a fraction of charged particles to be present in the interior of the NS (Shapiro and Teukolsky, 1983). These charged particles can sustain strong electric currents in the NSs interior, leading to the wide range of magnetic field observed in the different NSs population, from $B \sim 10^8$ G up to $\sim 10^{15}$ G.

1.2.2 The structure of NSs

In order to build realistic NS models it is necessary to solve the hydrostatic equilibrium equation of the star, by considering the effects of general relativity, i.e, to solve the Tolman-Oppenheimer-Volkoff equation (Oppenheimer and Volkoff, 1939). The NS modelling also depends on the equation of state (EOS), the choice of which significantly affects the resulting NS mass–radius relationship. Basically, for building an EOS two ingredients are necessary: a model for the behaviour of the nuclear force at ultradense regimes and a numerical technique to solve the energy per particle in a many or N-body system (Lattimer, 2012). The standard model for the structure of an NS (Haensel et al., 2007) comprises four zones:

- The outer crust: this is the most external solid shell of the NS, with density lower than $\sim 10^{11}$ g cm^{-3}. It is formed by a Coulombian crystal lattice, i.e, an arrangement of nuclei forming a metal, and a relativistic electron gas. The typical thickness of the outer crust is ~ 1 km.

- The inner crust: at higher densities, electrons become ultra-relativistic and

[1] The chemical potential of neutrinos is zero.

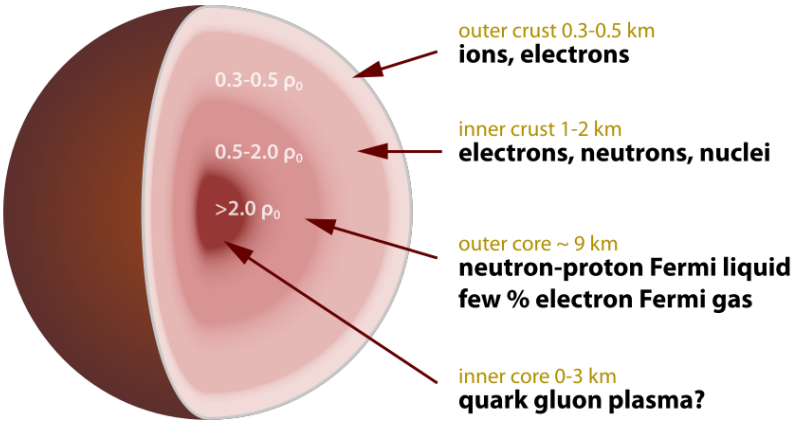

Figure 1.1: NS structure (Robert Schulze, wikimedia commons).

highly energetic. In the crystal lattice, an electron capture process produces neutron–rich nuclei. For densities above $\sim 10^{11}$ g cm^{-3} neutrons start to drip out of nuclei, and this marks the boundary between the outer and inner crust. Thus, the inner crust is composed by a neutron rich nuclei lattice that coexists with ultra-relativistic electron and a liquid of superfluid neutrons. The thickness of this shell is $\sim 1-2$ km. The outer and the inner crust contains $\sim 1\%$ of the total NS mass.

- The outer core: at densities above $\sim 0.5\rho_0$ (ρ_0 is the density of the atomic nucleus) the crystal lattice no longer exists and matter is composed by a neutron superfluid and superconductive protons together with electrons and muons. The size of this zone is several kilometres and it contains the largest fraction of the total mass of the star. Low-mass NSs, $M < 1.5\ M_\odot$, have only the outer core in their innermost region.

- The inner core: high-mass NSs, $M > 1.5M\odot$, may have an inner core. The boundary between outer and inner core is not well known. If the density of the star exceeds $\sim 2\rho_0$, for example, nucleons can be converted into hyperons and other exotic particles, such as kaons, may appear. The physics of this zone is very uncertain and the properties of the matter here are unknown.

Figure 1.1 shows a schematic view of the internal structure of an NS with the values of density and extension/size for each layer of the star. As already men-

tioned, the conditions in the NS interior, particularly those in the core, can not be reproduced in terrestrial laboratories. Therefore, the theoretical and observational study of NSs, and the determination of their mass and radius, provides a useful tool to constrain the equation of state for super-dense matter, and so a test for fundamental physics.

1.2.3 Neutron star passive cooling

The initial temperature of a newly-born NS is $T \sim 10^{11}$ K soon after the core-collapse. After that, the cooling of the NS is driven by neutrino emission from the interior of the star and photon emission from the surface of the star. The cooling is described by the thermal balance equation,

$$\dot{T} = \frac{1}{C}\left(\dot{H} - L_\gamma - L_\nu\right), \tag{1.1}$$

where C is the total heat capacity of the star, L_γ is the photon luminosity, L_ν is the neutrino luminosity, and $\dot{H}$ is the power released by some internal heating mechanism. If the NS cools down passively, with no internal heating source, the cooling can be separated in two stages. When the NS is relatively young, below 10^5 yrs, the cooling is dominated mainly by neutrino emission. After that, the cooling is dominated by photon emission from the surface.

Figure 1.2 shows the thermal evolution for a NS composed by normal matter (non-superfluid state). The cooling curves depend on the NS mass and the equation of the state assumed in the NS interior. These affect the neutrino emission and as a consequence the cooling curves. If the NS is massive with a highly dense core, a fast neutrino emission process is activated. Thus, the star cools down relatively quick (dashed lines). However, for a wide range of NS equation of states, typical NSs with $1.4M_\odot$ may cool down via a slow neutrino emission process. Figure 1.2, solid line, shows the standard cooling for slow neutrino emission. The main message here is that relatively young NSs (ages below 10^5 yrs), have temperatures above 10^6 K. This means that these sources produce most of their thermal emission in the soft X–ray band. Instead, relatively cold and old NSs (ages above 10^5 yrs),

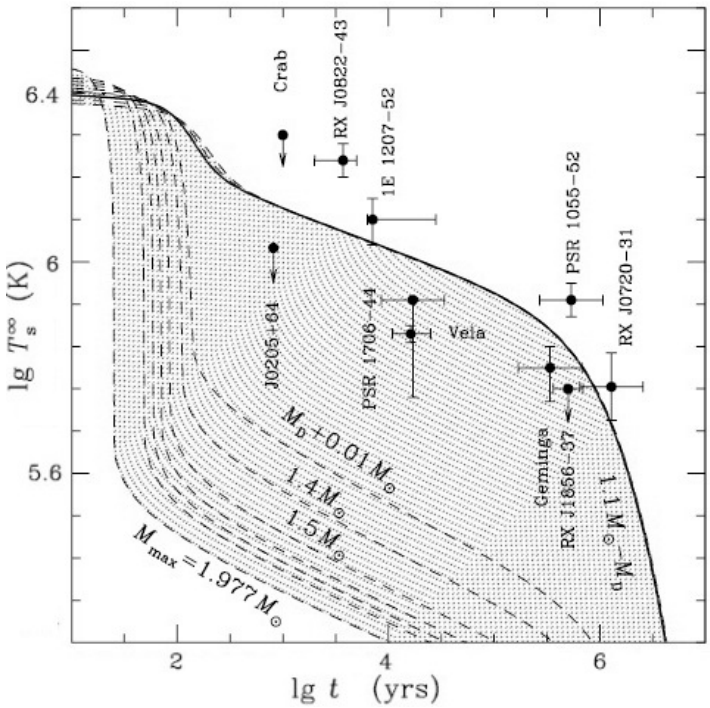

Figure 1.2: Surface temperature for an NS with interior composed of normal matter (Yakovlev and Pethick, 2004). The solid line shows the cooling considering slow neutrino emission (standard cooling model). The dashed lines show the the NS cooling for fast neutrino emission for different masses. The points with error bars show some observation of NS.

have surface temperatures below 10^6 K, which means that the peak of the thermal spectrum moves into the UV band.

1.3 Population of the Galactic NSs and the *P*-$\dot{P}$ diagram

There are $\sim$ 2300 pulsars detected in our Galaxy (see e.g., ATNF pulsar catalogue from Manchester et al. 2005). Their main characteristics can be inferred according to their position in the *P*-$\dot{P}$ diagram, where P and $\dot{P}$ are the observed period and period derivative of the pulsar, respectively. From these two quantities, the characteristic age and magnetic field strength can be inferred via a magnetic dipole model.

This approach considers the pulsar as a rotating NS in vacuo with magnetic axis disaligned from the rotational axis. The NS is radiating magnetic dipole radiation

at a rate (Shapiro and Teukolsky, 1983)

$$\dot{E} = -\frac{2}{3c^3}|\ddot{m}|^2 = -\frac{B^2R^6\Omega^4\sin^2\alpha}{6c^3}, \tag{1.2}$$

where m is the magnetic dipole moment, B is the magnetic field, R is the NS radius, Ω is the NS angular velocity, and α is the angle between the magnetic and the rotational axis of the NS. Since the source of this radiation is the rotational energy of the star, $E = I\Omega^2/2$, where I is the moment of inertia of the NS, it is possible to obtain a differential equation for Ω in the form:

$$\dot{\Omega} \propto -B^2\Omega^3. \tag{1.3}$$

Thus, from measurements of Ω and $\dot{\Omega}$, it is possible to estimate the magnetic field as $B \propto \sqrt{|\dot{\Omega}|\Omega^{-3}}$. At the same time, the integration of equation (1.3) yields (with constant magnetic field)

$$\Omega(t) = \frac{\Omega_0}{\sqrt{2k\Omega_0^2 t + 1}}, \tag{1.4}$$

where Ω_0 is the initial value of the angular velocity and $k = B^2R^6\sin^2\alpha/6Ic^3$. If the value of Ω_0 is very large compared with the current value Ω, the characteristic age of the pulsar can be estimated as

$$t_s = \frac{\Omega}{2|\dot{\Omega}|}. \tag{1.5}$$

This is commonly called spin-down age.

In Fig. 1.3 it is shown a P-$\dot{P}$ diagram with different pulsars which are clustered in different positions of the diagram. From this, it is possible to identify different NS populations such as classical radio pulsars, magnetars, XDINSs, millisecond pulsars, among others. Their main characteristics can be summarised as follows.

- **Classical pulsars or RPPs (Rotation-powered pulsars)** are located in the central region of the diagram. They have periods ranging from 30 ms up to 8 s, with period derivatives from 10^{-17} to 10^{-14} s s^{-1}. The inferred spin-down

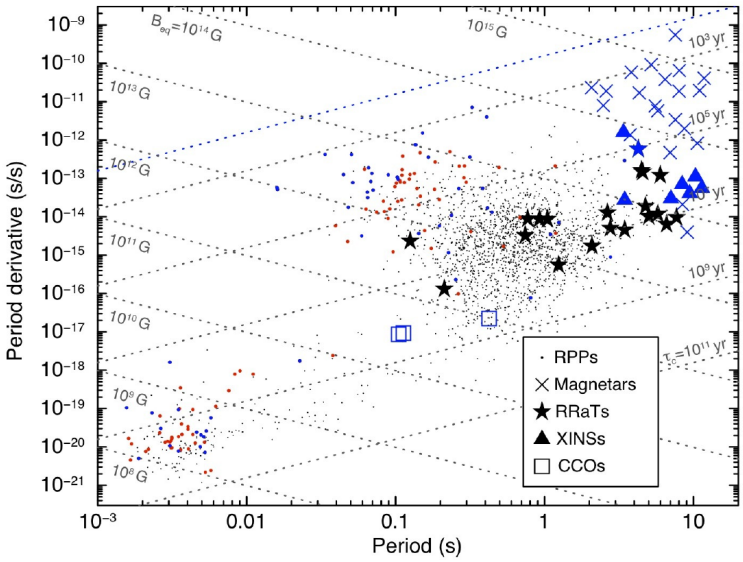

Figure 1.3: Galactic NSs P-$\dot{P}$ diagram (Turolla et al., 2015). The points correspond to the individual pulsar observations, for sources detected only at X–ray energies (red dots) or both in the radio and X–ray band (blue dots). The dotted lines show different magnetic fields, $B \propto \sqrt{P\dot{P}}$, and different spin-down ages, $t = P/2\dot{P}$, as inferred from the magnetic dipole model.

ages of these pulsars range from 10^3 to 10^8 yr and their magnetic fields are clustered around $B \sim 10^{11-12}$ G. They are the most numerous NS population with ~ 2000 sources discovered until now (Manchester et al., 2005).

- **Magnetars** are located in the upper-right corner of the diagram. They have periods between $2-12$ s and period derivatives between $10^{-13}-10^{-11}$s s^{-1}. They have characteristic spin-down ages $\sim 10^3$ yr and very strong magnetic fields, often up to $B \sim 10^{14}-10^{15}$ G. Unlike normal pulsars, magnetars in general do not produce pulsed radio emission. However, their rotational properties can be derived via their spin variability as observed in the X–ray band. Recently, magnetars with lower magnetic fields have also been discovered, together with transient magnetars and radio magnetars. Their properties and theoretical explanation are under debate (for a review see Turolla et al. 2015 and references therein).

- **X–ray dim isolated NSs (XDINSs)** are located in the middle-right side of

the diagram. They have periods $\sim 3-12$ s and period derivatives $\sim 10^{-14}-10^{-13}$s s^{-1} (Mereghetti, 2011). Their characteristic spin-down ages, $\sim 10^5-10^6$ yr, and relatively strong magnetic fields, $B \sim 10^{13}$ G, may suggest an evolutionary link with the magnetars.

- **Millisecond pulsars** are located in the bottom-left corner of the diagram. They have periods $\sim 1-10$ ms and period derivatives $\sim 10^{-21}-10^{-19}$s s^{-1}. Their inferred spin-down ages show that this population is very old, $\sim 10^9$ yr, with relatively weak magnetic fields, $B \sim 10^8$ G. Millisecond pulsars are thought to be old, normal pulsars that were recycled by accretion of matter from a binary companion. This accretion of matter produces a transfer of angular momentum and the spin up of the pulsar.

- **Central Compact Objects (CCOs)** are NSs which are located near the center of their supernova remnants (SNRs). Three of them show X–ray pulsations with periods $P = 0.1-1$ s and period derivatives $\sim 10^{-18}-10^{-16}$ s s^{-1} (Gotthelf et al., 2010; Halpern and Gotthelf, 2010, 2011). The timing solution of these objects implies relatively weak dipole magnetic fields $B \sim 10^{10}-10^{11}$ G. In turn, the characteristic spin-down age of these three objects exceeds, by 2–3 orders of magnitude, the age of the host SNRs. This information, combined with the highly non-uniform surface temperature distribution obtained from their thermal pulsations (Gotthelf et al., 2010; Bogdanov, 2014) which support the existence of magnetar-scale fields in the crust (see Shabaltas and Lai 2012 and Perna et al. 2013), suggest the presence of a hidden magnetic field under their surface, much larger than the external dipolar one.

- **Rotating Radio Transient (RRATs)** are NSs that emit erratic short radio pulses, $2-30$ ms, at intervals from minutes to hours. There are ~ 100 RRATs reported in the literature. The period derivatives obtained in 29 of them indicate magnetic fields $\sim 10^{12}$ G in most of the sources[2] (McLaughlin et al.,

[2] A catalogue can be found at http://astro.phys.wvu.edu/rratalog/

2006). Due to these relatively long periods, and since transient radio emission has been detected in some anomalous X–ray pulsars, RRATs may have a possible link with magnetars.

The historical record of the supernova explosion associated to the Crab pulsar[3] and expansion of supernova remnants for other pulsars impose other independent constraints on the age of NSs that are in rough agreement with their inferred characteristic spin-down ages. The discrepancy between the age derived from the magnetic dipole model and the observed one could be caused by other effects, such as magnetic field decay or gravitational wave emission.

The thermal and non-thermal emission observed in the various classes of Galactic NSs have different characteristics. In this thesis, we are interested in the study of magnetars and XDINS. We summarise their properties separately in the next subsections.

1.4 Magnetars

Magnetars are commonly observed as Soft Gamma Repeaters (SGRs) and Anomalous X–ray Pulsars (AXPs). The difference between these two classes of objects is historical, related to how they were discovered. Whereas SGRs were originally observed as sources emitting short and intense bursts in the hard X–ray/soft gamma-rays, AXPs were observed as X–ray pulsars in the soft X–rays. AXPs were called "anomalous" because their high X–ray luminosity $L_X \sim 10^{34} - 10^{36}$ erg s^{-1} is not explained by the rotational energy loss nor by the residual heat nor by accretion from a binary companion.

Subsequent observations have shown that both kinds of NSs share similar characteristics, i.e., similar magnetic fields that often can be as strong as $B \sim 10^{14} - 10^{15}$ G (derived from the spin-down rate) and persistent X–ray luminosities $L_X \sim 10^{33} - 10^{36}$ erg s^{-1}. Relatively frequent bursting activity is observed in both classes of objects. Magnetar bursts can be classified in three types:

[3]The Crab Pulsar (PSR B0531+21) is a relatively young NS. The source is in the center of the Crab Nebula, a remnant of the supernova SN 1054, which was widely observed by Chinese and Arab astronomers in the year 1054.

- Short bursts lasting $\sim 0.1 - 1$ s with luminosity of $\sim 10^{39} - 10^{41}$ erg s^{-1}.
- Intermediate bursts with $\sim 1 - 40$ s duration and luminosity $10^{41} - 10^{43}$ erg s^{-1}.
- Giant flares with luminosity $10^{44} - 10^{47}$ erg s^{-1}.

The last are rare events. Until now, they have been observed only three times and in three different SGRs (see Turolla et al. 2015 for a recent review). Currently, there are 23 confirmed AXPs/SGRs in our Galaxy plus 2 other sources detected in each of the Magellanic Clouds[4] (Olausen and Kaspi, 2014).

Moreover, two magnetars with peculiar characteristic have been recently observed, the so called 'low-field magnetars'. They have dipole magnetic fields comparable to that of normal radio pulsars $B \sim 10^{12} - 10^{13}$ G and spin down ages ranging from $\sim 10^{6} - 10^{7}$ yrs. However, they also show burst activity similar to that observed in SGRs (see Turolla et al. 2015 for a review). A third candidate with burst activity has been also detected, but more observations need to be performed to obtain its magnetic field (Rea et al., 2014).

1.4.1 Magnetar spectra

1.4.1.1 The X–ray emission

All the confirmed magnetars show pulsations in the soft X–ray band (< 10 keV). In several cases they have been also observed in the hard X–ray band ($\sim 100 - 200$ keV). The observed X–ray luminosity in half of them is nearly constant showing only a relatively small variability on long timescales (Mereghetti et al., 2015).

Magnetars are routinely observed in the soft X–ray band (using mainly the Chandra and the XMM-Newton space observatories). The X–ray pulsed profile of magnetars can differ markedly from source to source, from single to multipeaked. The pulsed fractions also vary, ranging from $\sim 10\%$ to nearly $\sim 100\%$. In general, within a single source, the pulse profiles are more complex at higher energies and may exhibit variations over long and short timescales. The short timescale vari-

[4] A catalogue can be found at http://www.physics.mcgill.ca/~pulsar/magnetar/main.html

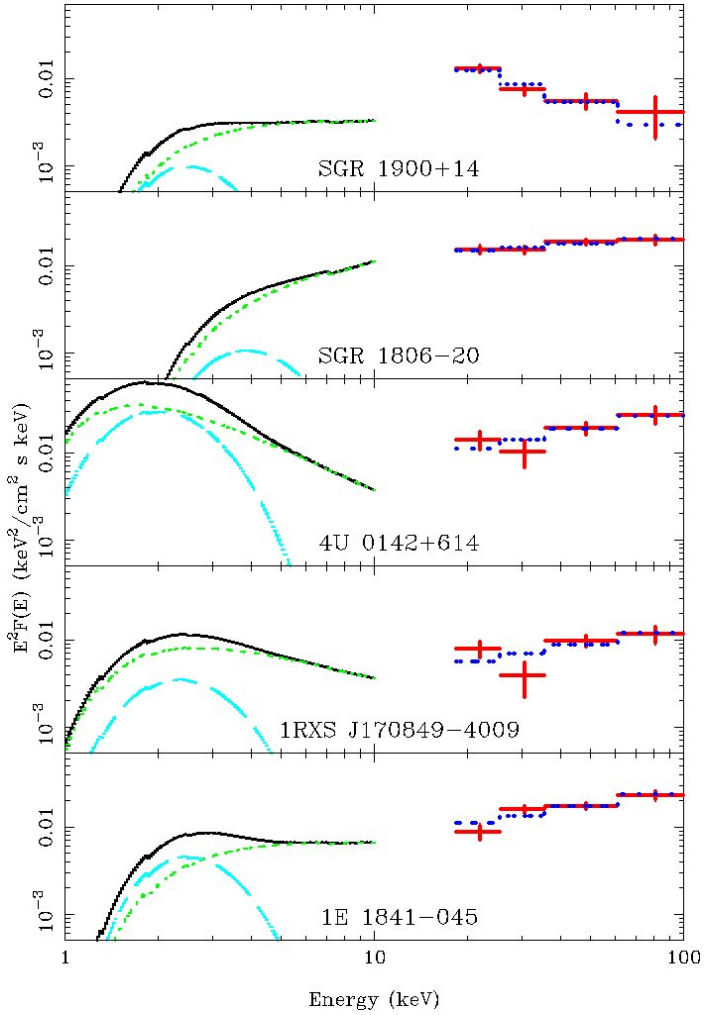

Figure 1.4: Broad band spectra for different magnetars (Götz et al., 2006). The black solid lines correspond to XMM data and the red error bars correspond to INTEGRAL data. The cyan and green lines show the best fitted blackbody and power law models in the soft X–ray, respectively. The blue dotted lines show the best fitted power law in the hard X–rays.

ations are usually associated with periods of bursting activity or with the source recovering after a flare (Mereghetti et al., 2015)..

Outside periods of bursting activity, the quiescent X–ray spectra of magnetars show a thermal and a non-thermal component (see Figure 1.4). The spectrum in the $2-10$ keV range is typically described by a blackbody with temperature $kT \sim 0.5$ keV plus a power law with a photon index $\Gamma \sim 3-4$ or a second blackbody component (see e.g. Oosterbroek et al., 1998; Patel et al., 2001). The power law (or non-thermal) component is probably caused by resonant cyclotron scattering

(RCS) between photons emitted from the surface and charges flowing in the magnetosphere (see Turolla et al. 2015 and references therein). Deviations of the thermal component from a single black body are expected theoretically for a number of reasons. For instance, the star may have a non-uniform surface thermal distribution, or be permeated by a gaseous atmospheric layer where radiation is reprocessed. Moreover, the magnetar magnetosphere is expected to be active and filled with charges that, in turn, may produce an efficient particle bombardment onto the magnetar surface.

Magnetar are also observed in the hard X–ray bands, mainly with the Integral, Suzaku and NuSTAR space telescopes (see again Figure 1.4). The properties of the spectrum in this band can be summarised as follows (Mereghetti et al., 2015):

- The observed luminosity detected in the hard spectrum is comparable to that below 10 keV.
- The $10 - 200$ keV spectrum is generally well fitted by a power law with photon index $\Gamma \sim 1 - 2$.
- The energy range of the spectrum in which the pulsed component appears is, in general, harder than that of the non pulsed emission. The shape the spectrum also shows phase-depend variations.
- In the MeV range, the upper limits available on the flux are better explained by models based on log-parabolic functions than power laws (Rea et al., 2007; den Hartog et al., 2008).
- In the $0.1 - 10$ GeV energy range, there is no detection of magnetar emission by the Fermi satellite and in the TeV range, no detection by ground based telescopes. The current upper limits obtained in the $0.1 - 10$ GeV appear to rule out early models that predicted emission from the outer magnetosphere (see for example Cheng and Zhang 2001).

The mechanism responsible for the high energy emission of magnetars (in the $20 - 100$ keV band) is still a subject of investigation. It was proposed that the hard

X–ray emission may be caused by thermal bremsstrahlung in the atmosphere of the magnetar heated by returning currents, or by synchrotron emission of electron positron pairs created in the upper magnetosphere (Thompson and Beloborodov, 2005). Also, resonant cyclotron scattering (RCS) of seed photons emitted by the surface with highly relativistic electrons flowing in the magnetosphere may boost the photon energy at such high energies (Baring and Harding, 2008; Beloborodov, 2013). The theoretical modelling of high energy emission is complicated by the fact that QED effects need to be taken into account to calculate the relevant cross sections. RCS spectra obtained with Monte Carlo simulations have been computed by Nobili et al. (2008), and a few examples for a twisted magnetic field including simplified assumptions for the magnetospheric electron current distribution have been discussed in Zane et al. (2011b). However, the present poor knowledge of the large scale distribution of the magnetic field and of the currents acceleration is hampering a quantitative fit of the observed spectra (for a review of the subject see Turolla et al. 2015).

1.4.1.2 Spectral features

As it will be discussed in detail later on (see Section 1.6.1), on the basis of the opacities properties it is expected that a magnetar should show spectral absorption features due to the strong magnetic field. For magnetic fields of $B \sim 10^{14} - 10^{15}$ G, electron and proton cyclotron lines should be in the MeV and keV energy range, respectively. The current detection of MeV electron cyclotron lines is not possible due to the lack of sensitive enough instruments. Instead, detection of lines in the soft X–rays (i.e. at a few keV) might be possible, and this motivated the intense search for proton cyclotron lines in the persistent emission from magnetars. Until now there has been no confirmed detection yet (see Tiengo et al. 2008). This may be caused, for example, by the superposition of the emission from different regions with different magnetic field strength or by vacuum polarisation effects, that may reduce the detectability of proton cyclotron lines (Mereghetti et al., 2015).

Recently, Tiengo et al. (2013) discovered an absorption feature in a low-field magnetar, SGR0418+5729. The feature has a strong energy and star rotation phase

dependence, and the line center varies between ~ 1 and ~ 5 keV on a short interval of the rotational phase. The phase-dependent feature is difficult to reconcile with atomic processes and instead is more easily understood in terms of a proton cyclotron line originating in a relatively small magnetic loop confined near the star surface. The field strength required in the loop, $B_{\rm loop} \sim (2-10) \times 10^{14}$ G, is much stronger that the strength of the large scale dipolar field, $B = 6 \times 10^{12}$ G inferred from the timing parameters. If this interpretation is correct, it will strengthen the idea that the magnetic topology of the field in magnetars is complex, and that multipolar components are present on small scales (possibly due to a localised twist), in agreement with the interpretation of the low field sources in terms of aged "waning magnetars" (Turolla et al., 2011).

1.4.1.3 Radio and Optical/infrared emission

Most magnetars do not have detectable radio emission (Mereghetti et al., 2015). However, radio pulsation have been observed in the transient magnetars XTE J1810−187 (Camilo et al., 2006) and 1E 1547.0−5408 (Camilo et al. 2007), with properties different to those observed in normal radio pulsars. The flux and pulse profile exhibit large variability on timescales of days. Moreover, the spectrum is very flat and highly polarised. Radio pulsations have been also detected from a transient magnetar located in the Galactic Center, SGR J1745-2900 (Eatough et al., 2013; Shannon and Johnston, 2013). The properties are similar to the other two magnetars detected in radio. Furthermore, one magnetar source has been discovered from observations in the radio band, PSR J1622−4950 (Levin et al., 2010). This source does not show typical magnetar activity, and its relatively fast decreasing X–ray luminosity suggests an interpretation in terms of a transient magnetar.

Detection of magnetars in other bands such as optical and infrared is challenging, due to their intrinsic faintness in these bands and by their location in the Galactic plane, which results in a strong absorption (Mereghetti et al., 2015). Optical counterparts have been suggested for a few sources and associations are certain for three magnetars that show optical pulsations at the star spin period: 4U 0142+61 (Kern and Martin, 2002; Dhillon et al., 2005), 1E 1048.1−5937 (Dhillon et al.,

2009) and SGR 0501+4516 (Dhillon et al., 2011). The observed counterparts have magnitudes $K \sim 19-22$ in the near infrared, and $\sim 23-26$ in the optical band. Again, the mechanisms responsible for such emissions are not certain and among the proposed scenarios are emission from a fossil disk and/or non-thermal curvature emission from pairs in the inner magnetosphere (see for example Beloborodov and Thompson 2007; Zane et al. 2011a).

1.4.2 Theory of Magnetars

1.4.2.1 Formation and origin

Two potential channels of formation of a strongly magnetised NS, following a supernova explosion, have been proposed. The first one exploits the fact that the magnetic flux must be conserved during the core collapse event, or fossil field scenario (Woltjer, 1964; Ruderman, 1972; Ferrario and Wickramasinghe, 2006). As the NS is very small compared to its precursor, the final magnetic field after the collapse could be as high as that observed in magnetars. NSs are expected to be the end point of evolution of stars with mass > 8 $M_\odot$, which correspond to O and early B type stars. In particular, relatively high magnetic fields $B \sim 1-10$ kG have been detected in O stars (see for example Donati et al. 2006). The magnetic flux, $\Phi = \pi R^2 B$, in these stars is the same order of magnitude of that of a magnetar, with $B \sim 10^{15}$ G, and white dwarfs with the strongest magnetic fields (see e.g. Reisenegger, 2001; Harding and Lai, 2006).

This scenario is, however, problematic: to explain the observed number of sources with $B \sim 10^{14}-10^{15}$ G simply in terms of flux conservation is hard due to several reasons. First, it is only a fractional area that corresponds to $\sim 2\%$ of the progenitor that collapses to form a NS, and this reduces the final magnetic field of the NS. Second, the magnetar birth rate which is needed to explain the current number of detected sources is higher than the number of potential progenitor stars with magnetic fields $B > 10$ kG (Keane and Kramer, 2008). It is also expected that in a NS the crust will be formed after ~ 100 s following the supernova explosion, which corresponds to the time scale at which the surface magnetic field is frozen. However, for $B \sim 10^{15}$ G, the Alfvén crossing time through the star is ~ 0.1 s. This

means that any magnetic field in the star has enough time to evolve into a stable configuration with minimal energy[5] (in case it exists) or to decay fast and disappear before the crust formation (Braithwaite and Spruit, 2006).

The second proposed channel invokes an efficient dynamo process (Duncan and Thompson, 1992; Thompson and Duncan, 1993). In a proto-NS, the matter is opaque to neutrinos, and heat transport in the star interior is driven by convection. Fast rotation and convection in the NS generate an α dynamo process, which amplifies a seed dipole field. In addition, the differential rotation produces a ω process, which leads to the formation of a strong toroidal field. This $\alpha - \omega$ dynamo requires, to be efficient, that the newly formed proto-neutron star rotates with a period < 3 ms such that efficient convective mixing can occur (Duncan and Thompson, 1992). Thus, in this scenario, magnetars would be the final product of the evolution of massive stars with fast rotating core (Burrows et al., 2007).

1.4.2.2 Burst trigger mechanisms

Reconfiguration of magnetic field is believed to be the main mechanism responsible for triggering the variety of bursting activity observed from magnetars. The evolution and subsequent decay of the star magnetic field (Goldreich and Reisenegger, 1992) affect both the star and its magnetosphere and can give rise to a series of processes that ultimately result in burst emission. Several scenarios have been proposed, and the main difference among them is the location of the trigger mechanism that can be in the core, crust, or magnetosphere of the star (for a review see Turolla et al., 2015; Kaspi and Beloborodov, 2017).

Models based on the core location follow the idea that, after the magnetar formation, the magnetic field may evolve into an unstable configuration in the core of the star (Flowers and Ruderman, 1977). At some point, this causes a build up of an instability (Thompson and Duncan, 1995) and eventually leads to a rapid magnetic reconfiguration, injecting Alfvén waves into the magnetosphere and hence producing the observed burst emission.

[5] Depending on the total magnetic energy, different magnetic equilibria may be present in the star interior e.g., a magnetic field with poloidal and toroidal components. However, their stability is still under debate (see for example Mitchell et al. 2015).

The other alternatives are based on the idea that stable configurations of the magnetic field in a NS should be a combination of a poloidal and a toroidal component (Braithwaite and Spruit, 2006). In particular, a strong toroidal component is expected in the interior and crust of the star and may contain most of the magnetic energy. As the magnetic field evolves, the toroidal component can transfer some helicity to the external dipolar component, a process that should be mediated through crustal displacements.

The main consequence is that the evolution of the magnetic field in the crust and magnetosphere of the star can build up a substantial stress in the solid crust. In fact, the magnetic field foot points are anchored to the solid crust: therefore, as a growing twist is imparted into the magnetosphere (for instance because the magnetic field helicity is transferred outwards from the toroidal crustal component), it can elastically deform (and accumulate a stress in) the crust. During this process the crust accumulates elastic energy. Since the crust of the star can resist only up to a certain level of deformation, that depends on its breaking strain, once the critical deformation threshold is reached the crust cracks. The subsequent release of energy can then power the observed bursts (Thompson and Duncan, 1995). Simulations of the evolution of the NS magnetic field, together with recent result of the braking stress of the crust, show that the age is the key variable that may explain the variety of observed phenomena in AXPs and SGRs, and relatively old low-field magnetars (Perna and Pons, 2011)

The third proposed scenario is based on a magnetospheric origin for the burst activity (Uzdensky, 2011). Again, it is assumed that a substantial helicity is transferred outwards and that, as the external magnetic field evolves, it can be subject to plasma instabilities that result into a spontaneous magnetic reconnection and consequently burst emission (see for example Parfrey et al. 2013). The powering mechanism of magnetar bursts may then show similarities with processes studied in solar physics such as reconnection in the corona of the Sun and flux tube ejection (see for example Meng et al. 2014 for a recent study).

1.5 X–ray dim Isolated NSs

XDINSs, also known as the Magnificent Seven, are highly magnetised NSs, $B \sim 10^{13}$ G, within the range of those of magnetars. However, unlike magnetars, XDINSs show no burst activity and their X–ray spectra are purely thermal and well represented by a black body. The thermal emission observed from XDINSs is not affected from magnetospheric activity, nor a surrounding nebula or supernova remnant.

All seven sources were discovered by the ROSAT satellite (Haberl, 2007; Turolla, 2009) and they are located at a distance between ~ 200 and 500 pc from Earth. The first of them, J1856.5−3754, was discovered by Walter and Lattimer (2002). Some common properties of XDINSs are (Turolla, 2009):

- X–ray luminosities of $L \sim 10^{30} - 10^{32}$ erg s^{-1}.
- Blackbody fits to the observed spectra consistent with temperatures $\sim 50 - 100$ eV.
- Pulsation periods quite large, and clustered in the range $P \sim 3 - 12$ s.
- Faint optical counterparts with an exceeding large X–ray-to-optical flux ratio $F_X/F_{opt} \sim 10^4 - 10^5$.
- No evidence of a binary companion.
- Low value of the Galactic hydrogen column density towards the sources, as derived from their X–ray spectra, $N_H \sim 10^{20}$ cm^{-2}.

Unlike radio pulsars, XDINSs do not show radio emission. The timing properties, however, can be obtained by the X–ray lightcurve, which in XDINSs is in general quasi-sinusoidal and single peaked. For example, the brightest XDINS, RX J1856.5−3754, has a period $P = 7.055$ s with a X–ray pulsed fraction[6] of 1.5 % (Tiengo and Mereghetti, 2007). The pulsed fraction observed from most XDINSs is generally low, but in a few cases, such as RX J1308.6+2127, it may exceed 25%.

[6]Pulsed fraction is defined as pf $= (F_{max} - F_{min})/(F_{max} + F_{min})$

Table 1.1: Timing and optical properties of XDINSs

Name	P (s)	$\dot{P}$ (10^{-14} s s^{-1})	$B_{\rm dip}$ (10^{13} G)	age (10^6 yr)	Ref.	mag$^{(h)}$
J0420.0−5022	3.5	2.8±0.3	1.0±0.1	2.0	(a)	$B = 26.6$
J0720.4−3125	8.4	1.04±0.6	2.4±0.5	1.9	(b)	$B = 26.6$
J0806.4−4123	11.4	5.5±3.0	2.5±3.8	3.3	(c)	$B > 24$
J1308.6+2127	10.3	11.20±0.03	3.40±0.01	1.5	(d)	$m_{\rm 50ccd} = 28.6$
J1605.3+3249	3.4	-	-	-	(e)	$B = 27.2$
J1856.5−3754	7.1	2.97±0.07	1.5±0.03	3.8	(f)	$B = 25.2$
J2143.0+0654	9.4	4.1±1.8	2.0±0.9	3.7	(g)	$B > 26$

Surface dipolar magnetic field inferred from $B_{\rm dip} = 6.4 \times 10^{19}(P\dot{P})^{1/2}$ G (Mereghetti, 2011).
(a) Kaplan and van Kerkwijk (2011)
(b) Kaplan and van Kerkwijk (2005a); Haberl et al. (2004b); Cropper et al. (2004)
(c) Kaplan and van Kerkwijk (2009a)
(d) Kaplan and van Kerkwijk (2005b)
(e) Pires et al. (2014)
(f) van Kerkwijk and Kaplan (2008)
(g) Kaplan and van Kerkwijk (2009b)
(h) Magnitudes taken from Haberl (2007)

The period derivative has been obtained for most of them (with the exception of RX J1605.3+3249), which allows to infer their magnetic fields and spin-down ages (see Table 1.1).

In spite that blackbody emission describes relatively well the continuous X–ray emission from XDINSs, XMM Newton data show absorption features in five[7] of them (see Table 1.2). RX J1308.6+2127 shows a second absorption feature harmonically spaced and RX J1605.3+3249 shows up to three lines with energy ratios 1, 1.5 and 2. The properties of the features are similar in the different sources: the lines are centered at energies of some hundreds of eV and with an equivalent width of several tens eV. The origin of these features is not clear yet, and two possible explanations have been suggested: proton cyclotron resonances or atomic transitions in light element atmospheres. The observed lines, in particular when multiple, are probably caused by both effects. In both cases a magnetic field $B \sim 10^{13}$ G is

[7]Potentially, RX J0420.0−5022 presents an absorption feature in its spectrum, but it has not been confirmed yet (Haberl et al., 2004a).

Table 1.2: XDINSs with spectral features

Name	P (s)	$B_{\rm dip}$ (10^{13} G)	$E_{\rm cyc}^{\rm (f)}$ (eV)	$B_{\rm cyc}^{\rm (f)}$ (10^{13} G)	References
J0720.4−3125	8.39	2.4 ± 0.5	270	5.6	(a)
J0806.4−4123	11.37	2.5 ± 3.8	430/306[1]	8.6/6.1	(b)
J1308.6+2127	10.31	3.4 ± 0.01	300/230[1]	6.0/4.6	(c)
J1605.3+3249	3.39	-	450/400[2]	9/8	(d)
J2143.0+0654	9.43	2.0 ± 0.9	750	15	(e)

[1] Fit spectrum with one line/two lines (minimal energy)
[2] Fit spectrum with one line fit/ three lines (minimal energy)
(a) Haberl et al. (2004b); Borghese et al. (2015)
(b) Haberl et al. (2004a)
(c) Haberl et al. (2003); Schwope et al. (2007)
(d) van Kerkwijk et al. (2004)
(e) Zane et al. (2005)
(f) Approximate values taken from Haberl (2007)

required. In two XDINSs, RX J0720.4−3125 and RX J1308.6+2127, the magnetic field derived from the timing properties is in relatively good agreement with the magnetic field inferred from the line energy. Recently, an absorption feature was observed in the spectrum of RX J0720.4−3125, which is energy and phase dependent (Borghese et al., 2015). The feature has an energy of ~ 750 eV, an equivalent width of ~ 30 eV, and it is significantly detected for only 20% of the pulsar rotation. This feature may be caused by resonant proton cyclotron absorption (or scattering) in a small multipolar loop of the magnetic field in the NS surface. The absorption line is consistent with a magnetic field strength $B \sim 10^{14}$ G, revealing a more complex topology than a pure magnetic dipole field in this NS.

Most of the XDINS show an optical counterpart (Table 1.1, see also Mignani 2011 and references therein). By using HST, optical emission was first detected from RX J1856.5−3754. After that, HST also detected optical emission from RX J1308.6+2127 and RX J1605.3+3249. Using ground based observatories, optical emission has been also detected in RX J0720.4−3125 and J214303.7+065419. A potential optical counterpart has been also proposed for RX J0420.0−5022. In gen-

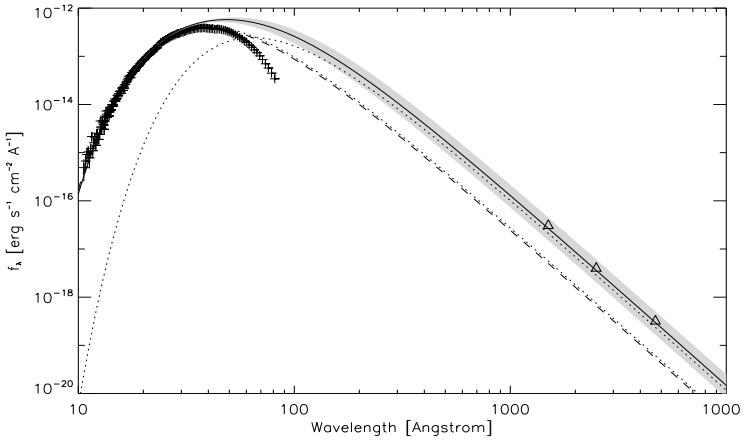

Figure 1.5: Broad band spectrum of RX J1856.5−3754 and two blackbody fits with temperatures $kT \simeq 62$ and 39 eV (Sartore et al., 2012). The dashed line is the extrapolation of the (unabsorbed) X–ray blackbody from Burwitz et al. (2003). The triangles represent the optical/UV data obtained from HST photometry (Kaplan et al., 2011a).

eral, the optical fluxes are higher by a factor $\sim 5-10$ than the extrapolation of the blackbody fluxes. In the best studied cases, RX J1856.5−3754 (van Kerkwijk and Kulkarni, 2001b; Sartore et al., 2012) and RX J0720.4−3125 (Motch et al., 2003), the optical spectra nearly follow a Rayleigh-Jeans law, and are consistent with thermal emission from a larger and cooler part of the NS surface at $T \sim 10^5$ K. Figure 1.5 shows the optical/ultraviolet and X–ray spectrum of RX J1856.5−3754 with the extrapolation mentioned above.

With the discovery of an optical counterpart it was possible to measure the proper motion and, in two sources, the parallax. The proper motions of RX J1856.5−3754, RX J0720.4−3125, and RX J1605.3+3249 are in the range $\sim 100-300$ mas/yr. There are also upper limits obtained via X–ray observations of RX J0806.4−4123 and RX J0420.0−5022, which are consistent with a proper motion < 100 mas/yr (Motch et al., 2009). The parallax measurements have been obtained for RX J1856.5−3754 and RX J0720.4−3125, allowing to measure a distance of $d = 123^{+11}_{-15}$ (Walter et al., 2010) and 286^{+27}_{-23} pc (Tetzlaff et al., 2011), respectively. The proper motions together with the parallax distances can provide the transverse velocity for these objects, which are ~ 280 and ~ 115 km/s, respectively.

The fast proper motion of these XDINS allows to rule out accretion from the

interstellar medium as the source of their X–ray luminosity. In addition, the period and period derivative imply that XDINSs have a spin-down age $\sim 10^5 - 10^6$ yr, which, when compared with theoretical models for the thermal evolution of passively cooling NSs[8], supports the idea that the X–ray emission from these objects is powered by the cooling of the star (Turolla, 2009).

There are several open issues that need to be addressed in the study of XDINSs. The spectral features present in most of the XDINSs, if explained with either proton cyclotron resonance or the atomic transition, require the presence of an atmosphere. However, it is difficult to explain the overall spectral energy distribution of XDINSs with atmosphere models. Moreover, the spectrum of RX J1856.5−3754 is nearly planckian and featureless. Other models for the thermal emission such as radiation from a bare or condensate (Section 1.6.4) surface may explain some of these aspects (see for example Turolla et al. (2004); Turbiner and López Vieyra 2006; Potekhin et al. 2012). In addition, the link between XDINSs and other NSs population is not clear, yet. The magnetic field of XDINSs is 1−2 order-of-magnitude weaker than those found in strong B-field magnetars. In turn, the spin-down age of XDINSs shows that this population is older than magnetars. Thus, the potential evolutionary link from magnetars to XDINSs, in terms of a decaying magnetic field, is still matter of study.

[8]Dynamical ages of XDINSs (obtained by identifying their parental star clusters and, then, by extrapolating backward the NS velocity vector in the Galactic potential) are somewhat shorter than spin-down ages.

1.6 Thermal emission from passively cooling NSs

The properties of matter under strong magnetic fields are not well understood, as neither are the properties of the radiation from the surface of magnetised sources such as XDINSs and magnetars. Following the studies that suggest a condensed phase for magnetic fields as those observed in XDINSs (Turolla et al., 2004; van Adelsberg et al., 2005), in this section two emission models are considered: a gaseous atmosphere and a condensed surface. The radiative transfer problem in a magnetised plasma is described and the standard approaches to solve the emission from both a (non-magnetic and magnetic) atmosphere and a condensed metallic surface are reviewed.

1.6.1 Radiative transfer in strong magnetic fields

Different media have different effects on the propagating radiation. Macroscopically, this is quantified by the opacity of the medium, which depends on the chemical composition, density, temperature and as well on the energy of the propagating photon. The total opacity of the medium is the sum of scattering and absorptive opacities. In an unmagnetised plasma, both scattering (Thompson) and free–free opacities are intrinsically featureless, with a constant and a smooth energy dependence, respectively. However, bound-bound and bound-free opacities produce different absorption lines (at different energies), which impart to the radiation a particular imprint of the medium in which it is propagating.

If a strong magnetic field is present, the opacities can be dramatically modified with respect to the non-magnetic case (Mészáros, 1992). A strong magnetic field can change the energy levels of atoms, and then the bound-bound and bound-free opacities. Moreover, if the medium is partially or fully ionised, the dynamics of free electrons/protons below the electron/proton cyclotron energy is no longer dominated by thermal motion. Thus, in this case, also free-free and scattering opacities depend on the magnetic field, and in particular on both, its strength and direction.

1.6.1.1 Plasma dielectric tensor

In order to compute the properties of the wave's electric field and the opacities in a magnetised plasma, it is necessary to introduce the complex dielectric tensor (Shafranov, 1967; Ginzburg, 1970; Mészáros, 1992). Following Ho and Lai (2001), this tensor and the associated polarisation vectors of the wave electric field can be expressed as below.

In a reference frame in which the magnetic field is parallel to the z-axis, the dielectric tensor is given by

$$\left[\varepsilon'_{ij}\right] = \begin{bmatrix} \varepsilon & ig & 0 \\ -ig & \varepsilon & 0 \\ 0 & 0 & \eta \end{bmatrix}, \tag{1.6}$$

where its components, considering different species of charged particles s, are given by

$$\varepsilon = 1 - \sum_s \frac{\lambda_s v}{\lambda_s^2 - u} \tag{1.7}$$

$$\eta = 1 - \sum_s \frac{v}{\lambda_s} \tag{1.8}$$

$$g = -\sum_s \frac{u^{1/2} v}{\lambda_s^2 - u}. \tag{1.9}$$

Here, $u = \omega_{cs}^2/\omega^2$ and $v = \omega_{ps}^2/\omega^2$, where ω_{cs} is the cyclotron frequency and ω_{ps} is the plasma frequency of the species s, and ω is the frequency of the electromagnetic wave. In order to take into account the collisions of particles, a damping factor λ_s is considered for each particle species s.

It is convenient to derive the properties of the electromagnetic wave propagating in the plasma by considering a reference frame in which the wave vector $\mathbf{k}$ is parallel to the z-axis and the magnetic field is located in the x-z plane. By solving the Maxwell equations, it can be found that the components of the electric vector of the wave, for an angle of propagation θ_B with respect to the magnetic field, are given by

$$\mathbf{E}^j = \mathbf{e}^j = \frac{1}{\sqrt{1+K_j^2+K_{z,j}^2}}(iK_j, 1, iK_{z,j}) \tag{1.10}$$

where

$$K_j = \beta\left[1+(-1)^j\left(1+\frac{1}{\beta^2}\right)^{1/2}\right], \tag{1.11}$$

$$K_{z,j} = \frac{u_e\nu(1-u_i-M^{-1})\sin\theta_B\cos\theta_B K_j - u_e^{1/2}\nu\sin\theta_B}{(1-u_e)(1-u_i)-\nu[(1-u_i)(1-u_e\cos^2\theta_B)-Mu_i\sin^2\theta_B]}, \tag{1.12}$$

$$\beta = \frac{u_e^{1/2}}{2(1-\nu)}\frac{\sin^2\theta_B}{\cos\theta_B}\left(1-u_i-\frac{1+\nu}{M}\right), \tag{1.13}$$

and $M = Am_p/(Zm_e)$.

The main properties of the polarisation vectors are listed below (Ho and Lai, 2001).

- The modes are elliptically polarised. For $j = 1$, the extraordinary mode (X-mode) is mostly perpendicular to the **k**-**B** plane. Instead, for $j = 2$, the ordinary mode (O-mode) lies in the **k**-**B** plane. This can be derived from the properties: $K_1 = -K_2^{-1}$ and $|K_1| < 1$.

- For, $\omega \ll \omega_{ce}$ the modes are pretty much linearly polarised, except for angles close to $\theta_B = 0$ and π, where the modes are circularly polarised.

- The component along the z-axis $K_{z,j} \propto \rho/\omega^2$, where ρ is the density of the plasma. Then, for relatively low densities, the modes are transverse. Notice that this approximation is often used to describe the wave electric field propagation when modelling magnetised atmospheres.

The components of the polarisation vector are standardly expressed in the so–called "rotating coordinates", i.e. in a system in which the z-axis is parallel to the magnetic field direction and two perpendicular coordinates in the plane x-y (defined as below) are indicated with $\pm$. After the change of coordinates, the resulting

expressions are:

$$|e^j_{\pm}|^2 = \left|\frac{1}{\sqrt{2}}\left(e^j_x \pm i e^j_y\right)\right|^2 = \frac{\left[1 \pm \left(K_j \cos\theta_B + K_{z,j}\sin\theta_B\right)\right]^2}{2(1+K_j^2+K_{z,j}^2)} \quad (1.14)$$

$$|e^j_z|^2 = \frac{\left(K_j \sin\theta_B - K_{z,j}\cos\theta_B\right)^2}{1+K_j^2+K_{z,j}^2}. \quad (1.15)$$

1.6.1.2 Opacities

In the following, it is considered the case of a fully ionised light element plasma in which the main sources of opacity are free-free absorption and Thomson scattering. As already mentioned, in a non-magnetised plasma the opacities relative to both processes are featureless. The free-free opacity, for a given temperature and density, has a smooth dependence on the frequency $\propto \omega^{-3}$ (for $\hbar\omega \gg k_B T$), and the Thomson scattering opacity does not depend on the frequency. In a strongly magnetised plasma, these opacities change substantially and depend on the mode j in which the electromagnetic wave propagates through the components of the polarisation vectors. Notice that, in the following, the components of these vectors in rotating coordinates are labelled as e^j_α, where $\alpha = -1, 0, 1$ and $e^j_0 \equiv e^j_z$ while $\alpha = +1$ and -1 refer to the $\pm$ rotating components.

The electron scattering opacities from mode j to mode i are given by (Ventura, 1979; Kaminker et al., 1982)

$$\kappa^{s,e}_{ji} = \frac{3}{4}\kappa_T \sum_{\alpha=-1}^{1} |e^j_\alpha|^2 |e^i_\alpha|^2 \frac{1}{(1+\alpha u^{1/2})^2 + \gamma_r^2} \quad (1.16)$$

where e^i_α, as mentioned above, correspond to the components of the normal modes in the coordinate frame with the z-axis parallel to $\mathbf{B}$ and $\gamma_r = (2/3)(e^2/m_e c^3)\omega$ is the radiation damping. The scattering opacity for mode j, angle-integrated for all possible output for mode i, is given by

$$\kappa^{s,e}_{j} = \kappa_T \sum_{\alpha=-1}^{1} |e^j_\alpha|^2 \frac{1}{(1+\alpha u^{1/2})^2 + \gamma_r^2}, \quad (1.17)$$

where $\kappa_T = \sigma_T / m_p$ is the Thomson opacity and σ_T is the Thompson scattering cross

section. Similarly, the ion scattering opacities are given by (Pavlov et al., 1995)

$$\kappa_{ji}^{s,p} = \frac{3}{4}\kappa_T \mu_m^2 \sum_{\alpha=-1}^{1} |e_\alpha^j|^2 |e_\alpha^i|^2 \frac{1}{(1-\alpha u^{1/2})^2 + \mu_m^2 \gamma_r^2} \tag{1.18}$$

$$\kappa_j^{s,p} = \mu_m^2 \kappa_T \sum_{\alpha=-1}^{1} |e_\alpha^j|^2 \frac{1}{(1-\alpha u^{1/2})^2 + \mu_m^2 \gamma_r^2} \tag{1.19}$$

where $\mu_m = m_e/m_p$ and $u_p = \omega_{\rm c,p}^2/\omega^2$.

The free-free opacity[9] for electron and ions are given by (Pavlov and Panov, 1976; Mészáros, 1992; Pavlov et al., 1995)

$$\kappa_j^{ff,e} = \kappa_{\rm ff} \sum_{\alpha=-1}^{1} |e_\alpha^j|^2 \frac{g\alpha}{(1+\alpha u^{1/2})^2 + \gamma_r^2} \tag{1.20}$$

$$\kappa_j^{ff,p} = \kappa_{\rm ff} \mu_m^2 \sum_{\alpha=-1}^{1} |e_\alpha^j|^2 \frac{g\alpha}{(1-\alpha u^{1/2})^2 + \mu_m^2 \gamma_r^2} \tag{1.21}$$

where $\kappa_{\rm ff}$ is the non-magnetic free-free opacity, and $g_0 = g_\parallel$, $g_{-1} = g_{+1}{=}g_\perp$, are the magnetic Gaunt factors (Pavlov and Panov, 1976).

The total opacities for absorption and scattering considering the contribution from electrons and ions are then $\kappa_j^{ff} = \kappa_j^{ff,p} + \kappa_j^{ff,e}$ and $\kappa_j^s = \kappa_j^{s,p} + \kappa_j^{s,e}$. It is interesting to study the response of the opacities to photon propagation in the typical conditions of an atmosphere: low density plasma and frequencies under the electron cyclotron frequency. If in addition we consider a photon propagation direction not parallel (or too close) to the magnetic field direction, and frequencies away from the ion cyclotron frequency, then the opacities relative to the X-mode are substantially reduced and are given by (Ho and Lai, 2001)

$$\kappa_1^{ff} \propto \frac{1}{\omega_{ce}^2 \omega}\left(1 - e^{-\hbar\omega/kT}\right) \quad \text{and} \quad \kappa_1^s \propto \left(\frac{\omega}{\omega_{ce}}\right)^2 \tag{1.22}$$

The opacities relative to the O-mode ($j = 2$) are instead almost unaffected by the magnetic field and have a behavior similar to that of the unmagnetised case.

[9] Other expressions that take into account the motion of both interacting particles, electrons and ions, in the strong magnetic field can be found in Potekhin and Chabrier (2003)

1.6.2 Atmosphere models for passive coolers

The thermal radiation from passively cooling NSs is expected to be reprocessed by a layer of gas at the surface, or atmosphere. This atmosphere can be present due to the fall-back gas from the supernova explosion or due to accretion of matter from the interstellar medium. Due to the strong surface gravitational field of the NS, $g_s \sim 10^{14} - 10^{15}$ cm s^{-2}, the atmosphere (for sub-Eddington luminosities) is expected to be very thin (in passively cooling stars), with typical scale height $H \sim k_B T_s/(m_p g_s) \sim 0.1 - 10$ cm, where k_B is the Boltzmann constant, m_p is the proton mass, and T_s is the surface temperature (typically $\sim 10^6 - 10^7$ K). Since the high gravitational field stratifies the composition of the atmosphere in a relatively short timescale, NS atmospheres are expected to be composed by light elements such as hydrogen or helium at the top of the atmosphere with the heavier elements located in deeper layers (Romani, 1987).

Due to the temperature gradient, composition, and magnetic field, the emergent spectrum from NS atmosphere is expected to show deviations from a black-body model. Numerical solutions have been presented by several teams for both non-magnetic atmospheres and magnetic atmospheres. In non-magnetic atmospheres, the standard approach for computing the emergent spectrum (Zavlin, 2009) is based on the assumptions listed below (notice that in the following the ν subscript indicates the dependence on the frequency).

- First, since the size of the atmosphere is very small compared to the radius of the star, $H \ll R \sim 10$ km, the radiative transfer can be calculated in the limit of a plane-parallel atmosphere. Thus, the specific intensity I_ν through the atmosphere is computed by solving the radiative transfer equation (Rybicki and Lightman, 1979):

$$\mu \frac{\mathrm{d}I_\nu}{\mathrm{d}y} = k_\nu (I_\nu - S_\nu), \tag{1.23}$$

  where $\mu = \cos\theta$ (with θ the photon propagation direction relative to the normal to the surface), y is the column density ($\mathrm{d}y = \rho \mathrm{d}z$, with z the geometrical

depth), $\kappa_\nu = \kappa_\nu^{ff} + \kappa_\nu^{s}$ is the total opacity of the medium (with contribution from absorption κ_ν^{ff} and scattering opacities κ_ν^{s}), and

$$S_\nu = \frac{\kappa_\nu^{s} J_\nu + \kappa_\nu^{ff} B_\nu}{\kappa_\nu} \tag{1.24}$$

is the source function. Here, $J_\nu = (1/2)\int_{-1}^{1} I_\nu \mathrm{d}\mu$ is the mean intensity and B_ν is the Planck function.

- Second, due to the relatively high density of the gas, $\rho \sim 1$ g cm^{-3} (comparable to the density of water on Earth), atmospheres of NSs are assumed to be in local thermodynamic equilibrium.

- Third, the atmosphere is in hydrostatic equilibrium. This means that the gradient of the pressure through the atmosphere (for luminosity much lower than the Eddington luminosity) is given by

$$\frac{\mathrm{d}P}{\mathrm{d}z} = -\rho g_s, \tag{1.25}$$

where, ρ is the density and the gravitational acceleration, g_s is assumed constant since its variation through the geometrically thin atmosphere is insignificant.

- Fourth, the atmosphere is in radiative equilibrium. Then,

$$\int_0^\infty \kappa_\nu^{ff} \left(\frac{B_\nu}{2} - J_\nu \right) \mathrm{d}\nu = 0. \tag{1.26}$$

However, this condition is not sufficient to constrain the magnitude of the flux. In a passive NS, the only source of thermal energy comes from the cooling of the star interior, thus, the radiative flux through the atmosphere is constant. The total energy is transported only by radiation and the flux is constrained through the atmosphere via the integral

$$\int_0^\infty \mathrm{d}\nu \int_{-1}^{1} \mu I_\nu \mathrm{d}\mu = \sigma T_{eff}^4, \tag{1.27}$$

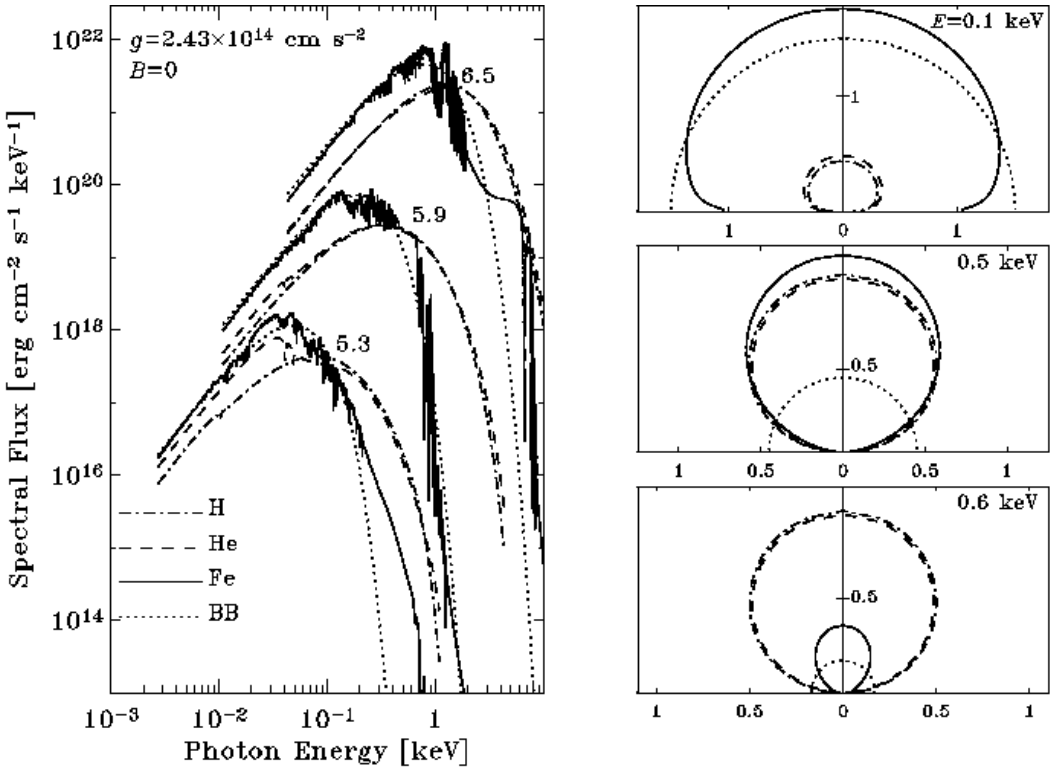

Figure 1.6: Non-magnetic NS atmosphere models from Zavlin 2009. **Left panel**: Emergent spectra for atmospheres with different effective surface temperatures and compositions. **Right panel**: Polar diagrams of normalised spectral specific intensities at temperature $\log T_{eff} = 5.9$ and different photon energies, E, and compositions. The normal to the surface is directed upward.

where σ is the Stefan-Boltzmann constant, and T_{eff} is the effective temperature.

In order to compute the emergent spectrum we need to provide an equation of state for the atmospheric plasma. Since in the simplest atmosphere models the kinematics of free particles are affected only by thermal effects, with Coulombian interaction giving a negligible effect on free electrons and ions, an ideal equation of state can be used as a good approximation to compute the emergent spectrum.

Figure 1.6 shows the emergent spectra of non-magnetic atmospheres for different chemical compositions and temperatures. In the left panel, the emergent spectra show noticeable deviations from a blackbody spectrum. In the case of light element atmospheres, H and He chemical compositions, the spectra are shifted to high energies compared to the case of a blackbody spectrum. This can be explained by

considering the properties of the free-free opacities, which are dominant in the energy and temperature range of the emergent spectrum. Free–free opacities have a energy dependence $k_\nu^{ff} \propto E^{-3}$ (for $E \gg kT$) and $k_\nu^{ff} \propto E^{-2}$ (for $E \ll kT$), which means that the atmosphere is optically thick (opaque) for low-energy photons. In other words, whereas low-energy photons can leave the atmosphere only from external and colder layers, high-energy photons can leave the atmosphere from deeper and hotter layers. Thus, the net effect of free–free opacities is to produce an emergent spectrum that is substantially harder than a simple blackbody. On the other hand, in the the case of heavy element atmospheres such as those with a Fe chemical composition, the emergent spectrum is affected mainly by the bound–bound and bound–free transitions in the atoms, which are reflected in the multiple absorption lines of the spectra.

Another important result which emerged from the computation of atmospheric models is that the emergent intensity is substantially beamed, i.e. it depends on the angle of emission. Figure 1.6, right panel, shows the angular dependence for the intensities. The case of a blackbody is shown with dotted line, which is isotropic, and then, the intensity is the same at all angles. However, in the case of model atmosphere spectra, intensities with different angles are produced from different layers of the atmosphere. In general, the maximum intensity is for those rays with direction parallel to the normal to the surface because they are produced in the deepest and hottest layers of the atmosphere. Instead, the minimal intensity is for rays nearly parallel to the surface because they are produced in the coolest layers of atmosphere.

1.6.3 Magnetised atmospheres

The criteria to establish if the magnetic fields are important for modelling magnetised atmospheres depend on the spectral energy range we wish to consider, temperature and on the magnetic field strength on the NS surface. Roughly, a magnetic field changes the properties of the atmosphere in two ways: by modifying the energy levels of the atoms and by modifying the dynamics of free electrons with kinetic energy below the electron cyclotron energy, which changes the free-free opacity.

Considering the electron cyclotron energy, $\hbar\omega_B$, a magnetic field changes the structure of the atoms if the ratio $\hbar\omega_B/Z^2Ry \sim (B/10^9\mathrm{G})Z^{-2} > 1$, where Z is the atomic number and $Ry = 13.6$ eV is the Rydberg energy. Similarly, for the free-free opacities, magnetic fields are important if the ratio $\hbar\omega_B/k_BT \sim (B/10^{10}\mathrm{G})(10^6\mathrm{K}/T) > 1$. Therefore, magnetic fields $B > 10^{13}$ G, like those of XDINSs and magnetars, can affect dramatically the thermal X–ray emission from NSs with surface temperature $T \sim 10^6$ K.

The first magnetised atmosphere models were computed by Shibanov et al. (1992) and Pavlov et al. (1994) for magnetic fields $B \sim 10^{12} - 10^{13}$ G. Magnetised NS atmospheres with accretion, and considering full, angle-dependent models, were first computed by Zane et al. (2000). The opacities adopted in the models include free-free transitions and electron scattering for hydrogen composition. The bound-free opacities are treated in a highly approximate manner and bound-bound transitions are not considered. Models of magnetic iron atmospheres (with $B \sim 10^{12}$ G) were studied by Rajagopal et al. (1997). Because of the complexity in the atomic physics and radiative transport, these Fe models are based on rough approximations. Atmosphere models for strong magnetic fields, $B > 10^{14}$ G have been computed by Ho and Lai (2001), and models including QED effects have been computed by Özel (2001) and Zane et al. (2001). The last work focused on the study of the proton cyclotron feature in the emergent spectra. Lai and Ho (2002) showed that because of QED effects or vacuum polarisation, mode conversion (photon in one mode can change into other mode with certain probability, see also Pavlov and Shibanov 1979 for an alternative treatment) can lead to suppression of ion cyclotron lines at magnetic fields $B \sim 10^{14}$ G. Atmosphere models including this effect have been also computed by van Adelsberg and Lai (2006). Because very strong magnetic field can increase the binding energy of atoms and molecules, these bound state may be also present in the atmosphere of NSs. Using consistent equation of state and H opacities, partially ionised models of magnetised atmospheres have been computed by different teams (Ho et al., 2003a; Potekhin and Chabrier, 2004). Atmosphere composed by mid-Z element and magnetic fields $B \sim 10^{12} - 10^{13}$ have been studied

by Mori and Ho (2007). Thin H atmospheres above either a condensed surface or He layer were studied by Ho et al. (2007) and Suleimanov et al. (2009), respectively. The effects of cyclotron harmonics were investigated by Suleimanov et al. (2012). A recent review of the topic can be found in Potekhin et al. (2015a).

Magnetised atmospheric models follow the same approach of the non-magnetic ones for calculating the emergent spectrum. The main difference is in the radiative calculations, that are typically computed under the two-normal mode approximation, i.e., the radiation propagates in the O-mode and X-mode (see Section 1.6.1.1).

A strong magnetic field introduces an anisotropy in the opacities and makes them different for electromagnetic waves propagating in different normal modes. Thus, the transport of radiation has to to be solved in terms of two coupled differential equations for the intensities I_ν^1 and I_ν^2,

$$\mu \frac{\partial I_\nu^j(\tau,\mu)}{\partial \tau} = \frac{\kappa_j^{tot}}{\kappa_T}\left[I_\nu^j(\tau,\mu) - S_\nu^j(\tau,\mu)\right] \tag{1.28}$$

where $j = 1,2$ now specify the normal mode in which the intensity is calculated, $\kappa_j^{tot} = \kappa_j^{ff} + \kappa_j^s$ is the total opacity and κ_T is the Thompson scattering opacity. Here, we use $\mathrm{d}\tau = -\rho\,\kappa_T \mathrm{d}z$, and the source function can be written as (van Adelsberg and Lai, 2006)

$$S_\nu^j(\mu) = \frac{\kappa_j^{ff}(\mu)}{\kappa^{tot}(\mu)}\frac{B_\nu}{2} + \frac{2\pi}{\kappa_j^{tot}(\mu)}\sum_{i=1}^{2}\int_{-1}^{1}\mathrm{d}\mu' \frac{\mathrm{d}\kappa_{ij}^s(\mu',\mu)}{\mathrm{d}\Omega} I_\nu^i(\mu'). \tag{1.29}$$

The last term in the source function contains the process in which a photon can be scattered from one to another mode, and introduces the coupling of the two radiative transfer equations.

The radiative transfer equation has to be solved together with the hydrostatic and radiative equilibrium equations. The last one is given by

$$\int_0^\infty \mathrm{d}\nu \sum_{j=1}^{2} \kappa_j^{ff}\left(\frac{B_\nu}{2} - J_\nu^j\right) = 0, \tag{1.30}$$

where $J_\nu^j \equiv (1/2)\int_{-1}^{1}\mathrm{d}\mu I_\nu^j(\mu)$ is the mean specific intensity associated to mode j.

Similarly, the condition for and constant flux through the atmosphere is now given by

$$\sum_{j=1}^{2}\int_0^\infty \mathrm{d}\nu \int_{-1}^{1} \mu I_\nu^j \mathrm{d}\mu = \sigma T_{eff}^4. \tag{1.31}$$

It should be noticed that the intensity I_ν^j now also depends on the angle between the direction of the photon propagation direction and the magnetic field direction θ_B. In general, when a tilted magnetic field direction at the star surface is assumed, the intensity of the radiation has a dependency on the co-latitude, $\mu = \cos\theta$, and azimuthal angle, φ, relative to the normal to the surface.

The usual technique to compute atmospheric models considers as a starting point a temperature profile given by that of a grey atmosphere

$$T(\tau) = T_{eff}\left[\frac{3}{4}\left(\tau + \frac{2}{3}\right)\right], \tag{1.32}$$

followed the computation of the atmosphere structure and the radiative transfer calculation. Since the temperature profile does not satisfy the condition of constant flux through the atmosphere, solutions are found with methods that iteratively correct the temperature profile and re-compute the atmosphere structure plus the radiative transfer calculations.

As an example, Figure 1.7 shows the emergent spectra for a magnetised atmosphere (Zavlin, 2009). Here, the intensities are summed in both normal modes, i.e., $F_\nu = \int_0^1 \mu(I_{\nu,1} + I_{\nu,2})\mathrm{d}\mu$. In particular, two different temperatures and two magnetic field angles (parallel and perpendicular to the NS surface) are considered. The main characteristics for these magnetised spectra can be summarised as follows:

- Like in the case of non-magnetised atmosphere, the spectrum for a pure H magnetised atmosphere shows deviations from a black body, with a spectrum which is harder than a blackbody spectrum at the same temperature. In other words, the spectrum is shifted to higher energies again, mainly due to the properties of the free–free opacity. However, in one of the modes, the free–free opacity is reduced, which produces a less evident shift of the spectrum of a magnetised atmosphere with respect to a backbody one.

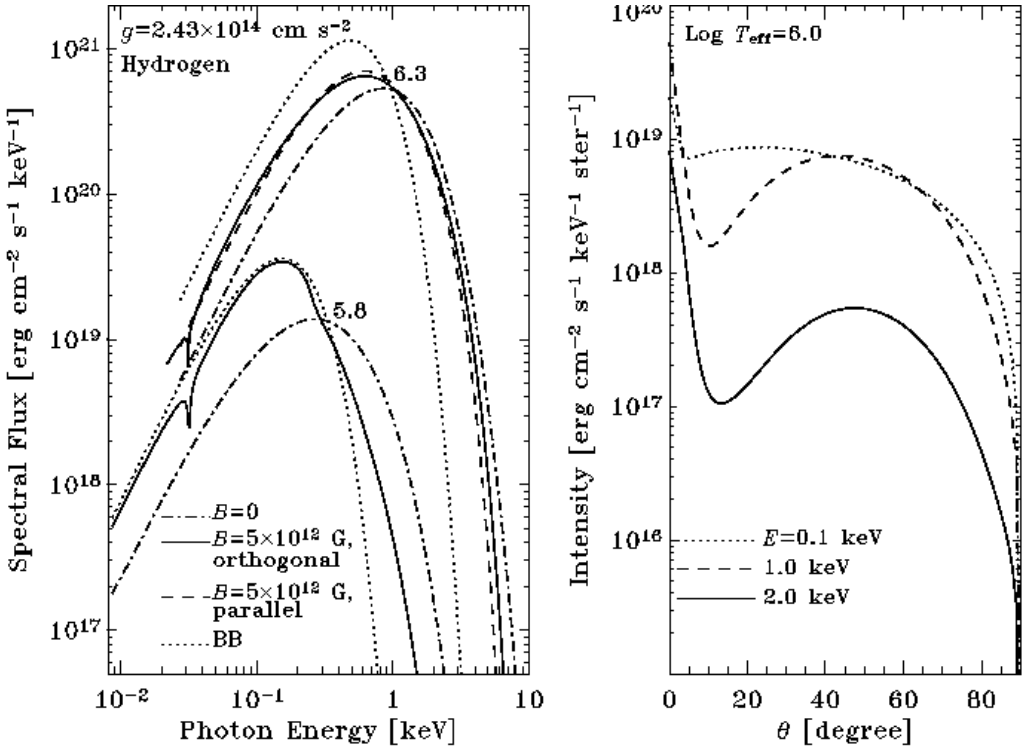

Figure 1.7: Magnetised atmosphere models from Zavlin 2009. Left panel: Emergent spectra for H atmospheres with different effective temperatures and magnetic field configurations. Right: Angular dependence of the intensity at temperature $\log T_{eff} = 6.0$ for different photon energies.

- Due the strong magnetic field now the X–ray spectrum exhibits an absorption line at the ion cyclotron frequency, which for $B = 5 \times 10^{12}$ G is located at $E_{ci} = 30$ eV. The electron cyclotron absorption line does not affect the soft X–ray spectra because it is located at higher energies, $E_{ce} = 11.6(B/10^{12}G)$ keV. However, for magnetic fields $B \sim 10^{11}$ G, this absorption line may, indeed, appear in the soft X–ray band.

- The intensities are significantly anisotropic and depend on the direction of the radiation. The anisotropy increases with the photon energy as showed in Figure 1.7, right panel.

Figure 1.8 shows the emergent flux from a strongly magnetised NS. As it can be noticed, for most energies the fluxes in the O-mode are lower than the fluxes in the X-mode. This is caused by the fact that the opacities in the X-mode are sig-

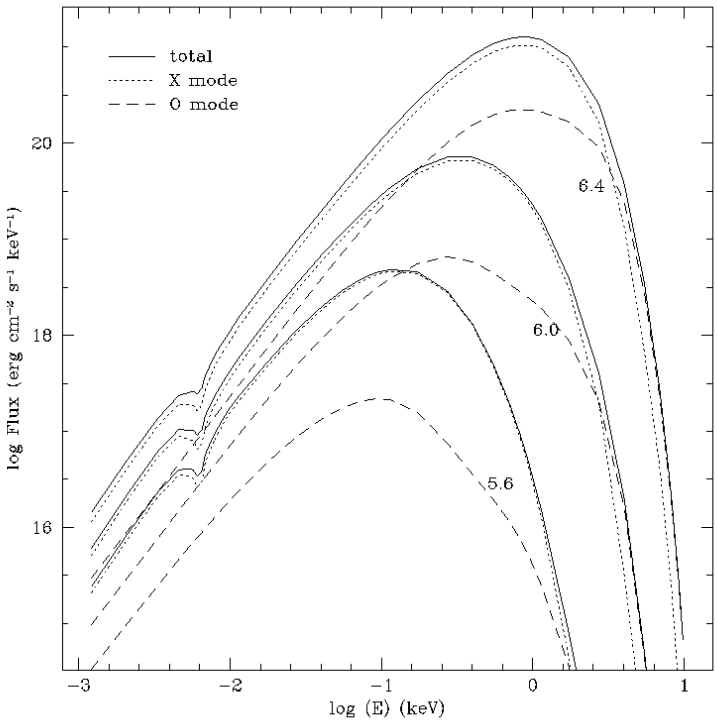

Figure 1.8: Hydrogen magnetised atmosphere models from Lloyd 2003 for magnetic field $B = 10^{12}$ G and different temperatures. The solid line shows the spectrum considering the total flux. The dashed and dotted lines show the flux in the O-mode and X-mode, respectively.

nificantly lower than the opacities in the O-mode. As a consequence, the emission from strongly magnetised atmospheres is expected to be highly polarised (with a polarisation dependence that becomes smaller at higher energies).

1.6.4 Emission from a condensed surface

A very strong magnetic field can change the properties of atoms making the electrons confined in the direction perpendicular to the magnetic field. These elongated, cylindrical atoms can form molecular chains by covalent bonding along the magnetic field lines. In turn, chain–chain interaction can lead to a condensate state of the matter. The cohesive energies for linear chains increase with the magnetic field strength (Lai, 2001; Medin and Lai, 2007). Therefore, it is expected that for sufficiently strong magnetic fields there is a critical temperature, T_{crit}, that characterises a phase transition between a gaseous and a condensed state. This temper-

ature increases with the magnetic field. The most recent rough estimation gives $T_{crit} \approx (5+2B_{13}) \times 10^5$ for Fe composition (Potekhin et al. 2012 and references therein). For $B > 13$ G, the phase transition may occur for surface temperatures as high as $T \sim 10^6$ K. Thus, for typical surface temperatures and magnetic fields found in XDINSs, at least if the star has not accreted substantial H, it is not unrealistic to consider that the thermal spectrum may be emitted directly from a condensate surface (Turolla et al., 2004).

The NS surface can condensate like a dense metallic surface. Because of this, plasma effects become important to describe the radiative properties of the metallic layer. Unlike the case of non-magnetised plasma, in which electromagnetic propagation is not possible under the electron plasma frequency, in a strongly magnetised condensed surface the electron cyclotron frequency modifies the dispersion relation of the medium, which allows the surface to radiate even under the plasma frequency.

The approach to calculate the emergent spectrum from a condensate surface reduces to calculate its emissivity, which in turn depends on the reflective properties of the surface (or reflectivity of the surface). The latter one can be calculated using the standard approach for the reflection and transmission of an electromagnetic wave at a plane surface between two media with different dielectric properties.

Lets consider a NS (with condensate surface) inside a cavity in thermodynamic equilibrium with a blackbody radiation field B_ν. Following van Adelsberg et al. (2005), for the incident unpolarised radiation, the electric field of an electromagnetic wave can be written in terms of the sum of two independent polarisation states: $\mathbf{E}_1^{(i)} = A\mathbf{e}_1^{(i)}$ and $\mathbf{E}_2^{(i)} = A\mathbf{e}_2^{(i)}$, where $A = (B_\nu/2)^{(1/2)}$, and $\mathbf{e}_1^{(i)}$ and $\mathbf{e}_2^{(i)}$ correspond to the polarisation eigenvectors of the incident wave. This wave is partially reflected and partially transmitted. The reflected field can be written as

$$\begin{aligned} \mathbf{E}_1^{(r)} &= A\left(r_{11}\mathbf{e}_1^{(r)} + r_{12}\mathbf{e}_2^{(r)}\right), \\ \mathbf{E}_2^{(r)} &= A\left(r_{21}\mathbf{e}_1^{(r)} + r_{22}\mathbf{e}_2^{(r)}\right), \end{aligned}$$

where $\mathbf{E}_1^{(r)}$ and $\mathbf{E}_2^{(r)}$ are the reflected electric fields from the incident field $\mathbf{E}_1^{(i)}$ and $\mathbf{E}_2^{(i)}$, respectively. Since the intensity is proportional to the square of the electric field amplitude, the electric field of the reflected intensities for $\mathbf{E}_1^{(r)}$ and $\mathbf{E}_{\mathbf{2}}^{(\mathbf{r})}$ are given by

$$\begin{aligned} I_{\nu 1}^{(r)} &= \frac{1}{2}\left(|r_{11}|^2+|r_{21}|^2\right)B_\nu = \frac{1}{2}R_1 B_\nu, \\ I_{\nu 2}^{(r)} &= \frac{1}{2}\left(|r_{12}|^2+|r_{22}|^2\right)B_\nu = \frac{1}{2}R_2 B_\nu. \end{aligned}$$

Since in the cavity the radiation field has a blackbody distribution, the intensity of the radiation emitted by the surface in the direction of the reflected wave with polarisations $\mathbf{E}_{\mathbf{1}}^{(\mathbf{r})}$ and $\mathbf{E}_{\mathbf{2}}^{(\mathbf{r})}$ is

$$\begin{aligned} I_{\nu 1}^{(e)} &= \frac{1}{2}B_\nu - I_{\nu 1}^{(r)} = \frac{1}{2}(1-R_1)B_\nu, \\ I_{\nu 2}^{(e)} &= \frac{1}{2}B_\nu - I_{\nu 2}^{(r)} = \frac{1}{2}(1-R_2)B_\nu. \end{aligned}$$

These expressions are valid even when the body (i.e., the crust) is not in thermodynamic equilibrium with the radiation field. The total emission of the crust is given by

$$I_\nu^{(e)} = (1-R)B_\nu(T) = JB_\nu(T), \tag{1.33}$$

where $R = \frac{1}{2}(R_1+R_2)$ is the reflectivity and $J = 1-R$ is the emissivity.

In order to calculate the reflectivity of the surface it is necessary to obtain the electric fields of the reflected wave. They can be obtained by the Snell law, which links the refraction angles of the transmitted wave with the index of refraction of the surface (they, in turn, depend on the dielectric tensor), and by imposing the boundary conditions between the media with different dielectric tensors. These boundary conditions express the continuity of the normal components **D** and **B**; and the continuity of the tangential components of **E** and **H**.

The main problem in the computation of the emissivity from a condensate and

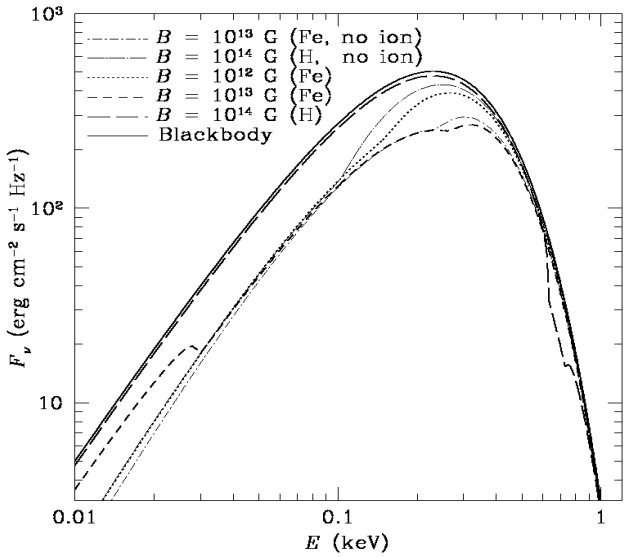

Figure 1.9: Spectra from a condensate surface with temperature $T = 10^6$ K (van Adelsberg et al., 2005). Different lines show spectra for condensate surface with different composition and magnetic field strength (normal to the surface). The lines labelled "no ion" show the case in which motions of ions are neglected in the dielectric tensor. For comparison, the solid line shows a blackbody spectrum.

magnetised NS surface is that the associated dielectric tensor is poorly known. For example, one of the difficulties is that the dielectric tensor depends on the conductivity, for which the interactions between phonons (lattice vibration) and electrons are expected to be relevant. In addition, the strong magnetic field in the crust complicates the electron "transport", making it anisotropic; charges can move freely along **B** but the motion perpendicular to the field is quantised (Turolla et al., 2004). However, expressions for the dielectric tensor can be derived in two limiting cases that depend on the response of the medium to an electromagnetic wave:

- **"Fixed ions"** limit i.e, when only electrons in the condensate respond to an incident electromagnetic wave but ions are not affected because of their relatively strong Coulombian interactions.

- **"Free ions"** limit i.e., when both electrons and ions fully respond to an incident electromagnetic wave as Coulombian interactions are relatively week (so they can be neglected).

The realistic reflectivity of the surface should be between both limits.

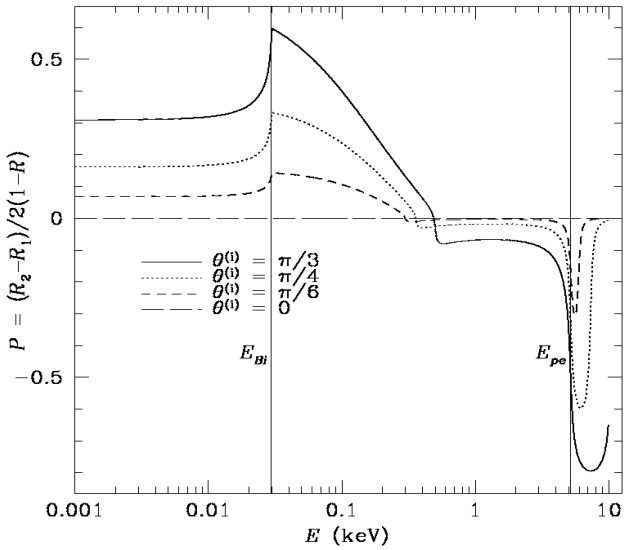

Figure 1.10: Degree of polarisation for a Fe condensate NS surface with magnetic field $B = 10^{13}$ G (van Adelsberg et al., 2005). The magnetic field direction is normal to the surface. The different curves show the polarisation degree for different azimuthal angles (between photon direction and the normal to the surface).

Figure 1.9 shows the emergent spectra for the H and Fe condensate surface. In general, the fluxes are reduced compared to the case of a blackbody. However, for a particular case of an H condensate surface with $B = 10^{14}$ G the emergent spectrum is just slightly suppressed with respect to a blackbody spectrum. As in the magnetised atmospheric model, the emission is different for different propagation modes, which effect produces a polarised emission. Figure 1.10 shows the degree of polarisation for an Fe condensate surface for radiation at different azimuthal angles. The polarisation increases as the direction of the radiation becomes perpendicular to the magnetic field and the photon energy tends toward the ion and electron cyclotron energies.

The concepts described here will be the basis of my work in calculating polarisation properties and transport of radiation in magnetised sources, described in the next chapters.

Chapter 2

Polarised thermal emission from XDINSs

This chapter is devoted to the study of the polarisation properties of XDINSs. I present theoretical models considering either thermal emission from a magnetised atmosphere or condensed metallic surface. In particular, the models account for QED vacuum birefringence operating in the NS magnetosphere, as well as light bending i.e., a general relativity effect due to the strong gravitational field of the NS. The aim is to prove the power of polarimetry to test the properties of the matter and vacuum under strong magnetic fields. I model a representative source: RX J1856.5–3754, the nearest and brightest XDINS. It is demonstrated that, indeed, by performing combined optical and X-ray polarimetry it is possible to establish whether XDINSs have gaseous atmosphere or condensed surfaces. This result is relevant, as it provides a new scientific case for future missions of X-ray polarimetry.

This chapter is organised as follows. First, the properties of vacuum birefringence are discussed and the concept of adiabatic radius is introduced. Then, the ray tracing method and the rotation of the Stokes parameters needed to compute to polarisation properties are explained. Next, I compute the polarisation properties for RX J1856.5–3754, considering different surface emission models and a dipolar magnetic field topology, which also set the temperature distribution over the whole NS surface. Finally, the chapter is closed with a summary and discussion of the

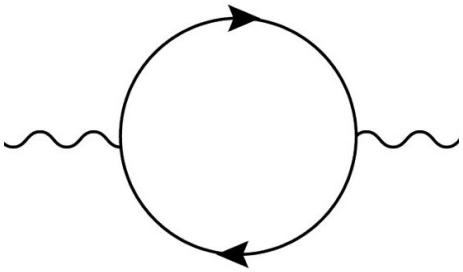

Figure 2.1: Feynman diagram for vacuum polarisation in a magnetic field. Wavy line correspond to photons and and circle lines correspond to virtual e^+ or e^- (source: wikimedia commons)

main results.

2.1 QED vacuum birefringence

A notable effect derived from QED is the polarisation of the vacuum under a strong magnetic field. Photons propagating in the magnetised vacuum can interact with the background field via the creation of virtual electron positron pairs, e^+e^- (Fig. 2.1), and those virtual pairs can modify the dielectric and the magnetic permeability tensors of the vacuum (Mészáros, 1992). In this regime, the Lagrangian from which the equations of electromagnetism are obtained is not longer linear. Expanded up to second order in the fine structure constant α, the Lagragian including QED vacuum correction is given by (Heisenberg and Euler, 1936)

$$\mathscr{L} \simeq \underbrace{\frac{1}{2}(\mathbf{E}^2 - \mathbf{B}^2)}_{\text{Classical Lagrangian}} + \underbrace{\frac{2\alpha^2}{45}\frac{(\hbar/mc^3)}{mc^2}\left[(\mathbf{E}^2 - \mathbf{B}^2)^2 + 7(\mathbf{E}\cdot\mathbf{B})^2\right]}_{\text{QED vacuum correction}},$$

where $\mathbf{E}$ and $\mathbf{B}$ correspond to the total electric and magnetic fields (wave field plus external field), respectively. Defining $E_i = E_i^w$ and $B_i = B_i^w + B_i^e$, where w and e label the wave and external field, respectively, the response of the vacuum can be found by the constitutive equations $D_i = 4\pi\partial\mathscr{L}/\partial E_i$ and $H_i = -4\pi\partial\mathscr{L}/\partial B_i$. By linearising these equations with respect to the wave fields, one obtains the $\mathbf{D}^w$ and

$\mathbf{H}^w$ fields, which are related to $\mathbf{E}^w$ and $\mathbf{B}^w$ by $D_i^w = \varepsilon_{ij} E_j^w$ and $H_i^w = \mu_{ij}^{-1} B_j^w$. These equations, in turn, define the dielectric and permeability tensors for the vacuum (Mészáros, 1992),

$$\varepsilon_{ij} = \delta_{ij}(1+2\delta) + \delta b_i b_j \tag{2.2}$$

$$\mu_{ij}^{-1} = \delta_{ij}(1+2\delta) - 4\delta b_i b_j, \tag{2.3}$$

where

$$\delta = \frac{\alpha^2}{45\pi}\left(\frac{B}{B_Q}\right)^2 = 0.5\times 10^{-4}\left(\frac{B}{B_Q}\right)^2 \tag{2.4}$$

quantifies the deviation from unity (actually from the unit matrix δ_{ij} or Kronecker delta) of the dielectric and permeability tensors due to the QED vacuum, $\hat{\mathbf{b}}$ is the unitary vector along the external magnetic field, and B_Q.

By solving the Maxwell equations of the sourceless radiation field (without charges or electric currents), it can be found that for a plane electromagnetic wave $\mathbf{E} = \hat{\mathbf{e}} e^{i(\mathbf{k}\cdot\mathbf{r}-\omega t)}$, the two propagation eigenmodes are given by (Mészáros, 1992)

$$\hat{\mathbf{e}}_\perp = \mathbf{k}\times\hat{\mathbf{b}} \tag{2.5}$$

$$\hat{\mathbf{e}}_\parallel = n_\parallel^{-1} a^{-1}\hat{\mathbf{b}} - n_\parallel a^{-1}\mathbf{k}\cdot\hat{\mathbf{b}}\mathbf{k} \tag{2.6}$$

where the refractive indices associated to each mode are given by

$$n_\perp = 1 + 2\delta\sin^2\theta \tag{2.7}$$

$$n_\parallel = 1 + (7/2)\delta\sin^2\theta. \tag{2.8}$$

Here, $\parallel$ and $\perp$ label the wave electric vector parallel and perpendicular to the external magnetic field, respectively.

The properties of the external region of a NS, where the electron number density is $n_e < 10^{20}$ cm^{-3} and the magnetic field can be $B > 10^{12}$ G, for electromagnetic waves in the X-ray range ($\omega \sim 10^{18}$ Hz), can be summarised as follows

- The departure from unity of the dielectric (and permeability) tensor due to

QED vacuum for fields $(B/B_Q) > 10^{-1}$ is of the order of 10^{-6}. Therefore, in the external region of the NS, QED vacuum effects can easily dominate over plasma effects, which can be quantified as $(\omega_p/\omega)^2 \sim 3 \times 10^{-7}(\omega/10^{18}\ \mathrm{Hz})^{-2}(\mathrm{n}/10^{20}\ \mathrm{cm}^{-3})$.

- The normal modes are linearly polarised, with the directions of the polarisation vectors either parallel or perpendicular to the external magnetic field.

- The refractive indices for the normal modes in the the magnetised vacuum are $n_{\parallel} \neq n_{\perp}$. Then, the vacuum becomes birefringent, even when a plasma is not present, and electromagnetic waves in different polarisation modes travel with different speed.

Vacuum birefringence is expected to modify the polarisation of the surface radiation as photons propagate thought the NS magnetosphere. The method used to quantify its effects is explained in the following sections.

2.2 Adiabatic Radius

The normal modal description in vacuum holds for photon energies below the electron cyclotron energy $E < E_{ce} = \hbar eB/m_e c \simeq 11.6(B/10^{12}\mathrm{G})$ keV (Gnedin and Pavlov, 1974), which implies $B \gtrsim 10^{11}$ G at X-ray energies, whereas B can be as low as $\sim 10^{10}$ G in the optical band. The topology and strength of the magnetic field, however, are expected to change as photons propagate across the NSs magnetosphere as well as the dielectric, ε, and magnetic permeability, μ, tensors of vacuum (Heyl and Shaviv, 2000, 2002).

To account for the effect of vacuum birefringence around the NS, the evolution of the radiation is obtained by solving the wave equation

$$\nabla \times (\mu \cdot \nabla \times \mathbf{E}) = \frac{\omega^2}{c^2}\varepsilon \cdot \mathbf{E} \tag{2.9}$$

In particular, for a reference frame (x, y, z) with the z-axis along the photon propagation direction k, and the x-axis perpendicular to both k and the local magnetic field

B, the evolution of the amplitude of the electromagnetic wave $\mathbf{E} = \mathbf{A}(z)e^{i(kz-\omega t)}$ is given by (Heyl and Shaviv 2002; Fernández and Davis 2011; Taverna et al. 2015)

$$\begin{aligned} \frac{\mathrm{d}A_x}{\mathrm{d}z} &= \frac{\mathrm{i}k_0\delta}{2}(MA_x + PA_y) \\ \frac{\mathrm{d}A_y}{\mathrm{d}z} &= \frac{\mathrm{i}k_0\delta}{2}(PA_x + NA_y)\,. \end{aligned} \tag{2.10}$$

Here $\mathbf{A} = (A_x, A_y) = (a_x \mathrm{e}^{-\mathrm{i}\varphi_x}, a_y \mathrm{e}^{-\mathrm{i}\varphi_y})$ is the electric field complex amplitude, $k_0 = \omega/c$ with ω the photon angular frequency and the adimensional quantities δ, M, N and P (Fernández and Davis, 2011) depend on the (local) magnetic field strength.

From equations (2.10) one obtains the typical lengthscale over which vacuum polarisation induces a change in the electric field $\ell_\mathrm{A} = 2/k_0\delta \simeq 100(B/10^{11}\,\mathrm{G})^{-2}(E/1\,\mathrm{keV})^{-1}\,\mathrm{cm}$, where $E = \hbar\omega$. By comparing this lengthscale with the typical lengthscale of the variation of the magnetic field along the photon trajectory $\ell_\mathrm{B} = B/|\hat{k}\cdot\nabla B| \sim r$, where r is the radial distance, three regions with different properties can be identified around the NS:

- Near to the star surface, where $\ell_\mathrm{A} \ll \ell_\mathrm{B}$, the direction along which the wave electric field oscillates can instantaneously adapt to the variation of the local magnetic field direction, maintaining the original polarisation state. In these conditions, the photon is said to propagate adiabatically and in the following this region will be referered as the *adiabatic region*.

- As the photon moves outwards the magnetic field strength decreases ($B \propto r^{-3}\sqrt{1+3\cos^2\theta}$ for a dipole field, where θ is the magnetic colatitude) and ℓ_A increases. Thus, the condition $\ell_\mathrm{A} \sim \ell_\mathrm{B}$ determines a region in which the wave electric field can not promptly follow the variation of the magnetic field any more, and the normal mode description is no longer valid.

- In the external region where $\ell_\mathrm{A} \gg \ell_\mathrm{B}$, the electric field direction freezes and the polarisation state of photon is fixed.

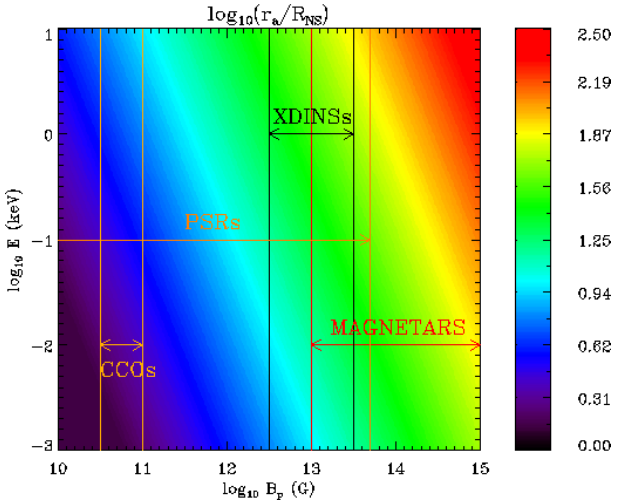

Figure 2.2: Contour plot showing the adiabatic radius $r_{\rm a}$ (in units of the stellar radius $R_{\rm NS}$) as a function of the polar magnetic field strength and the photon energy (Taverna et al., 2015). The typical $B_{\rm P}$-ranges for different classes of neutron stars, the magnetars, the isolated, thermally emitting NSs (XDINSs), the radio-pulsars (PSRs) and the central compact objects (CCOs), are also shown.

In principle, the evolution of the polarisation modes should be calculated integrating equations (2.10) from the surface up to infinity (or, at least, up to a distance sufficiently large to consider the complex amplitude components A_x and A_y as constants). This has been the approch followed, for example, by Heyl et al. (2003, see also Fernández and Davis 2011; Taverna et al. 2014). However, this requires quite long computational times as numerical integration must be performed along each ray, which is not particularly suited for a systematic study of how the polarisation observables depend on the various physical and geometrical parameters. In order to overcome this problem, in the following only the adiabatic region and the external one are considered, assuming that they are divided by a sharp edge. To this end we introduce the adiabatic radius[1] $r_{\rm a}$, defined implicitly by the condition $\ell_{\rm A} = \ell_{\rm B}$. Assuming a dipole field and purely radial photon trajectories, $\ell_{\rm B} = r/3$ and hence $\ell_{\rm A}(r_{\rm a}) = r_{\rm a}/3$. Recalling the expression for $\ell_{\rm A}$, it follows that $r_{\rm a}/R_{\rm NS} \simeq 3.9\times10^{-4}(E/1\ {\rm keV})^{-1}(B_{\rm P}/10^{11}\ {\rm G})^{-2}(R_{\rm NS}/r_{\rm a})^{-6}$ and finally (Taverna et al., 2015)

[1] This same quantity is called the polarisation-limiting radius, $r_{\rm pl}$, in previous literature (see Heyl and Shaviv, 2002).

$$r_{\rm a} \simeq 4.8 \left(\frac{B_{\rm P}}{10^{11}\,{\rm G}}\right)^{2/5} \left(\frac{E}{1\,{\rm keV}}\right)^{1/5} R_{\rm NS}\,, \tag{2.11}$$

where $R_{\rm NS}$ is the stellar radius, $B_{\rm P}$ is the polar strength of the dipole and $\cos\theta \sim 1$ is assumed. The adiabatic radius depends on both the photon energy and the star magnetic field: it is larger for stars with stronger magnetic field, and, at fixed $B_{\rm P}$, it becomes smaller for less energetic photons, as shown in Figure 2.2.

2.3 Ray tracing method

NSs are expected to have both a varying temperature and varying magnetic field distribution over the surface. Given an emission model characterised by a specific intensity I_ν, which in general depends on the photon frequency ν and direction $\mathbf{k}$, and on the position on the star surface, the spectral and polarisation properties at infinity are obtained by summing the contributions of the surface elements which are into view at a given rotational phase. The ray tracing method used to compute these properties is explained below.

Following Zane and Turolla (2006, see also my work in Taverna et al. 2015 for further details), two angles χ and ξ are defined: the former is the angle between the line-of-sight (LOS, unit vector $\boldsymbol{\ell}$) and the spin axis ($\mathbf{p}$), while the latter is that between the magnetic (dipole) axis ($\mathbf{b}_{dip}$), and the spin axis. Then, two coordinate system are also defined:

- A fixed (observer) coordinate system, (X,Y,Z), with the Z-axis parallel to $\boldsymbol{\ell}$ (i.e. along the LOS) and the X-axis in the $(\boldsymbol{\ell},\mathbf{p})$ plane. The associated polar angles to this coordinate system are $(\Theta_{\rm S},\Phi_{\rm S})$. In this system, the cartesian components of $\mathbf{p}$ and $\mathbf{b}_{dip}$ are $\mathbf{p} = (\sin\chi, 0, \cos\chi)$ and $\mathbf{b}_{dip} = (\sin\chi\cos\xi - \cos\chi\sin\xi\cos\gamma, \sin\xi\sin\gamma, \cos\chi\cos\xi + \sin\chi\sin\xi\cos\gamma)$, where $\gamma = \omega t$ is the phase angle ($\omega = 2\pi/P$, and P is the star rotational period).

- A co-rotating coordinate system, (x,y,z), in which the north and south poles coincide with the magnetic poles and the z-axis is parallel to $\mathbf{b}_{dip}$ (the x-axis is defined below). Here, the polar angles are (θ,ϕ), respectively. An additional

vector $\mathbf{q} = (-\cos\chi\cos\gamma, \sin\gamma, \sin\chi\cos\gamma)$ is defined, which corresponds to a unit vector orthogonal to $\mathbf{p}$ and rotating with angular velocity ω (in the fixed frame). The x-axis of the rotating coordinate system is then chosen in the direction of the component of $\mathbf{q}$ perpendicular to $\mathbf{b}_{dip}$,

$$\mathbf{q}_\perp = \frac{\mathbf{q} - (\mathbf{b}_{dip}\cdot\mathbf{q})\mathbf{b}_{dip}}{\left[1-(\mathbf{b}_{dip}\cdot\mathbf{q})^2)\right]^{1/2}}\,. \tag{2.12}$$

The transformations linking the pairs of polar angles in the two systems are (Zane and Turolla 2006; Taverna et al. 2015)

$$\begin{aligned} \cos\theta &= \mathbf{b}_{dip}\cdot\mathbf{n} \\ \cos\phi &= \mathbf{n}_\perp\cdot\mathbf{q}_\perp \end{aligned} \tag{2.13}$$

where $\mathbf{n} = (\sin\Theta_S\cos\Phi_S, \sin\Theta_S\sin\Phi_S, \cos\Theta_S)$ is the radial unit vector in the fixed coordinate system and $\mathbf{n}_\perp$ is defined in analogy with $\mathbf{q}_\perp$. Equations (2.13) are needed to express the intensity (naturally written in terms of the magnetic coordinate angles $(\theta\,,\phi)$), in terms of the polar angles of the fixed frame $(\Theta_S\,,\Phi_S)$ over which integration is performed. Notice that, in general, an additional coordinate system is needed to compute the ray tracing for a surface slab emitting anisotropic radiation, as expected for local magnetic field tilted by an arbitrary angle with respect to the vector normal to the surface. This is going to be explained in §2.5, where the emission models are discussed in more detail.

Once the fixed and rotating coordinate system are linked, the monochromatic flux (at each phase) detected by an observer at distance $D \gg R_{NS}$ is obtained by integrating the intensity I_ν (in the fixed coordinate system) over the visible part of the surface (Page, 1995; Zane and Turolla, 2006)

$$F_\nu(\gamma) = \left(1-\frac{R_s}{R_{NS}}\right)\frac{R_{NS}^2}{D^2}\int_0^{2\pi} d\Phi_S \int_0^1 I_\nu(\mathbf{k},\theta,\phi)du^2\,, \tag{2.14}$$

where $u = \sin\bar{\Theta}$. The two angles, Θ_S and $\bar{\Theta}$, are related by the "ray tracing" integral

$$\bar{\Theta} = \int_0^{1/2} d\varphi \, \sin\Theta_S \left[\frac{1}{4}(1-x) - (1-2\varphi x)\varphi^2 \sin^2\Theta_S\right]^{-1/2}, \tag{2.15}$$

which accounts for light bending, a general relativity effect caused by the intense gravitational field around the NSs. For $x \ll 1$ Newtonian geometry is recovered and $\bar{\Theta} = \Theta_S$. Notice that in the "ray tracing" integral we consider a Schwarzschild spacetime, and frame-dragging is no account for as for NSs with spin periods $\gtrsim 1$ s its effect is negligible.

In the case of radiation (linearly) polarised in the two normal modes (the O-mode and X-mode), the total intensity is just the sum of the intensities in the two modes

$$I_\nu(\mathbf{k},\theta,\phi) = I_{\nu,O}(\mathbf{k},\theta,\phi) + I_{\nu,X}(\mathbf{k},\theta,\phi) \tag{2.16}$$

and we define the "intrinsic" degree of polarisation, i.e. that at the source, as

$$\Pi_L^{EM} = \frac{F_X - F_O}{F_X + F_O}, \tag{2.17}$$

where $F_{X,O}$ is the monochromatic, phase-dependent flux in each mode, defined as in equation (2.14). This expression, implicitly consider a uniform magnetic field distribution over the star surface. However, notice that for a given surface element, the normal modes computed in our atmospheric or crustal model are defined with respect to a reference frame that depends on the local direction of the magnetic field. To take into account a varying magnetic field over the star surface, a proper calculation of the degree of polarisation requires a rotation of the local reference frames (for the normal modes) to the common reference frame of a polarimeter. A discussion about this can be found in Pavlov and Zavlin (2000). Instead, in the following, this rotation will be performed at the adiabatic radius, since in this way it is possible to account for QED effects. This is explained in the next section.

2.4 Stokes parameters and vacuum birefringence

The evolution of the wave electric field can be followed by solving the (linearised) wave equation in the magnetised vacuum around the star, along each photon trajectory. However, as discussed in Section §2.2, the main effects of vacuum polarisation can be accounted for by using a simpler approach in which adiabatic propagation (i.e. mode locking) is assumed up to $r_{\rm a}$, while the wave electric field direction is constant for $r > r_{\rm a}$. In this approach, the polarisation properties are determined by the direction of the star magnetic field at $r_{\rm a}$, in addition to the intrinsic polarisation degree at the surface (which depends on the emission model, see Section §2.5).

Since the X- and O- modes are defined according to the direction of the wave electric field with respect to the plane defined by the star magnetic field **B** and the wavevector **k**, the Stokes parameters of the photons crossing $r_{\rm a}$ at different positions are, in general, defined with respect to different coordinate systems. While the z_i' axes for the photon trajectory coincide with the LOS (i.e. with $\boldsymbol{\ell}$), the two axes, x_i', y_i', in the plane orthogonal to $\boldsymbol{\ell}$ will be different for each photon trajectory, because **B** changes its direction over the sphere of radius $r_{\rm a}$. In order to derive the polarisation observables as detected by a distant instrument, the Stokes parameters must be referred to the same fixed direction, **u**, in the plane perpendicular to the LOS. This is done by rotating the Stokes parameters by an angle $\alpha_i = \arccos \mathbf{u}\cdot\mathbf{x}_i$ photon by photon, according to the relations:

$$\begin{aligned} I_i &= \bar{I}_i \\ Q_i &= \bar{Q}_i \cos(2\alpha_i) + \bar{U}_i \sin(2\alpha_i) \\ U_i &= \bar{U}_i \cos(2\alpha_i) - \bar{Q}_i \sin(2\alpha_i)\,. \end{aligned} \tag{2.18}$$

In a strong magnetic field, each photon is 100% polarised either in the X-mode or O-mode[2]. This is conveniently expressed in terms of the (normalised) Stokes parameters of each photon as $\bar{I}_i = 1$, $\bar{Q}_i = \pm 1$ (for X-mode and O-mode photons)

[2]Photons can be circularly polarised if their propagation direction is parallel to the magnetic field. However, due to the non-uniform magnetic field topology of the NS, the presence of circular polarisation in the thermal emission from XDINSs is expected to be negligibly small.

and $\bar{U}_i = 0$ (Taverna et al., 2015). The collective Stokes parameters, i.e. those for the entire radiation field, are simply the sum of the individual parameters. This is immediately generalised to a continuum photon distribution following the same approach as in equation (2.14)

$$\begin{aligned} I &= \int_0^{2\pi} d\Phi_s \int_0^1 du^2 (n_X + n_O) \\ Q &= \int_0^{2\pi} d\Phi_s \int_0^1 du^2 (n_X - n_O)\cos(2\alpha) \\ U &= \int_0^{2\pi} d\Phi_s \int_0^1 du^2 (n_O - n_X)\sin(2\alpha)\,, \end{aligned} \tag{2.19}$$

where $n_{O,X} = I_{O,X}/E$, and Q, U are the fluxes of the Stokes parameters; here I is proportional to the total photon number flux and in (2.19) the constant factor appearing in front of the integral (see equation [2.14]) has been dropped. The α angle contains the information of the magnetic field topology at the adiabatic radius, and it depends on Θ_s, Φ_s, ξ, χ, the phase γ and the photon energy, E. Finally, the observed polarisation fraction and polarisation angle are given by the usual expressions

$$\Pi_L = \frac{\sqrt{Q^2+U^2}}{I} \tag{2.20}$$

$$\chi_P = \frac{1}{2}\arctan\left(\frac{U}{Q}\right). \tag{2.21}$$

2.5 Emission models

The polarisation properties of the the thermal emission from XDINSs are studied for the case of an atmosphere and condensed surface. The numerical method used to obtain the emergent spectrum associated to each emission model is explained below.

2.5.1 Magnetised atmosphere

Atmospheric models have been presented by a number of authors, under different assumptions and accounting for different degrees of sophistication in the description of radiative processes and the plasma composition. The objective of this study is to derive simple expectations for the difference in the polarisation signal emitted in the

case the NS is covered by a gaseous layer (Section §1.6.3) or it is "bare" (Section §1.6.4). Therefore, the assumption of a fully ionised pure H atmosphere is adopted and the complications induced by different compositions and partial ionisation are ignored (for a complete treatment see Potekhin et al. 2014). The emergent intensity is computed using the numerical method presented in Lloyd (2003, see also Lloyd et al. 2003; Zane and Turolla 2006). The code exploits a complete linearisation technique for solving the stationary radiative transfer equations for the two normal polarisation modes in a plane-parallel slab, by including the effect of the magnetic field inclination with respect to the surface normal. The source term accounts for magnetic bremsstrahlung and magnetic Thompson scattering.

The spectral models have four input parameters: the (local) effective temperature T and magnetic field strength, B, the angle between the local magnetic field $\mathbf{B}$ and the surface normal $\mathbf{n}$, $\theta_{\rm B}$, and the surface gravity, g. The code solves for the emergent intensity $I_\nu(\mathbf{k}) \equiv I(E, \mu_{\rm k}, \phi_{\rm k})$ for a range of photon energies $E = h\nu$, photon co-latitudes and azimuthal angles relative to the slab normal, $\theta_{\rm k} = \arccos(\mu_{\rm k})$ and $\phi_{\rm k}$, respectively. The $\phi_{\rm k} = 0$ direction is defined by the projection of the magnetic field on the symmetry planes. It should be noticed that, since the magnetic field introduces an anisotropy in the opacities, the emergent intensity is not symmetric with respect to a rotation around the surface normal but instead it depends on both, $\mu_{\rm k}$ and $\phi_{\rm k}$. For the particular case in which $\theta_{\rm B} = 0$, symmetry with respect to $\phi_{\rm k}$ is restored, so the angular dependence of the intensities is restricted to $\mu_{\rm k}$ only. Moreover, even in the general case $\theta_{\rm B} > 0$, thanks to the symmetry properties of the opacities, the calculation of the emergent spectrum can be restricted to $0 < \phi_{\rm k} < \pi$.

Since we are considering photon energies well below the electron cyclotron frequency, the opacity for O-mode photons is almost unaffected by the magnetic field, while that for X-mode one is substantially reduced (see e.g. Harding and Lai, 2006). Therefore, in general, the emergent intensity of the X-mode is much larger than that of the O-mode, resulting in an emergent radiation with a substantial degree of polarisation. This is illustrated in Figure 2.3, that shows the intrinsic polarisation fraction, as a function of the energy, for a single model, assuming a parallel

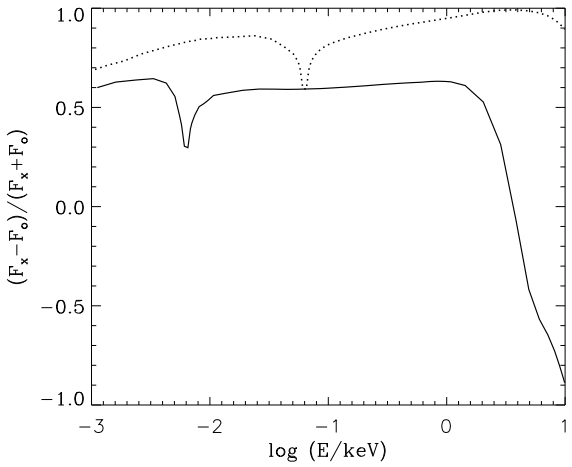

Figure 2.3: Degree of polarisation for emission from a pure H ionised atmosphere with $T = 10^{6.5}$ K and magnetic field perpendicular to the surface (González Caniulef et al., 2016). The solid line corresponds to $B = 10^{12}$ G, and the dotted line to $B = 10^{13}$ G. See text for details.

magnetic field ($\theta_B = 0$). As it can be seen, for $B = 10^{13}$ G, the polarisation fraction is relatively high in the optical band ($\sim 70\%$) and it tends to increase at higher energies.

2.5.2 Condensed surface

As mentioned in Section §1.6.4, there are uncertainties associated to the calculation of the radiation from condensed surfaces. The present knowledge of the condensate is poor, and the lack of a reliable expression of the dielectric tensor hinders the correct derivation of the reflectivity. Previous works adopted a simplified treatment, in which only the limits of "free ions" (no account for the effects of the lattice on the interaction of the electromagnetic waves with ions) and of "fixed ions" (no ion response to the electromagnetic wave because lattice interactions are dominant) were considered. The true reflectivity of the surface is expected to lie in between these two limits.

Here, the same approach is maintained and we use the analytical approximations by Potekhin et al. (2012) to compute the emissivities in the two normal modes. They depend on the magnetic field B, the photon direction $\mathbf{k}$ and energy, and the angle between $\mathbf{k}$ and $\mathbf{B}$, θ_{Bk}. However, the modes 1, 2 of Potekhin et al. (2012) are not

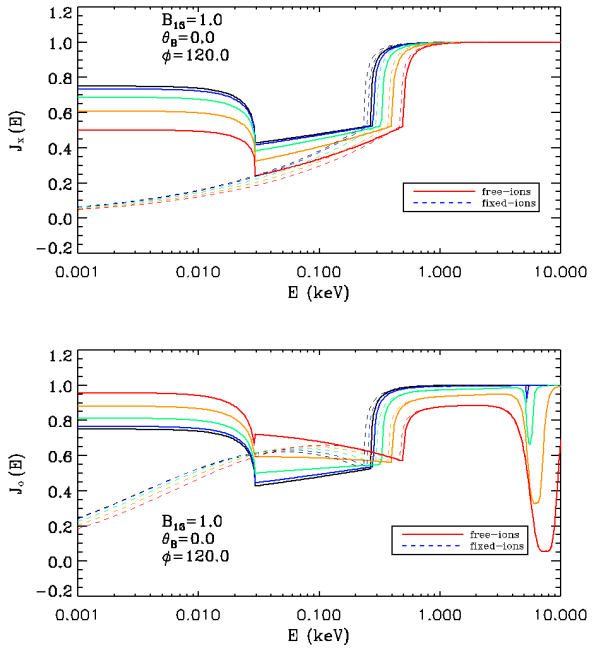

Figure 2.4: The condensed-surface emissivity in the X (top panel) and O mode (bottom panel). Full (dashed) lines refer to the free (fixed)-ions approximation. The different colours are for different values of $\theta_{\rm k}$ (0°, black; 15°, blue; 30°, green; 45°, orange; 60°, red). Here $\phi_{\rm k} = 120°$, $\theta_{\rm B} = 0$ and $B = 10^{13}$ G (González Caniulef et al., 2016).

defined with respect to the local direction of **B** but with respect to the local normal **n**, with mode 1 perpendicular to both **k** and **n**. As a consequence, the emissivities $j_{\nu,\rm i}$ (i $= 1, 2$) do not coincide with those in the X- and O- modes, unless **n** and **B** are parallel, i.e. $\theta_{\rm B} = 0$. The transformation linking the emissivities in the two basis is given in Appendix B of Potekhin et al. (2012)[3]. Once the transformation is performed the intensity of the emergent radiation in the X- and O- modes follows, by assuming the radiance of a blackbody, $B_\nu(T) = 2h\nu^3/[c^2(\exp(h\nu/kT) - 1)]$,

$$I_{\nu,\rm O} = j_{\nu,\rm O}(\nu, B, \mathbf{k}, \theta_{\rm Bk}) B_\nu(T)$$
$$I_{\nu,\rm X} = j_{\nu,\rm X}(\nu, B, \mathbf{k}, \theta_{\rm Bk}) B_\nu(T)\,. \qquad (2.22)$$

[3]Note that there is a typo in equations B.6 of Potekhin et al. (2012), where the array in the left hand side should be a matrix, and B.12, where $\cos^2\theta_{\rm k} - \sin^2\theta_{\rm k}$ should be $\cos^2\theta_{\rm k} + \sin^2\theta_{\rm k} = 1$. These typos have been mentioned and corrected in González Caniulef et al. (2016)

Figure 2.4 shows the emissivity in the two normal modes, calculated in the two limits ("free" and "fixed" ions), for different values of θ_k.

2.6 The model for RX J1856.5-3754

In the following, a NS with mass $M_{NS} = 1.5\,M_\odot$ and radius $R_{NS} = 12$ km is considered, which is compatible with expectations from modern equations of state such as APR or BSk21 models (Akmal et al., 1998; Goriely et al., 2010). The value of the radius is also in agreement with the estimates derived by Sartore et al. (2012) and Ho (2007), assuming a source distance of 120 pc (Walter et al., 2010). This choice translates into a gravitational redshift factor at the star surface $1+z = 1.26$. The rotational period of RX J1856.5-3754 (RX J1856 hereafter) is $P = 7$ s and the X–ray pulsed fraction[4] is the lowest among the XDINSs, $\sim 1.3\%$ (Tiengo and Mereghetti, 2007). The polar strength of the dipole field is taken to be $B_p = 10^{13}$ G, a value which is somehow intermediate between the spin-down measure and the estimates from spectral fitting (van Kerkwijk and Kaplan, 2008; Ho, 2007). It is assumed that the magnetic field is dipolar (see Section §1.3) and that the surface temperature distribution is that induced by the core-centered dipole. Since for fields higher than $\sim 10^{11}$ G, electron conduction across the field lines is strongly suppressed, the meridional temperature variation is $T_{dip} \simeq T_p |\cos\theta_B|^{1/2}$, where T_p is the polar value of the temperature (e.g. Greenstein and Hartke, 1983). This simple expression for T_{dip} differs only slightly ($\lesssim 6\%$) from the more accurate formula by Potekhin et al. (2015b) for $\theta \lesssim 80^\circ$. However, taken at face value, the previous expression for T_{dip} yields vanishingly small values near the magnetic equator. The analysis of Sartore et al. (2012) has shown that the X–ray spectrum of RX J1856 is best modelled in terms of two blackbody components with $kT_h^\infty \sim 60$ eV and $kT_c^\infty \sim 40$ eV. To account for this in a simple way, a temperature profile given by $T_s = \max(T_{dip}, T_c)$ was adopted, with $T_p = T_h$, where $T_{h,c} = T_{h,c}^\infty/(1+z)$.

To compute the case in which the star is surrounded by a gaseous atmosphere, the star surface is divided in six angular patches in magnetic colatitude, centered

[4]Pulsed fraction defined as $pf = \frac{F_{max}-F_{min}}{F_{max}+F_{min}}$, where F_{max} and F_{min} are the the maximum and minimum values of the observed photon flux in the X-ray light curve of the source.

at the values $\theta = \{0°, 10°, 30°, 50°, 70°, 89°\}$. By using the magnetic and temperature profiles previously described, we compute for each θ, the local magnetic field strength, B, the angle $\theta_{\rm B}$ between the magnetic field and the normal to the surface, and hence the temperature, T. Then, a set of atmospheric models is produced for the six θ angles. Since the models are computed using different integration grids in the photon phase space (because the choice of the photon trajectories along which the radiative transfer is solved needs to be optimised to ensure fast convergence at the different values of magnetic field strength and inclination, see Lloyd, 2003), all model outputs are reinterpolated over a common grid. This results in three 4-D arrays for the emergent intensity $I^i_\nu(\mathbf{k},\theta) \equiv I^i(E,\mu_k,\phi_k,\theta)$ $(i = 1,...3)$ which contain the total intensity and the intensities for the ordinary and extraordinary modes, respectively. In order to take into account the emission from the southern magnetic hemisphere of the star, the previous 4-D arrays are redefined with the substitutions $\theta_B \rightarrow \pi - \theta_B$ and $\phi_k \rightarrow \pi - \phi_k$, which is justified by the symmetry properties of the opacities.

The same approach was used to compute the (phase-dependent) spectrum and the polarisation properties for a bare INSs with a condensed surface. In this case the calculation was repeated twice, by assuming either "free" or "fixed" ions. Since the approximated analytical expressions by Potekhin et al. (2012) for the emissivities were adopted, no interpolations were required, contrary to the case of the atmosphere. The fitting formulae, however, cover the range $0 \leq \theta_{\rm B} \leq \pi/2$. In order to take into account the emission from the southern magnetic hemisphere of the star, where $\mathbf{B}$ "enters" into the surface and $\pi/2 < \theta_{\rm B} \leq \pi$, the emissivities are calculated by replacing $\cos\theta_{\rm B}$ with $-\cos\theta_{\rm B}$ and $\cos\phi_{\rm k}$ with $-\cos\phi_{\rm k}$ (A. Potekhin, private communication).

2.6.1 Intrinsic polarisation degree

First, we compute the phase averaged polarisation properties (i.e., averaged over the NS rotation) using equation (2.17). This definition for the polarisation is valid for a uniform magnetic field. Therefore, it is not realistic and should be considered as an "upper limit" for the polarisation signal that could be produced by the emission

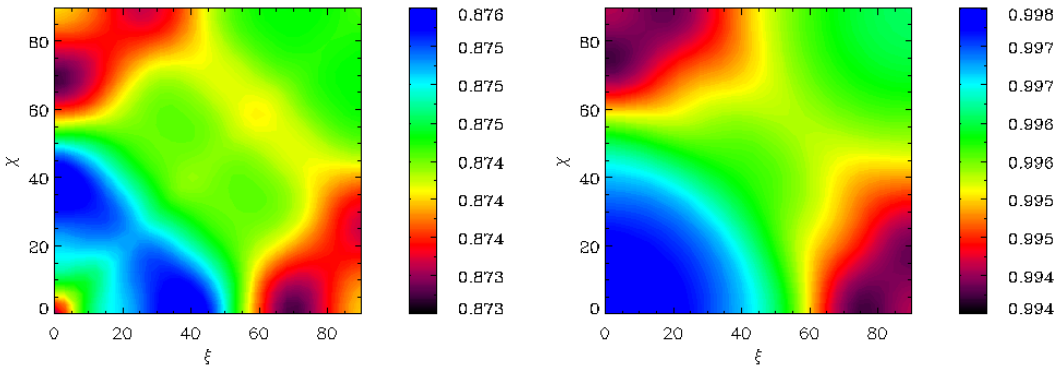

Figure 2.5: Contour plots of the intrinsic, phase-average polarisation fraction in the (χ, ξ) plane for the gaseous atmosphere model, with the left panel for the optical (B-filter) band and the right panel for the X–ray (0.12 - 0.39 keV, at infinity) band. See text for details (González Caniulef et al., 2016).

from the visible part of the NS surface. As it will be discussed later, the magnetic field topology (and the viewing geometry set by the ξ and χ angles) will act as partially "washing down" the polarisation signal.

Figure 2.5 shows the contour plots of the phase-averaged polarisation fraction in the (χ, ξ) plane, for the X–ray $(0.12 - 0.39$ keV) and optical (B-filter) bands. In both cases the phase-averaged polarisation degree is significantly high. The phase-averaged polarisation degree in the X–ray band is $\sim 99\%$, and that in the optical band is only slightly lower, $\sim 87\%$.

Although we take into account relativistic ray bending (i.e. the fact that the emitting area which is into view is larger than a hemisphere), it must be noticed that a proper calculation of the polarisation observables is based on the Stokes parameters and must account for both QED effects in the magnetised vacuum through which photons propagate and the rotation of the plane normal to the photon wavevector in a varying magnetic field topology (see Section §2.4), effects that are not accounted for in the plots of Figure 2.5. We therefore refer to this quantity as the "intrinsic" degree of linear polarisation, to distinguish it from the observed one, which is discussed later on (see Section §2.7). In some sense, this is the "intrinsic" polarisation of each surface patch only due to the emission properties of the atmosphere, and simply adding the patches together is only justified in the unrealistic case in which the magnetic field is constant over the star in both, strength and

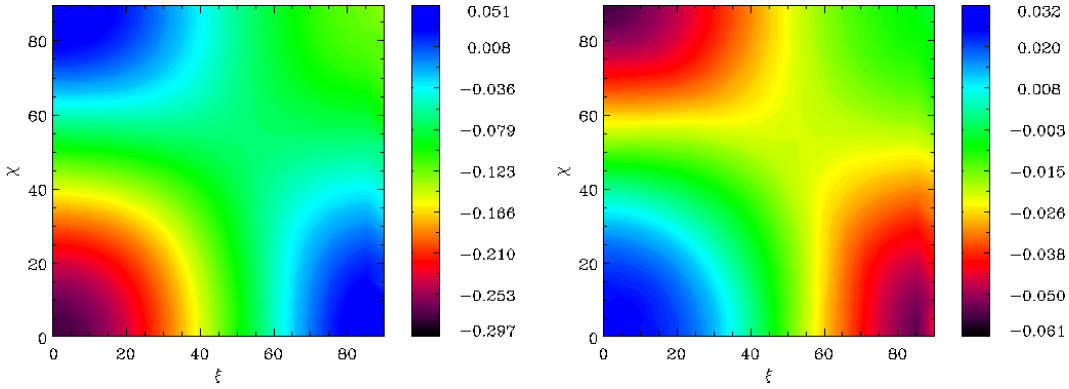

Figure 2.6: Contour plots of the intrinsic, phase-average polarisation fraction in the (χ, ξ) plane for the free ion crustal emission model, with the left panel for the optical (B-filter) band and the right panel for the X–ray (0.12 - 0.39 keV) band (González Caniulef et al., 2016).

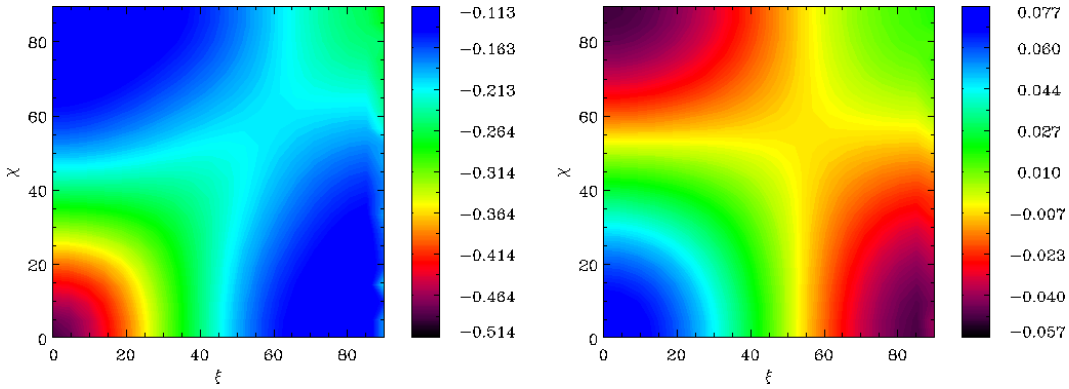

Figure 2.7: Same as in Figure 2.6 but for the fixed ion crustal emission model (González Caniulef et al., 2016).

direction. We remark that both the "intrinsic" and the observed degree of polarisation are evaluated at infinity, and a comparison of the two quantities may be of help in understanding how QED and geometrical effects influence the polarisation observables.

The corresponding contour plots for the condensed surface emission, X–ray and optical phase-averaged polarisation fraction, are shown in Figure 2.6 (free ions) and Figure 2.7 (fixed ions), respectively. In the case of free ions, the phase-averaged polarisation degree in the X–ray band is always less than $\sim 6\%$ either when the emission is dominated by ordinary (negative values) or extraordinary photons (positive values, see Figure 2.6, right panel), while in the optical band (Figure 2.6, left panel) ordinary photons are predominant, with a maximum polarisation degree

$\sim 30\%$ for particular viewing geometries. In the case of fixed ions expectations are similar in the X–ray band, where the phase-averaged polarisation degree is always less than $\sim 8\%$. However, in the optical band, the polarisation degree can be slightly larger, up to $\sim 50\%$ (Figure 2.7, left panel), for the most favorable viewing geometries.

2.7 Predictions for the observed polarisation signal

With the method described in Section § 2.2 and 2.3, it is possible to make a realistic calculation and compute the properties of the radiation as measured by a distant observer for any given viewing configuration, accounting for vacuum birefringence and considering a non-uniform magnetic field topology. In particular, the X-ray pulsed fraction, the phase-averaged[5] degree of polarisation and polarisation angle in the X-ray (0.12 - 0.39 keV) and in the optical bands are computed as functions of the two geometrical angles χ and ξ. Here, all the calculations are performed by assuming that the polarimeter reference frame is aligned with the "fixed" one on the NS. It should be noticed that the choice of the direction of the polarimeter reference frame with respect to the "fixed" reference frame of the NS has no effect on the polarisation fraction, but it affects the polarisation angle (Taverna et al., 2015).

The computed X-ray pulsed fractions are quite similar for both the atmosphere (Figure 2.8, top panel) and condensed surface (Figure 2.9 and 2.10, top panels). Particularly, the 1% X–ray pulsed fraction observed in RX J1856 does not impose a strong constraint on the viewing geometry[6] of the NS (χ and ξ angles). However, it imposes (to a minor extent) a constraint to the polarisation observables. So, for comparison and completeness this information is also kept in the contour plots of phase-averaged polarisation fraction and polarisation angle.

Figure 2.8 shows the results for the case of magnetised atmospheric model.

[5]The polarisation quantities are obtained by averaging the Stokes parameters over the NS rotation.

[6] Using a magnetised model atmosphere, Ho et al. (2007) constrained the viewing geometry of RX J1856 to $< 6^\circ$ for one angle and $\approx 20^\circ - 45^\circ$ for the other. Our ranges for the viewing angles are compatible but less restrictive. The discrepancy may be due to the different choice of mass, radius and temperature which are $M = 1.4 M_\odot$, $R = 14$ km (note that the value of the radius was based on a different distance estimate) and $T_p = 7 \times 10^5$ K (at the magnetic pole) and $T_{eq} = 4 \times 10^5$ K (at the magnetic equator) in Ho et al. (2007).

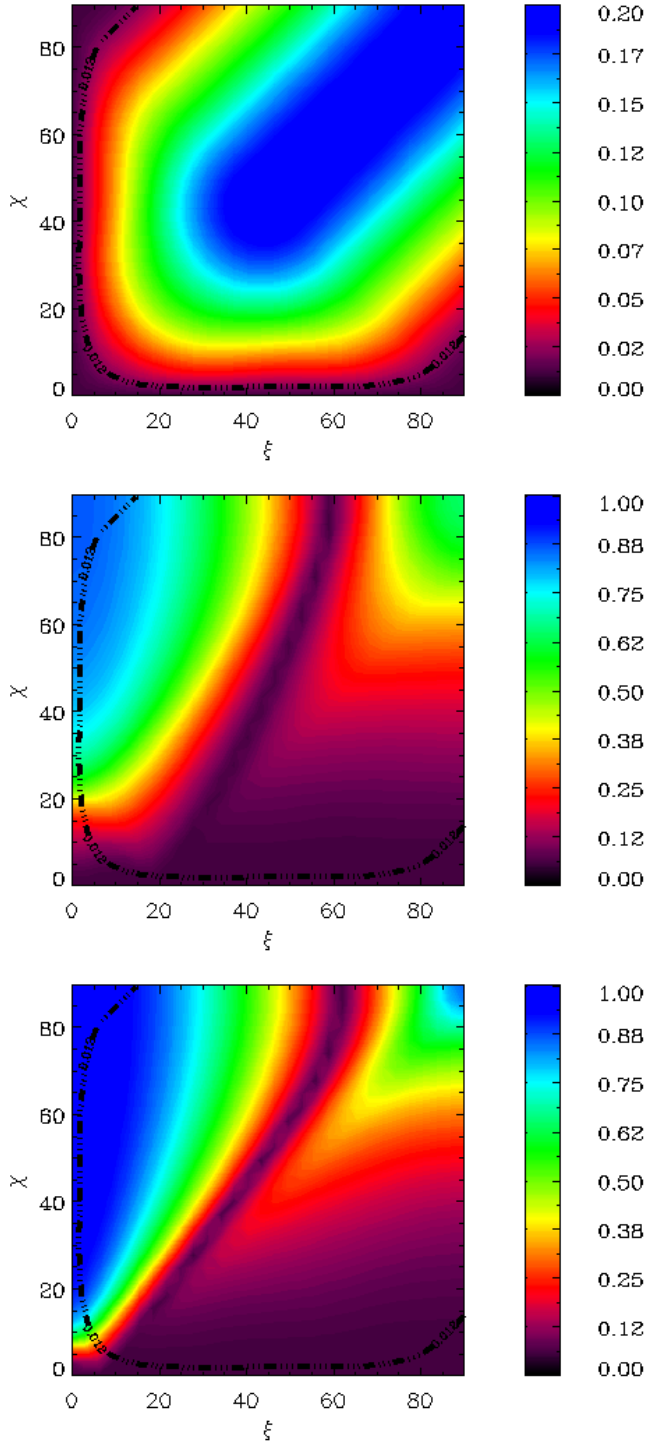

Figure 2.8: Contour plots for the X–ray pulsed fraction, phase-averaged polarisation fraction in the optical (B filter) band and phase-averaged polarisation fraction in the X–ray band (0.12-0.39 keV) in the (χ,ξ) planes (panels from top to bottom respectively) for the gaseous atmosphere model (González Caniulef et al., 2016). All polarisation observables are computed by the expressions of the Stokes parameters. The black curve in each panel corresponds to the observed X–ray pulsed fraction of RX J1856, $\sim 1\%$ (Tiengo and Mereghetti, 2007).

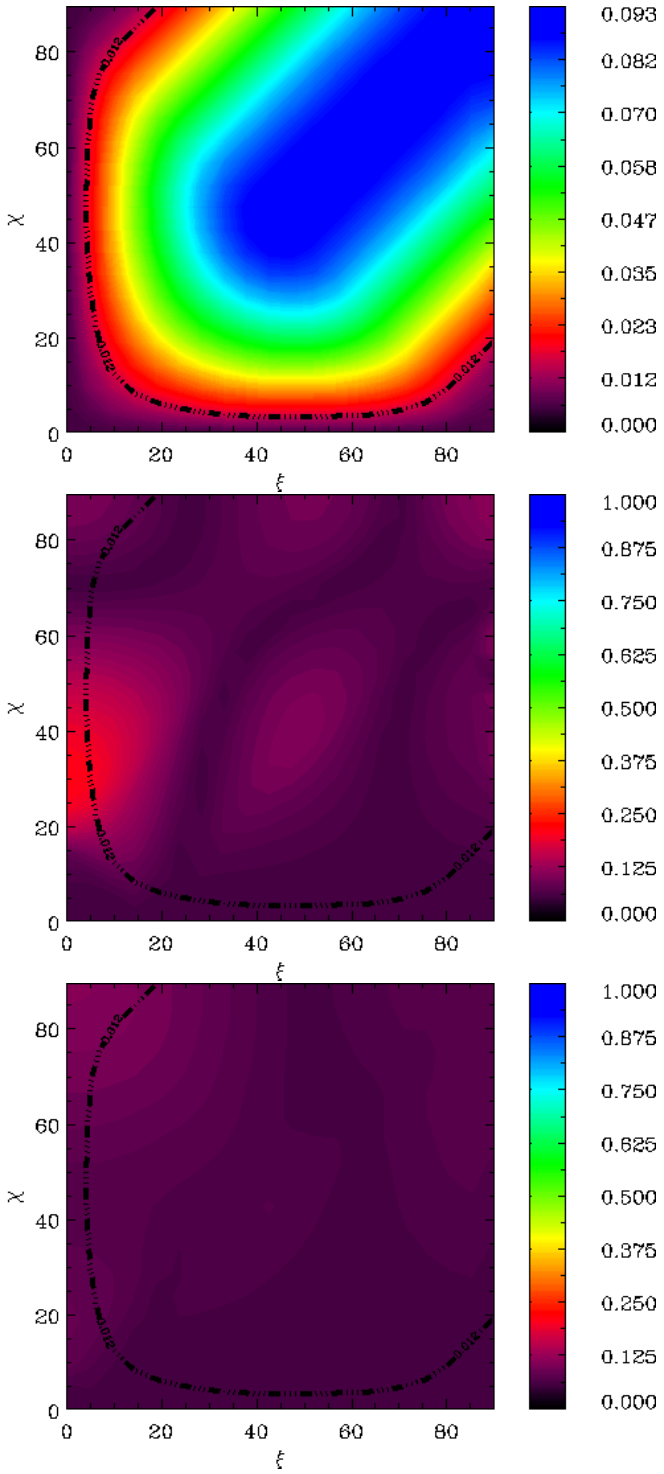

Figure 2.9: Same as Figure 2.8 but for the free ion crustal emission model (González Caniulef et al., 2016).

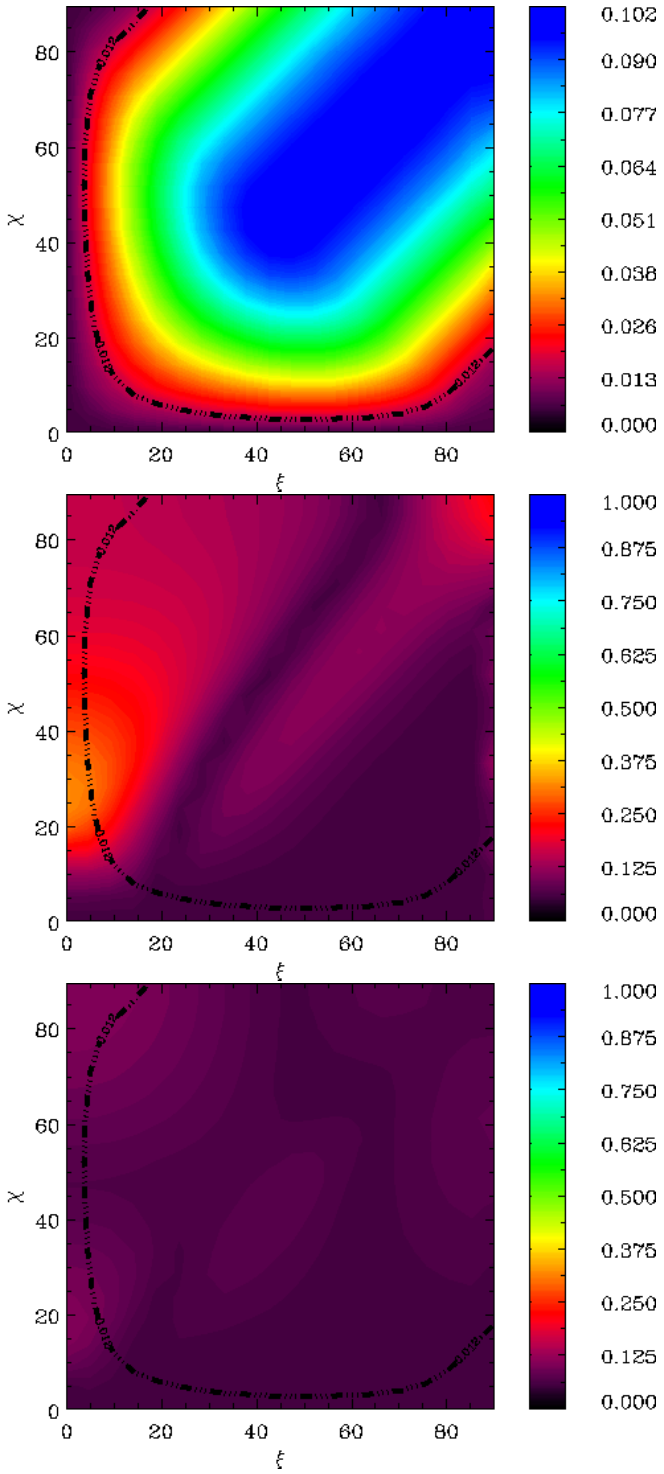

Figure 2.10: Same as Figure 2.8 but for the fixed ion crustal emission model (González Caniulef et al., 2016).

First, the range of viewing angles in which the polarisation fraction is substantial (and potentially detectable) is approximately given by $\chi > \xi$. Viewing geometries near $\chi = 90^\circ$, $\xi = 0^\circ$ or $\chi = 90^\circ$, $\xi = 90^\circ$, which correspond to aligned and orthogonal rotators respectively, both seen perpendicularly to the spin axis, are particularly favorable for observing a high phase-averaged polarisation fraction. In particular, for $\chi = 90^\circ$ and $\xi = 0^\circ$ the phase-averaged polarisation fraction can reach $\sim 80\%$ in the optical band, and be even larger, up to $\sim 90\%$, in the X–ray band.

Figure 2.9 and 2.10 show the case of a condensed surface in the two limits, free and fixed ions, respectively. The results are noticeably different with respect to the atmospheric model. In fact, for free ions, if viewing geometries close to $\chi = 40^\circ$ and $\xi = 0^\circ$ are considered, the phase-averaged polarisation fraction can still be as large as $\sim 20\%$ in the optical band but it is substantially reduced in the X–ray band. In the case of fixed ions, for similar viewing geometries, it is expected a phase-averaged polarisation fraction of $\sim 35\%$ in the optical band while, in the X–ray band, the polarisation is vanishingly small for all viewing angles.

As noticed by Fernández and Davis (2011) and Taverna et al. (2015), the phase-averaged polarisation fraction is expected to be small for $\chi < \xi$, due to a combination of both QED effects and the frame rotation of the Stokes parameters which is needed in presence of a varying magnetic field over the emitting region. The effects of the choice of the emission model become important for viewing angles $\chi > \xi$. In particular, for a magnetised atmosphere, the highest phase-averaged polarisation fraction is attained in the region near $\chi = 90^\circ$ and $\xi = 0^\circ$. This is because: i) under this hypothesis an "intrinsic" polarisation fraction (see Section §2.6.1) as high as $\sim 99\%$ is expected, and ii) in the case of an aligned rotator there is virtually no differential effect due to the rotation of the Stokes parameters at the adiabatic radius (that tends to reduce the observed polarisation degree).

The situation is different for the condensed surface emission. In the optical band, in fact, the "intrinsic" polarisation fraction can be as high as $\sim 30\%$ ($\sim 50\%$) for the case of free (fixed) ions at viewing angles $\chi \sim \xi \sim 0^\circ$ (see Section §2.6.1). However, for this viewing geometry, the depolarising effects of the Stokes parame-

ter rotation are stronger because the α distribution is symmetric and the angles take all the values in the range $[0, 2\pi]$, cancelling the original "intrinsic" polarisation at infinity. As shown in Figures 2.9 and 2.10, central panels, a significant polarisation degree, as high as $\sim 20\%$ ($\sim 35\%$) for the case of free (fixed) ions, is present only for values of $\chi \sim 35^\circ$ and $\xi \sim 0^\circ$. On the other hand, in the X–ray band, ordinary and extraordinary waves are expected to have similar reflected amplitudes: the "intrinsic" polarisation fraction is therefore substantially reduced and as well the observed ones (at all viewing angles).

Figure 2.11 shows the phase-averaged polarisation angle for the atmospheric emission in the optical and X–ray bands. The computed quantity is nearly constant in two regions of viewing angles, for which it is $\chi_P \sim 90^\circ$ and $\chi_P \sim 0^\circ$. This occurs also for the condensed surface models (see Figure 2.12 in the case of fixed ions); however, the main difference is that in these cases the expectation are somehow reversed in the two bands. In fact, by considering the region of viewing angles in which the phase-averaged polarisation fraction is detectable, $\chi \sim 30^\circ$ and $\xi \sim 0^\circ$, it can be noticed that in the case of fixed ions the expected phase-averaged polarisation angle in the optical is $\chi_P \sim 0^\circ$, while the X–ray band this is $\chi_P \sim 90^\circ$.

Again, this behavior can be understood in terms of QED effects. The polarisation angle reflects the global direction of the electric field distribution of the radiation, which in turn depends on the direction of the magnetic field at the adiabatic radius. Then, the observed phase-averaged polarisation angle should reflect the "phase-averaged" direction of the magnetic field at the adiabatic radius, which for viewing angles $\chi > \xi$ is approximately parallel and for $\chi < \xi$ is approximately perpendicular to the spin axis. As a consequence, if the observed radiation is dominated by extraordinary photons, then for $\chi > \xi$ the "average" observed direction of the photon electric field is perpendicular to the spin axis, and the phase-averaged polarisation angle is $\sim 90^\circ$, in agreement with our expectations for the case of the atmosphere model in both, the optical and the X–ray band (Figure 2.11, left and right panel, respectively). Here, it should be noticed that the association between the normal modes and the phase-averaged polarisation fraction is possible because

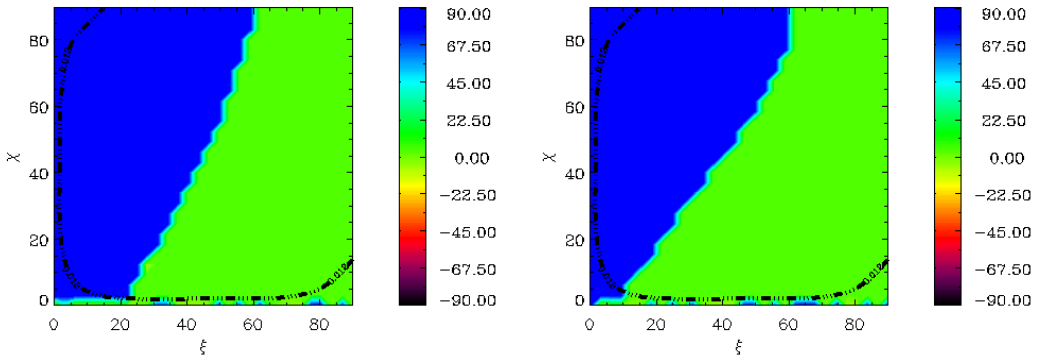

Figure 2.11: Contour plots of the phase-averaged polarisation angles in the (χ, ξ) plane for the gaseous atmosphere emission model, with left and right panels corresponding to the optical (B filter) and the X–ray bands, respectively (González Caniulef et al., 2016).

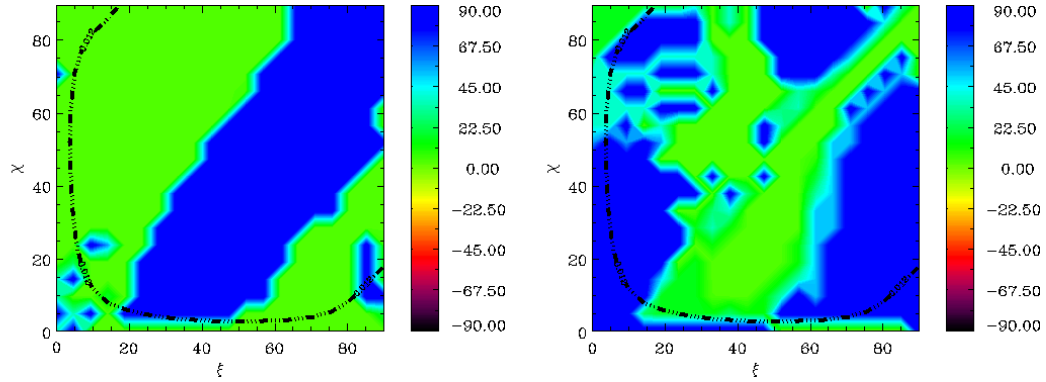

Figure 2.12: Same as Figure 2.11 but for the fixed ion crustal emission model (González Caniulef et al., 2016).

the coordinate system of the polarimeter was set aligned with the "fixed" coordinate system of the NS. However, in general the reference frame of the polarimeter and the "fixed" one of the NS are expected to be disaligned.

For condensed surface emission (in both approximations, fixed and free ions), whereas in the optical band the emitted radiation is dominated by ordinary photons (see Figure 2.7, left panel), in the X–ray band the two modes have similar intensities, with the emitted radiation being slightly dominated by extraordinary photons for fixed ions (Figure 2.7, right panel). As a consequence, in the optical band and for viewing angles $\chi > \xi$ the phase-averaged direction of the photon electric field should be parallel to the spin axis, and thus the phase-averaged polarisation angle is $\sim 0°$. On the contrary, in the X–ray band and again for viewing angles $\chi >$

ξ the phase-averaged direction of the photon electric field is perpendicular to the spin axis, and therefore the expected phase-averaged polarisation angle is $\sim 90^{\circ}$. However, the behavior of the polarisation angle in the X–rays is quite irregular, due to the fact that the emissivities of the two modes in this band are similar to each other. So, the polarisation angle presents jumps by 90°, which arises because of an even slight predominance of O over X photons or conversely. For the same reason, the contour plots in the case of free ions are not shown, since the corresponding polarisation fraction in the two energy bands is even lower than that of the fixed ions case; hence, the phase-averaged polarisation angle behavior for free ions presents even more noisy patterns.

The main conclusion is that, by measuring the phase-averaged polarisation observables in optical *and* X–ray bands it is potentially possible to discriminate between atmospheric and crustal emission. The most favorable geometries are those with viewing angles $\chi > \xi$, for which the expected phase-averaged polarisation fraction is substantial. If emission is atmospheric, it is expected a high phase-averaged polarisation fraction in both, optical and X–ray band (although slightly lower in the optical). Whereas, if emission originates from a condensed surface, the phase-averaged polarisation fraction should be modest in the optical, with an almost unpolarised signal in the X–ray band.

At the same time, the phase-averaged polarisation angle for atmospheric emission is expected to be the same in the optical and X–ray band. On the contrary, for crustal emission the angle measured in the two bands is expected to be different by $\sim 90^{\circ}$ (although this latter consideration is just a theoretical expectation, since realistically the measure of the angle in the X–ray band can not be performed due to low degree of polarisation in the signal).

2.8 Chapter summary and discussion

The polarisation properties of the thermal emission from RX J1856 were studied considering different emission models: a NS with a magnetised atmosphere or a condensed surface. The effects of vacuum polarisation in the propagation of the

radiation in the NS magnetosphere and the rotation of the Stokes parameters were accounted for. Using a ray tracing method and assuming a dipole magnetic field, the polarisation observables were computed for different viewing angles χ and ξ. It was found that the phase-averaged polarisation fraction can be substantial for viewing angles $\chi > \xi$. For these viewing angles, in the case of an atmosphere: **a)** the phase-averaged polarisation fraction in the optical band is expected to be lower than in the X–ray band and **b)** the phase-averaged polarisation angle in the optical is the same that in the X–ray band. In the case of condensed surface, it was found that **a)** the phase-averaged polarisation fraction in the optical band is substantially higher than in the X–ray band and **b)** the phase-averaged polarisation angle in the optical band is generally shifted by 90° with respect to that in the X–ray band. Therefore, by combining optical and X–ray observations of the polarised emission from RX J1856, it is possible to determine if this XDINS has an atmosphere or a condensed surface.

The present treatment of the surface emission from RX J1856 relies on a number of assumptions and simplifications. In particular, the atmosphere model assumes pure H composition and complete ionisation. For the low surface temperature (~ 60 eV) and strong magnetic field ($\sim 10^{13}$ G) of RX J1856, the neutral fraction of H atoms is expected to be ≈ 0.01–0.1 for typical atmospheric densities (Potekhin et al., 2004), so that opacities are affected. H atmospheres with partial ionisation have been presented e.g. by Potekhin and Chabrier (2004) and Suleimanov et al. (2009, see also Potekhin et al. 2014). The major difference with respect to fully ionised models is the appearance of spectral features related to atomic transitions. These features, however, are mainly confined to far UV–soft X–ray range ($\lesssim 0.2$ keV), and fully ionised models give a reasonable description of the spectra at X–ray (above 0.2 keV) and optical energies. Moreover, the features are strongly smeared out when the contributions from different surface patches (each with a different T and $\mathbf{B}$) are summed together to obtain the spectrum at infinity (Ho et al., 2008, see again also Potekhin et al. 2014), similarly to what occurs to the proton cyclotron line (Zane et al., 2001).

As noticed by Pavlov and Shibanov (1979, see also van Adelsberg and Lai 2006; Ho et al. 2003a), in the atmosphere around strongly magnetised NSs, vacuum polarisation can induce a mode collapse point (MCP) where the assumption of two normal mode propagation breaks down. Ho et al. (2003a) interpreted these points as Mikheyev-Smirnov-Wolfenstein like resonances, across which a photon may convert from one mode into the other, with significant changes in the opacities and polarisation. While for $B \lesssim 10^{13}$ G this is not going to change the emission spectrum, it still can significantly affect the polarisation pattern at least at certain energies. For a photon of energy E, the vacuum resonance occurs when the vacuum and plasma contributions to the dielectric tensor become comparable, i.e. where $\rho = \rho_V \approx 0.96 Y_e^{-1} (E/1\ \mathrm{keV})^2 (B/10^{14}\mathrm{G})^2 f^{-2}$ g cm^{-3}, where $Y_\mathrm{e} = Z/A$ (Z and A are the atomic and mass number of the ions) and $f \sim 1$ is a slowly varying function of B. Near the vacuum resonance, the probability of mode conversion is given by $1 - P_\mathrm{jump} = 1 - \exp\left[-\pi \left(E/E_\mathrm{ad}\right)^3/2\right]$, where E_ad depends on the photon energy, on B and on the angle between the photon direction and $\mathbf{B}$ (θ_Bk, van Adelsberg and Lai, 2006, see in particular their eq. 3). For $B \lesssim 10^{13}$ G (as in the case discussed in this work), it is $\rho_\mathrm{V} < 10^{-3}$ g/cm^3, i.e. the vacuum resonance is well outside the photospheres of both the ordinary and the extraordinary mode. Moreover, the inequality $E < E_\mathrm{ad}$ is satisfied for all photon energies $\lesssim 1$ keV, unless radiation is propagating nearly along the magnetic field direction ($\tan\theta_\mathrm{Bk} \lesssim 0.1$). An alternative and more detailed treatment of the photon behavior across the MCP was studied by Pavlov and Shibanov (1979) who demonstrated that the fate of a photon moving across the vacuum resonance (whether it changes or not its polarisation mode) depends on the photon frequency and propagation angle. For this reason our assumption of "no mode conversion" at the vacuum resonance, which is equivalent to assume $E \ll E_\mathrm{ad}$ (or $P_\mathrm{jump} = 1$) for all photons, appears reasonable. Further narrow features due to mode collapse and spin-flip transitions are expected very near the broad proton cyclotron resonance (Ho et al., 2003a; Zane et al., 2000, see also Melrose and Zhelezniakov 1981 for the case of electrons). In the absence of a complete description of the dielectric tensor in a electrons+ions+vacuum plasma, no

mode conversion is assumed as a working hypothesis at this frequency. However, this issue is going to be revisited in the context of atmosphere of magnetars (with magnetic fields $B \sim 10^{14} - 10^{15}$ G), to which the study presented in Chapter §5 is devoted.

The present analysis can be extended to other XDINSs as well. The narrow range of surface temperatures inferred from the spectra of XDINSs, $T \sim 50 - 100$ eV may be important to determine the state of the surface, but it should not have an important effect on the properties of the observable polarisation. A significant difference on the polarisation properties of XDINSs may be introduced if different magnetic field configurations are considered (Taverna et al., 2015). However, in general, XDINSs share a similar magnetic field configuration, i.e., external dipole magnetic field, and there is no observational evidence for multipolar components or twisted magnetic fields (such as those that may be present in magnetars, see Turolla et al. 2015). This is supported by the good agreement between the magnetic fields derived from timing properties and those inferred from the absorption lines (assuming that they are caused by proton cyclotron resonance or atomic transitions in the strong magnetic field, see Turolla 2009), and by the absence of non-thermal emission that may be linked to the presence of a twist in the external magnetic field. However, in this respect RX J0720.4-3125 may be an exception. For this XDINS, an absorption feature that is energy-dependent and phase-dependent has been reported (Borghese et al., 2015). If this feature is caused by proton cyclotron resonance, then it would be compatible with the presence of a multipolar component confined very close to the NS surface and consistent with a magnetic field $B = 10^{14}$ G. The effect of this component on the polarisation properties of the radiation has not been assessed in my study so far, but certainly it can be studied in the future using the method and the emission models discussed in this chapter.

Chapter 3

Optical polarimetry of RX J1856.5−3754

The models of RX J1856 presented in Chapter §2 shown that combined optical and X-ray polarimetric observations of XDINSs can allow us to distinguish between the emission from a magnetised atmosphere or a condensed surface. However, the models assume an important ingredient: the propagation of the radiation from the XDINSs is affected by QED vacuum birefringence, an effect that was predicted more than 80 years ago by Heisenberg and Euler (1936) and Weisskopf (1936) but has not been observed in terrestrial laboratories, yet. Motivated by the exciting possibility to use XDINSs to test this QED effect for the first time, I collaborated with a team of experts in optical observations of NSs (PI: R. Mignani) and proposed to performed optical polarimetric observations of RX J1856 with the VLT (Very Large Telescope, at the ESO Cerro Paranal Observatory, Chile). The proposal was accepted and time was allocated to observe this source in May-June 2015: this was the first polarimetric measurement ever done for a XDINS. In this chapter, the theoretical models developed in Chapter §2 are confronted with the polarimetric observation of RX J1856. I discuss a potential signal of QED vacuum birefringence found[1] in RX J1856 and further astrophysical constraints obtained from this optical polarimetric observation.

[1] A press coverage by ESO can be found in https://www.eso.org/public/news/eso1641/

3.1 Introduction

One of the first predictions of QED, even before it was properly formulated, was vacuum birefringence, and, in particular, that a strong magnetic field affects the propagation of light through it (Heisenberg and Euler, 1936; Weisskopf, 1936). Despite the signal of QED vacuum birefringence has been searched for by a number of experiments (in terrestrial laboratories), such as PVLAS[2] (in Italy), OSQAR[3] (at CERN, Switzerland), BMV[4] (in France), Q&A[5] (in Taiwan), and BFRT[6] (in USA), no positive detection has been reported, yet.

As discussed in Chapter §2, the thermal emission from XDINSs comes from a region comparable with the entire star surface, over which the magnetic field direction changes substantially. In the absence of QED vacuum polarisation effects, this would produce a drastic depolarisation of the radiation collected at infinity (Heyl et al., 2003, see also Taverna et al. 2015; González Caniulef et al. 2016 and references therein). Vacuum birefringence dramatically increases the linear polarisation of the observed radiation, from a level of a few % up to even $\sim 100\%$, depending on the viewing geometry and the surface emission mechanism (Heyl and Shaviv, 2000, 2002; Heyl et al., 2003; Taverna et al., 2015; González Caniulef et al., 2016). Detecting polarisation in the thermal emission from the surface of XDINSs is therefore extremely valuable. First, and independently on the physical conditions of the emitting region, the detection of a large degree of linear polarisation in the signal would constitute the observational evidence of QED vacuum polarisation effects in the strong-field regime. Second, the polarisation observables can be compared with emission models and help uncover the physical conditions of the surface of XDINSs, ideally complementing spectral observations. Furthermore, polarimetric observations combined with measurements of the X-ray pulsed fraction can helps us to constraint the viewing geometry of the source.

With X-ray polarimetry still moving its first steps (see e.g., Marshall et al.,

[2] http://pvlas.ts.infn.it
[3] https://home.cern/about/experiments/osqar
[4] http://www.toulouse.lncmi.cnrs.fr/spip.php?rubrique78&lang=en
[5] Chen et al. (2007)
[6] Cameron et al. (1993)

2015), other energy ranges must be explored. Besides the X-rays, all XDINSs have been detected in the optical/near-UV (Kaplan et al., 2011b) where well-tested techniques, even for objects as faint as INSs, can be exploited, as shown by the polarisation measurements in RPPs (see e.g., Mignani et al., 2015). Due to their faintness, prior this work no optical polarimetric observations have been performed for any XDINSs. In particular, RX J1856 is the brightest ($V \sim 25.5$; Walter and Matthews, 1997) and youngest (0.42 Myr; Mignani et al., 2013) of this class of NSs. This source is located at a relatively close distance, 123^{+11}_{-15} pc (Walter et al., 2010), which minimises the effects of contamination by foreground polarisation. In the next section, I present a summary of the optical polarimetric observation of RX J1856 carried out with the VLT, in Chile (further details can be found in Mignani et al. 2017).

3.2 Observation description

The VLT optical polarimetric observations of RX J1856 were performed in May and June 2015 (PI: R. Mignani). In particular, one of the VLT tescopes (the Antu telescope) mounts the FORS2 (the second Focal Reducer and low dispersion Spectrograph, Appenzeller et al. 1998). This instrument can operate in different modes: imaging, polarimetry, long slit and multi-object spectroscopy (MOS). The polarimetry mode works with a Wollaston prism as a beam splitting analyser and two superachromatic phase retarder 3x3 plate mosaics. In imaging polarimetry (IPOL) of extended sources or crowded fields a strip mask is inserted in the focal area of FORS2 to avoid overlapping of the two beams of polarised light in the CCD. This mask is obtained by setting the MOS slits in such a way that images corresponding to the extraordinary and ordinary beams are recorded on two adjacent slits.

Images were obtained with the high efficiency v_{HIGH} filter ($\lambda = 555.0$ nm, $\Delta\lambda = 61.6$ nm). To measure the linear polarisation, the four standard IPOL half-wave retarder plate angles of 0°, 22.°5, 45°, and 67.°5, were used. In order to deal with the variable sky polarisation background, each observation block (OB) incorporated exposures ($\sim$ 720 s) for each of the four retarder plate angles. A total of

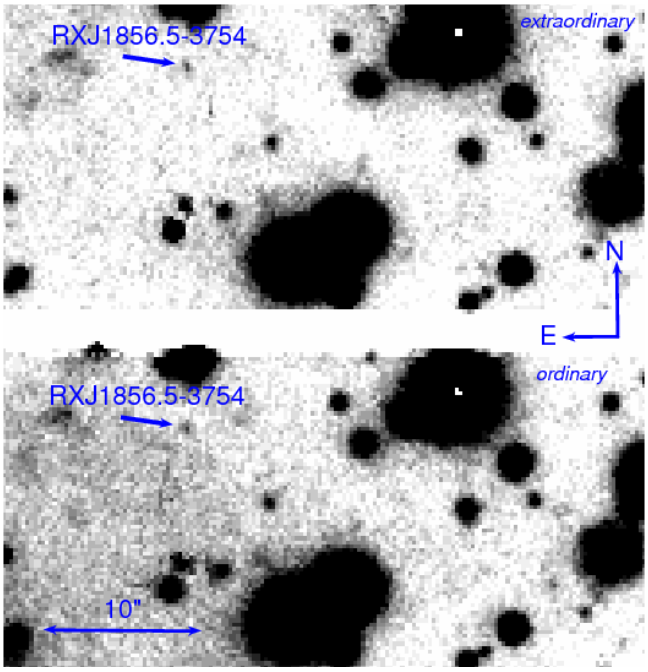

Figure 3.1: Section of the FORS2 IPOL v_{HIGH}-band image of the RX J1856 field obtained from the co-addition of all exposures taken with all retarder plate angles. The optical counterpart to RX J1856 is marked by the arrow and labelled. The image is divided in two parts, corresponding to two adjacent MOS slitlets in the FORS2 polarisation optics, which split the incoming light into two beams. The top and bottom part of the image corresponds to the extraordinary and ordinary beams, respectively, whereas the white stripe corresponds to the gap between the two adjacent MOS slitlets (Mignani et al., 2017).

11 OBs were executed, for a total exposure of 7920 s per angle. Observations were performed in dark time, with average seeing of $0\farcs84$, airmass below 1.1, and clear sky conditions (Mignani et al., 2017). In addition, a number of short exposures (< 3 s) of polarised standard stars (Mathewson and Ford, 1971; Whittet et al., 1992) were acquired for calibration purposes, as part of the FORS2 calibration plan.

The Guide Star Catalogue 2 (GSC-2; Lasker et al., 2008) was used as a reference for Astrometry calculations. The RX J1856 position at the epoch of the FORS2 observations (2015.37) was obtained by correcting for its proper motion μ using its reference coordinates (epoch 1999.7) measured with the *Hubble Space Telescope* (Kaplan et al., 2002). The derived coordinates at the epoch of the VLT observations are $\alpha = 18^{\rm h}56^{\rm m}36\fs03$; $\delta = -37^\circ5437\farcs11$ (J2000), which were used to identify the source in the images (Mignani et al., 2017).

The processing of the images, photometry and model for PSF were done with IRAF software (see Mignani et al. 2017 for details). Figure 3.1 shows a section of the image obtained from the co-addition of all exposures taken with all retarder plate angles, zoomed on the RX J1856 position.

Following the FORS2 manual[7], the degree of linear polarisation of a source is calculated from the normalised Stokes parameters $P_{\rm U} \equiv U/I$ and $P_{\rm Q} \equiv Q/I$:

$$P_{\rm Q} = \frac{1}{2}\left\{\left(\frac{f^{\rm o}-f^{\rm e}}{f^{\rm o}+f^{\rm e}}\right)_{\alpha=0^\circ} - \left(\frac{f^{\rm o}-f^{\rm e}}{f^{\rm o}+f^{\rm e}}\right)_{\alpha=45^\circ}\right\} \tag{3.1}$$

$$P_{\rm U} = \frac{1}{2}\left\{\left(\frac{f^{\rm o}-f^{\rm e}}{f^{\rm o}+f^{\rm e}}\right)_{\alpha=22.5^\circ} - \left(\frac{f^{\rm o}-f^{\rm e}}{f^{\rm o}+f^{\rm e}}\right)_{\alpha=67.5^\circ}\right\} \tag{3.2}$$

where $f^{\rm o}$ and $f^{\rm e}$ are the source fluxes in the ordinary (o) and extraordinary (e) beams, respectively, for each of the four retarder plate angles α (0°, 22.°5, 45° and 67.°5). The linear polarisation degree (PD) and position angle (PA) are, then, determined from $P_{\rm U}$ and $P_{\rm Q}$ according the usual definitions:

$$\mathrm{PD} = \sqrt{{P_{\rm Q}}^2 + {P_{\rm U}}^2} \tag{3.3}$$

$$\mathrm{PA} = \frac{1}{2}\arctan\left(\frac{P_{\rm U}}{P_{\rm Q}}\right). \tag{3.4}$$

3.3 Results

3.3.1 RX J1856 polarisation

The polarisation quantities for RX J1856 obtained after the data reduction and photometric analysis are PD $= 16.43\% \pm 5.26\%$ and PA $= 145.^\circ39 \pm 9.^\circ44$. The errors are at one sigma level (computed as described in Fossati et al. 2007) and reflect uncertainties dominated by statistics as the target is faint.

Remarkably, the polarisation degree measured for RX J1856 seems to be above what measured for RPPs[8] (see Chapter §1), for which the PD is usually below 10%

[7] The FORS2 User Manual (Boffin, 2014)

[8] The Crab and Vela pulsars, PSR B0540−69, PSR B1509−58, and PSR B0656+14 (see,

(Mignani et al. 2015). The orientation of the polarisation angle is also different. Previous optical and/or radio polarisation measurements in RPPs showed a substantial alignment between the polarisation angle and the proper motion direction (Mignani et al., 2015, and references therein), which can give us some insights about, for instance, the kick mechanism in the proto NSs (Section §3.4.3 and references therein). In the case of RX J1856, the measured polarisation angle PA $= 145.^{\circ}39 \pm 9.^{\circ}44$ and the proper motion (PA$^{\mu} = 100.^{\circ}2 \pm 0.^{\circ}2$; Kaplan et al. 2002) differ significantly, by $\sim 45^{\circ}$, even accounting for the substantial uncertainty of the former measurement.

It should be noted, however, that the emission process which produces the polarised optical radiation is different for RPPs and thermally emitting XDINSs. In young RPPs, such as the Crab and Vela pulsars, the optical emission is produced in the NS magnetosphere (Pacini & Salvati 1983), i.e. along a preferred direction, whereas in thermally emitting XDINSs the optical radiation comes from the entire cooling NS surface. In fact, this may be a potential explanation for the misalignment between the proper motion of RX J1856 and its PA. However, the polarisation properties of the thermal emission from XDINSs depend on the topology of their magnetic field. As discussed in Chapter §2, if the magnetic topology is dominated by a dipolar component, then, the measurement of PA may give us information about the rotational axis of the source. Furthermore, as also discussed in Chapter §2, combined polarimetric observation with the X-ray pulsed fraction of XDINSs may allow us to constraint the geometry of the sources i.e., the angles associated to the LOS and magnetic axis with respect to the spin axis. This information, in turn, may allow us to extend to XDINSs the analysis of the proper motion and PA done for RPPs. Before proceeding in this analysis, it is important to rule out sources of contamination in the optical polarimetric observation, which is done in the next section.

Mignani et al. 2015 and references therein)

3.3.2 Remarks on the possibility of polarisation contamination

RX J1856 is $\sim 1.^{\circ}4$ away from the center of the dusty molecular cloud complex in the Corona Australis region (CrA). The distance to the CrA complex is not clear and it may vary from $\sim$ 130 pc (Casey et al. 1998) to $\sim$ 170 pc (Knude & Høg, 1998). Therefore, a CrA dark cloud (either in foreground or which embeds the source) may affect the polarisation measurement of RX J1856 which is a distance of $\sim$ 120 pc (Walter et al., 2010). Although the properties of dust in the interstellar medium are not very well understood, its effects are known: a net degree of polarisation may be observed, due to starlight scattering onto the dust grains, for an intrinsically unpolarised source. In fact, this has been observed in stars embedded in, or in the background of, dust clouds, showing a non-zero degree of polarisation (e.g. Draine, 2004, for a review). The dust-induced degree of linear polarisation $p(\lambda)$ can be described by the empirical Serkowski's law (Serkowski, 1973):

$$p(\lambda) = p_{\max} \exp[-K \ln^2(\lambda/\lambda_{\max})], \tag{3.5}$$

where λ is the radiation wavelength and $p_{\max}$ is the maximum polarisation at $\lambda_{\max}$. In general K linearly depends on $\lambda_{\max}$ (e.g. Wilking et al., 1982; Whittet et al., 1992; Cikota et al., 2017), while the maximum polarisation $p_{\max}$ is found to be a function of the reddening (Serkowski, 1973, and references therein), $p_{\max} \sim 0.09E(B-V)$. Since $\lambda_{\max} \sim 555$ nm (Serkowski et al., 1975), which is within the v_{HIGH} filter range, the effects of dust in the polarisation measurement could be potentially relevant. The measured interstellar extinction towards RX J1856 is $A_V \sim 0.12$ (van Kerkwijk and Kulkarni, 2001a) which translates into $E(B-V) \sim 0.04$. Therefore, assuming that the CrA complex is, indeed, foreground to RX J1856, the maximum degree of polarisation predicted by the Serkowski's law in the v_{HIGH} filter ($\lambda \simeq \lambda_{\max}$) would be $p_{\max} \sim 0.36\%$, almost undetectable for this source. It should be noticed that the polarisation is affected by the degree of alignment of the dust grains i.e. on how much their spin angular momenta point in the same direction (a still very debated issue; see e.g. Draine, 2004). To account for this, a relatively large value of $p_{\max}$ has been already chosen in the previous calculations, showing that even a large degree

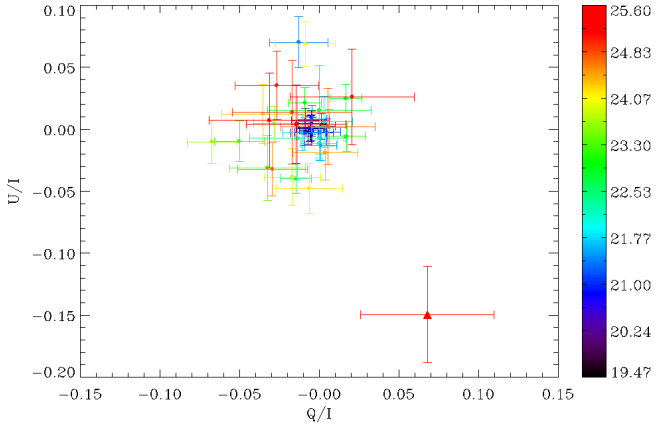

Figure 3.2: Plot of the normalised Stokes parameters U/I and Q/I for a selected sample of 42 field stars (filled points; top left) and for RX J1856 (filled triangle, bottom right). Notice that the values of U/I and Q/I plotted here are in unity fractions and so would be the value of PD computed from them (Eqn. 3.3). The color bar on the right corresponds to the stars V-band magnitude (Mignani et al., 2017).

of dust alignment is not able to produce a polarisation degree higher than 1%.

Furthermore, this conclusion is confirmed by the values of the Stokes parameters $P_{\rm Q}$ and $P_{\rm U}$ measured for a set of 42 stars randomly selected within a region of a few arcmin in the RX J1856 field, as shown in Figure 3.2. For these field stars (selected in the magnitude range ∼20–26, away from the CCD edges and with error lower than 5%) the intrinsic degree of polarisation is very small or even statistically compatible with zero. This show that dust effects are quite unimportant and are not able to explain the substantial degree of polarisation measured for RX J1856 ($\gtrsim$ 11%).

An extra possible source of polarisation contamination could be the bow-shock nebula of RX J1856. This nebula is observed in H_α images, with the apex being $\sim$ 1 arcsec ahead of the NS, and the tail extending up to $\sim$ 25 arcsec behind it (van Kerkwijk and Kulkarni, 2001a). The free electrons in the shocked interstellar medium (ISM) may also modify the polarisation signal from this source. However, the estimated number density (3 cm^{-3}) in the shocked ISM surrounding RX J1856 (van Kerkwijk and Kulkarni, 2001a) is too small to make propagation effects such as scattering or Faraday conversion relevant in this context.

3.4 Discussion

3.4.1 Comparison with theoretical models

I have used the theoretical framework described in Chapter §2 to compute the polarisation properties of RX J1856 in the optical v_{HIGH} band ($\lambda = 555.0$ nm, $\Delta\lambda = 61.6$ nm), in which the data were collected. The models account for QED vacuum birefringence and consider the case of thermal emission from (i) a magnetised, completely ionised hydrogen atmosphere, and (ii) a condensed surface (both in the fixed and free ion limit; see again Chapter §2). Results are summarised in Figure 3.3 (see also Table 3.1), which shows the observed PD as a function of χ (spin - LOS) and ξ (spin - B axis) angles.

Figure 3.3 (left panel) shows the case of atmospheric emission, for which there is a range of angles that is consistent with both the X-ray pulsed fraction (1.2 %, Tiengo and Mereghetti, 2007), and the observed PD, $16.43\% \pm 5.26\%$: the angle between the LOS and the spin axis is constrained to $\chi = 14.^{\circ}0^{+2.3}_{-3.0}$ and the angle between the magnetic axis and the spin axis is constrained to $\xi = 3.^{\circ}1^{+0.8}_{-0.4}$. Figure 3.3 (right panel) shows the case of condensed surface models, for which the optical polarimetric measurement and the X-ray pulsed fraction are consistent only in the fixed ion limit. Here, the viewing geometry is constrained for two pairs of angles: $\chi = 21.^{\circ}7^{+5.9}_{-4.4}$ and $\xi = 5.^{\circ}5^{+1.4}_{-1.3}$, together with $\chi = 51.^{\circ}9^{+37.3}_{-14.7}$ and $\xi = 2.^{\circ}9^{+13.2}_{-0.4}$, while the central value of the measured PD is never recovered in the free ion case.

For all the considered emission models, the analysis shows relatively small values of ξ, and $\chi \sim 15^{\circ}$–20° (in the case of the condensed surface emission model and the fixed ions limit there is a second solution at $\chi \sim 50^{\circ}$). This narrows the (broader) constraints set on the two geometrical angles by Ho (2007), $\chi \approx 20^{\circ}$–45° and $\xi \lesssim 6^{\circ}$ (or vice versa), on the basis of their pulse profile fits with atmospheric models. With the present estimate of the geometrical angles, a putative radio beam from RX J1856 would not intersect the LOS, either assuming the pulsars average beaming factor, $f = 0.1$, or using the expression by Tauris and Manchester (1998) to relate f to the spin period (see also Ho, 2007). This may be a plausible explanation for the undetected radio emission from RX J1856 (see Chapter §1 for the

Table 3.1: Constraints on the viewing angles for RX J1856.

Model	$\chi(^\circ)$	$\xi(^\circ)$	Reference
Optical polarimetry plus X-ray pulsed fraction			
Atmosphere	$14.0^{+2.3}_{-3.0}$	$3.1^{+0.8}_{-0.4}$	This work
Condensed surface †	$21.7^{+5.9}_{-4.4}$	$5.5^{+1.4}_{-1.3}$	This work
	$51.9^{+37.3}_{-14.7}$	$2.9^{+13.2}_{-0.4}$	This work
X-ray light curve			
Atmosphere	≈ 20–45	$\lesssim 6$	Ho (2007)

† Fixed ion limit.

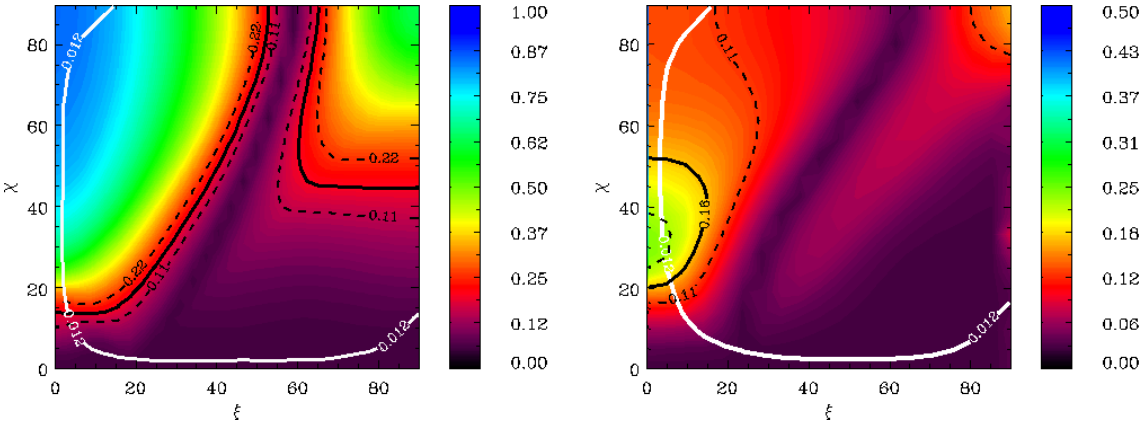

Figure 3.3: Contour plot of the phase-averaged linear polarisation degree in the VLT v_{HIGH} band for the atmosphere (left) and the condensed surface in the fixed ion limit (right) models. Notice the different scale in each color bar. The thick white line shows the domain of ξ–χ angles in which the computed pulsed fraction matches the observed value, 1.2% (Tiengo and Mereghetti, 2007). The solid black line corresponds to the measured VLT optical polarisation of RX J1856 while the dashed lines correspond to the $\pm 1\sigma$ error (PD $= 16.43 \pm 5.26\%$). (Mignani et al., 2017)

properties of XDINSs), and it may also provide an interesting scientific case for further polarimetric observations of other XDINSs and studying the lack of radio emission in these sources.

3.4.2 Test of QED predictions

Polarimetric observations in a single band are not sufficient to disentangle the emission model from the surface of an XDINS (gaseous atmosphere or condensed sur-

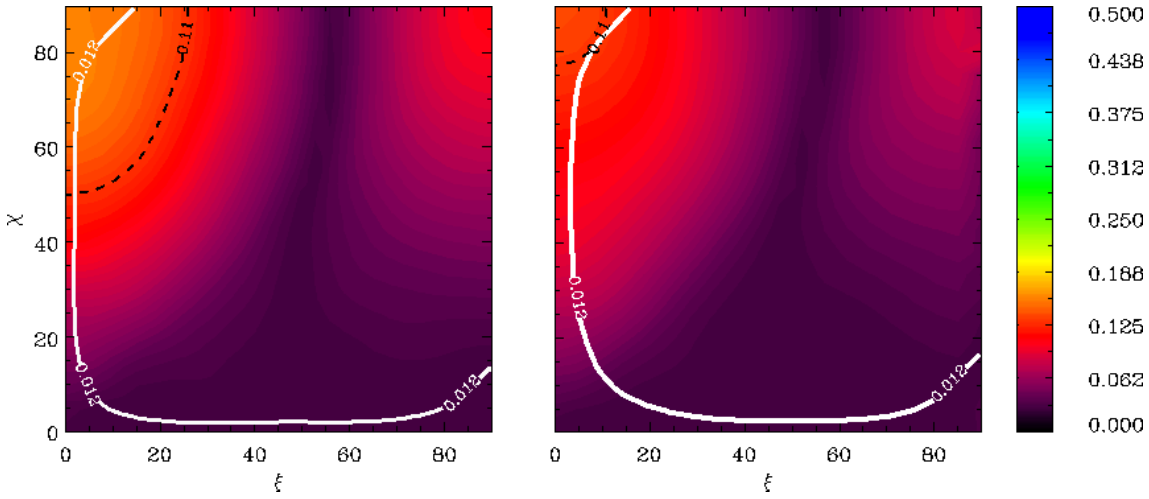

Figure 3.4: Same as in Figure 3.3 for emission from an atmosphere (left) and condensed surface in fixed ion limit (right) but without accounting for vacuum polarisation effects. Notice scale in color bar (Mignani et al., 2017).

face, see Chapter §2). However, even a single band measurement offers an unique and unprecedented opportunity to experimentally test the predictions of QED vacuum polarisation effects in the strong field limit (Chapter §2). In order to do this, I recomputed the models for the polarisation fraction PD in the optical band for RX J1856, this time neglecting vacuum polarisation effects. Results are shown in Figure 3.4. In all cases, the computed phase-averaged PD is substantially reduced compared to the case without QED effects. This is because, now, the depolarisation induced by the frame rotation is much more effective at the star surface due to the non-uniform topology of the magnetic field (Heyl and Shaviv, 2002; van Adelsberg and Lai, 2006; Taverna et al., 2015; González Caniulef et al., 2016). The minimum observed phase-averaged PD (at 1σ level) is still within the polarisation range for the atmospheric emission and condensed surface emission in the fixed ions limit (while it is not for the condensed surface model in the free ion limit). However, the most likely measured value is never reproduced by models with no QED vacuum polarisation effects and the highest attainable PD, which is anyway below the measurement, requires a very particular geometry of the source, i.e. an aligned rotator ($\xi \approx 0°$), seen equator-on ($\chi \approx 90°$). Furthermore, at variance with the case where vacuum birefringence is accounted for, if the models do not include QED effects, the constraints on the viewing geometry differ substantially from those obtained by

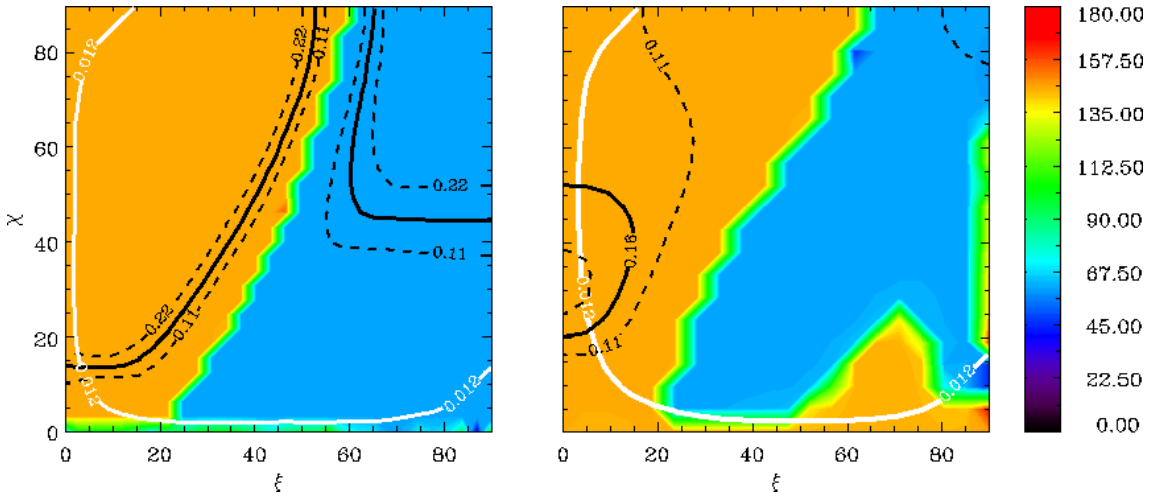

Figure 3.5: Contour plot of the phase-averaged position angle in the VLT v_{HIGH} band for emission from a gaseous atmosphere (left) and a condensed surface (fixed ion limit; right). In each case a rotation by an angle β around the LOS has been applied (see Sectn. 3.4.3 for details). The labeled contours have the same meaning as in Figure 3.3 (Mignani et al., 2017).

.

Ho (2007), based on the study of the X-ray light curve of RX J1856. The observed high value of the PD is therefore a strong indicator for the presence of vacuum polarisation effects around RX J1856.

3.4.3 Constraints on neutron star viewing orientations

In principle, the polarisation position angle PA provides independent information about the viewing orientations of the NS. However, care must be taken in comparing the observed value with those derived from simulations since the PA depends on the choice of a reference direction in the plane of the sky. More specifically, the polarisation properties computed in Chapter §2 were obtained by assuming as reference direction the projection of the star spin axis on the plane of the sky. In the case of the atmospheric emission model, it was found that the phase-averaged PA is nearly constant over almost the entire region where $\chi > \xi$ and assumes a value of $\sim 90°$. This implies that, when "phase-averaging" the signal, the direction of the electric field of the observed radiation should oscillate mostly in a direction perpendicular to the star spin axis projected on the sky (with the thermal radiation dominated by X-mode photons). For the condensed emission model (considering

only the fixed ion limit since it matches the PD constraint), the situation is similar but somehow reversed, with PA $\sim 0^\circ$ in the region where $\chi > \xi$, meaning that the electric field oscillates mainly along the projection of the spin axis (with the thermal radiation dominated by O-mode photons).

The VLT polarimetry observations of RX J1856 give a polarisation position angle PA $= 145.^\circ39 \pm 9.^\circ44$, where this angle is computed using as reference direction the North Celestial Meridian. Thus, it is necessary to introduce a rotation by an angle β around the LOS, to account for the different reference direction in the simulations and in the observations. In this case, β corresponds to the angle between the projection of the NS spin axis on the plane of the sky and the North Celestial Meridian. By doing this, it is possible to obtain for the first time the absolute direction of the spin-axis of RX J1856 in the plane of the sky. It was found that, for the atmosphere model, a rotation angle $\beta = 55.^\circ39 \pm 9.^\circ44$ (or $235.^\circ39 \pm 9.^\circ44$) reproduces the observed value, for the viewing angles derived in Section 3.4.1 ($\chi = 14.^\circ0^{+2.3}_{-3.0}$, $\xi = 3.^\circ1^{+0.8}_{-0.4}$). Similarly, a rotation angle $\beta = 145.^\circ39 \pm 9.^\circ44$ (or $325.^\circ39 \pm 9.^\circ44$) is required for the condensed surface model (fixed ions, see Figure 3.5).

From the value of β, I can also compute the angle θ between the projection of the NS spin axis on the plane of the sky and the NS proper motion vector, which can be obtained from $\theta = \mathrm{PA}^\mu - \beta$, where $\mathrm{PA}^\mu = 100.^\circ2 \pm 0.^\circ2$ (Kaplan et al., 2002) is the angle associated to the proper motion μ of the source. For the atmospheric case ($\beta = 55.^\circ39 \pm 9.^\circ44$), it is found that the direction of the spin-axis of RX J1856 is tilted westward of the NS proper motion vector by an angle $\theta = 44.^\circ81 \pm 9.^\circ64$. In the case of the condensed surface emission model ($\beta = 145.^\circ39 \pm 9.^\circ44$), instead, the projection of the spin axis is tilted eastward of the proper motion vector by $\theta = 45.^\circ19 \pm 9.^\circ64$. Therefore, in both cases the projection of the spin axis and the proper motion vector are significantly misaligned.

Although this is still a debated issue, it has been suggested that in the Crab and Vela pulsars the direction of the spin axis projected in the plane of the sky, assumed to coincide with the axis of symmetry of their X-ray pulsar wind nebulae (PWNe), coincides with that of the proper motion (Helfand et al., 2001; Pavlov

et al., 2001, see also Kaplan et al. 2008). Noutsos et al. (2012) presented a statistical analysis based on a large sample of pulsars with proper motion and polarisation measurement, and found evidence for pulsar spin-velocity alignment, although the possibility of orthogonal spin-velocity configurations could not be excluded. Such an alignment derives from that of the pulsar rotation axis and the velocity vector. The latter can be produced if the proto-NS kick resulted from multiple thrusts over a time longer than the star initial period. On the other hand, no correlation is expected if the acceleration phase is shorter (Spruit and Phinney, 1998). Therefore, the $\sim 45^\circ$ misalignment that we found in RX J1856 might not be peculiar, also accounting for the fact that the velocity vector might have changed over the source lifetime, ~ 0.42 Myr, as the result of the interaction with the Galactic gravitational potential (e.g., Mignani et al. 2013). For comparison, in the case of the radio-quiet RPP Geminga, of age (≈ 0.3 Myr) comparable to RX J1856, the pulsar spin axis (again assumed to coincide with the axis of symmetry of its PWN) and the proper motion vector are aligned (Pavlov et al. 2010). This would suggest that their relative orientation has not been affected by the pulsar orbit in the Galactic potential (Pellizza et al. 2005).

3.5 X-ray polarimetry prediction

The state of the matter in the surface of XDINSs can be determined by using combined optical and X-ray polarimetry, as discussed in Chapter §2. The optical VLT polarimetric observation of RX J1856 provides constraints on its viewing geometry. This, in turn, allows us to make sensible predictions for future X-ray polarimetry missions (under study) capable to observe this source and other XDINSs (see e.g. Marshall et al., 2015).

Based on the X-ray polarisation in the energy band $E = 0.1 - 0.4$ keV (computed in Chapter §2, accounting for QED vacuum birefringence), it is possible to argue that if an atmosphere is present in RX J1856, the PD in the soft X-ray band is expected to be in the range 62-86%, which is substantially higher than the PD in the optical band. However, if a condensed surface is present (in the fixed ion limit) the corresponding X-ray PD will be $\lesssim 6\%$, much lower than that in the optical band.

Also, as shown in Chapter §2, the polarisation angle PA in the optical and X-ray band are expected to be the same in the case of atmospheric emission but they have a relative shift of a 90° in the condensed surface model. Therefore, if an atmosphere is present in the surface of RX J1856 the PA in the X-ray band is expected to be approximately 145°. On the contrary, if a condensed surface is present, the expected PA in the X-ray band will be roughly 55° deg (in the fixed ion limit).

For completeness, I can also use my models to compute the X-ray polarimetry expectations, without to account for vacuum polarisation effects. For atmospheric emission, and the viewing angles derived from the optical observation, the expected PD is $\sim 1-7\%$. It should be noticed that this value is lower than that measured in the optical band, $\sim 11-21\%$. This is explained by the magnetic and temperature distribution used in the simulations, i.e., a NS with a dipole field and temperature distribution hotter at the magnetic poles and colder at the magnetic equator. In particular, the X-ray emission is produced mostly in the NS poles, where the depolarisation effects by the magnetic field topology are stronger. Instead, the optical emission is produced by the extended area around the equator, where the depolarisation effects by the magnetic field topology are lower, which explain the higher PD in this band when vacuum polarisation is not operating. Finally, in the case of the condensed surface (fixed ion), the expected PD in the X-ray band is $\sim 2\%$, nearly undetectable.

3.6 Chapter summary and conclusions

In this chapter I have presented the first measurement of optical polarisation from an XDINS, RX J1856. The observations show a linear polarisation degree PD = $16.43\% \pm 5.26\%$ and a polarisation position angle PA = $145.^{\circ}39 \pm 9.^{\circ}44$. At variance with the case of RPPs, in which polarisation measurements give an indication of the magnetic field direction in the magnetosphere (Mignani et al. 2015 and references therein), in the case at hand the polarisation observables are directly linked to the properties of the surface (or atmospheric) layers of the NS. As already discussed in Chapter §2, combined optical and X–ray polarimetry can be used to discriminate between the emission from a gaseous atmosphere or a condensed surface. Thus, this optical measurement paves the way to future X-ray polarimetry measurements in the soft X rays (e.g., Marshall et al. 2015). In any case, it was found that, independently on how thermal photons are produced, such a high value of linear polarisation in the signal is extremely unlikely to be reproduced by models in which QED vacuum polarisation effects are not accounted for. Therefore, the VLT polarimetric measurement constitutes the very first observational support for the predictions of QED vacuum polarisation effects.

This important result needs further confirmation. For instance, in the optical band longer follow-up polarimetry observations of RX J1856 will improve this measurement and make the observational support to the QED predictions more robust. Optical polarimetry measurements of some other XDINSs would be obviously important to consolidate this result, although such measurements would be more challenging owing to the fact that other XDINSs are even fainter than RX J1856 (Kaplan et al. 2011). Imaging polarimetry capabilities at the next generation of 30-40m class telescopes, such as the European Extremely Large Telescope (E-ELT), would then play a crucial role in testing QED predictions of vacuum polarisation effects on a larger sample. An even more promising possibility to test further QED vacuum birefringence is given by the future generation of X-ray polarimetry missions. Potential X-ray observation of other magnetised sources, such as magnetars, is going to be discussed in the next chapter.

Measurements of the circular optical polarisation, never obtained so far for any isolated NS other than the Crab pulsar (Wiktorowicz et al. 2015), should also be pursued. Circular polarisation for thermal radiation coming from the neutron surface is zero in the approximation adopted in the present work (a sharp boundary for the adiabatic region, see Chapter §2) and, according to the numerical simulations, it is expected not to exceed 1–2% even accounting for the presence of an intermediate region, the only place where circular polarisation can be created (Taverna et al., 2014, 2015). The measurement of such a small polarisation degree could be attainable, again, only exploiting the high throughput of the next generation of extra-large telescopes.

Chapter 4

X-ray polarimetry of magnetars

The optical polarimetry observations of the XDINS RX J1856.5−3754 discussed in Chapter §3 showed a first evidence for QED vacuum birefringence induced by a strong magnetic field. This important result can be confirmed by performing systematically polarimetry observations in the X-ray band for other strongly magnetised NSs, such as transient or persistent magnetars. These sources are brighter than XDINSs, with X-ray luminosities $L_X \sim 10^{34} - 10^{36}$ erg s^{-1}, for persistent magnetars, and $L_X \lesssim 10^{36}$ erg s^{-1} (at the flux peak), for transient magnetars. As such, they are targets that can be observed by future X-ray polarimetry missions under development such as IXPE (NASA, Weisskopf et al. 2013) and eXTP (CAS, Zhang et al. 2016).

In this chapter, I extend the polarimetric models of XDINSs, discussed in Chapter §2, to the case of magnetars. At variance of XDINSs, magnetars are active sources that show large variability in their X-ray luminosity. I model the polarisation properties of the thermal component of the X-ray spectrum of magnetars. In particular, I consider the case in which this component is associated to emission from the NS surface. I show that polarimetric observation of magnetars can be used as a test for vacuum birefringence effects and for the magnetar model itself.

4.1 Introduction

Magnetars are strongly magnetised NSs, with magnetic fields as strong as $B \sim 10^{14} - 10^{15}$ G. These sources (observed as AXPs and SGRs) show variability in their persistent X-ray emission over a timescale of years, characterised by large flux changes (by 1 up to 3 orders of magnitude) and drastic alterations in the spectral and timing properties (see Chapter §1). The so-called transient magnetars, a subclass of magnetars, present the far end of this behavior (Turolla et al., 2015; Kaspi and Beloborodov, 2017). In representative sources, such as XTE 1810−197 and CXOU J164710.2−455216, a sudden outbursts was observed in which the X–ray flux increased, in a timescale of hours, up to 3 orders of magnitude. The associated X–ray flux decay has continued for a few years after the event and has been monitored extensively with XMM-Newton (Albano et al., 2010; Rea and Esposito, 2011).

The soft X–ray spectrum (below $\sim$ 10 keV) of transient and persistent magnetars is typically described by a two components model, consisting of a blackbody plus a power law or a double blackbody (Chapter §1, see also Turolla et al., 2015; Kaspi and Beloborodov, 2017). While the thermal component is thought to be reprocessed by an atmosphere, the non-thermal component is thought to be associated to thermal photons that underwent resonant cyclotron scattering (RCS) by charge particles in a twisted magnetosphere (Thompson et al., 2002; Fernández and Thompson, 2007). RCS models have been successfully applied to the spectrum of magnetars, validating the twisted magnetosphere model (Rea et al., 2008; Zane et al., 2009). X–ray polarimetry will complement this kind of spectral analysis by removing the degeneracy in the fitting parameter space (twist angle, charge velocity, source geometry) of RCS model and will provide a further test for vacuum birefringence effects (Fernández and Davis, 2011; Taverna et al., 2014). In particular, future missions, such as the Imaging X–ray Polarimetry Explorer (IXPE, Weisskopf et al. 2013) and the enhanced X–ray Timing and Polarimetry mission (eXTP, Zhang et al. 2016), will allow us to perform X–ray polarimetry in the $2 - 10$ keV range in persistent and transient magnetars (see Section §4.5).

In this chapter, I model the polarisation properties of transient and persistent

magnetars, extending the work on XDINSs that I have presented in Chapter §2. Here, the main goal is to study the polarisation properties of the thermal component of these sources when RCS effects are negligible, but a slightly twisted magnetosphere may still be present. Hence, the results are relevant for those magnetars with a more thermal soft X–ray spectrum (modelled by multiple blackbodies) and a less developed or absent power law component. We can also argue that these results can be applied to magnetars with thermal plus non-thermal spectral components (below 10 keV) provided that the application is limited to their thermal emission and under the assumption that RCS affects equally ordinary and extraordinary seed photons.

I model both, phase-averaged and phase-resolved polarisation quantities, adopting as input for the model parameters the observations of XTE 1810-197 and CXOU J164710.2-455216. Particular attention is given to the search for the signal of QED vacuum birefringence.

4.2 Twisted magnetospheres

The bursting activity and high luminosity observed in anomalous X–ray pulsars and Soft-gamma repeaters is thought to be powered by strong toroidal magnetic fields in the NS interior (see Chapter §1). The outbursts and subsequent flux decay observed in these sources are explained in the magnetar model in terms of catastrophic instabilities leading to a reconfiguration of the magnetosphere (Thompson et al., 2002). In particular, the internal toroidal field may transfer some helicity to the external magnetic field via plastic deformations or starquakes of the solid NS crust, producing a twisted magnetosphere. This twisted field evolves and gradually untwists (Beloborodov, 2009; Kaspi and Beloborodov, 2017), dissipating magnetic energy until, eventually, a nearly dipolar, stable configuration is reached

Twisted magnetosphere are non-potential,

$$\nabla \times \mathbf{B} = \frac{4\pi}{c}\mathbf{j}, \tag{4.1}$$

and they can sustain large currents, $\mathbf{j}$, of charged particles. These particles move along the twisted field lines with large Lorentz factors and return to the star sur-

face, producing a particle bombardment. The energy deposited at the magnetic pole produce a hot polar cap[1]. Most of the thermal radiation from the hot polar cap is expected to be produced in the soft X–ray band, with the polarisation properties determined by both, the magnetic topology at the star surface and by vacuum polarisation in the magnetised vacuum around the star, far from the star surface, i.e., at the adiabatic radius (see Chapter §2).

In the following, the topology of the external magnetic field is assumed to be described by a globally twisted dipole magnetosphere. The polar components of axisymmetric, self-similar solutions for globally twisted fields can be written as (Thompson et al., 2002)

$$\mathbf{B} = \frac{B_{\rm p}}{2}\left(\frac{r}{R_{NS}}\right)^{-p-2}\left[-f', \frac{pf}{\sin\theta}, \sqrt{\frac{C(p)\,p}{p+1}}\frac{f^{1+1/p}}{\sin\theta}\right], \tag{4.2}$$

where $B_{\rm p}$ is the strength of the field at the magnetic pole, and the function f (that depends on $\mu = \cos\theta$) is solution of the Grad-Shafranov equation (a second order differential equation). This function together with the function C can be obtained once that the input parameter p, related to the shear of the twisted field, is specified (Thompson et al., 2002; Pavan et al., 2009).

The amount of shear of the twisted field can be, alternatively, quantified by (Thompson et al., 2002)

$$\begin{aligned}\Delta\Phi &= \int_{\text{field line}} \frac{B_\phi}{(1-\mu^2)B_\theta}\mathrm{d}\mu \\ &= \left[\frac{C(p)}{p\,(1+p)}\right]^{1/2}\int_{\text{field line}}\frac{f^{1/p}}{1-\mu^2}\mathrm{d}\mu\,,\end{aligned} \tag{4.3}$$

which shows that different values of p correspond to fields with different shear. In particular, the effect of decreasing p is to increase B_ϕ with respect to the other components, and consequently to increase the shear. From $\Delta\Phi = 0$ to π, the solutions vary from a dipole field configuration ($p = 1$) to a split monopole configuration

[1] NSs may have complex magnetic field topologies, including non-polar twisted bundles. However, these kind of configurations are not discussed in this work.

($p = 0$).

4.3 Magnetar model

The phase-averaged and phase-resolved polarisation properties are studied for magnetars with untwisting magnetospheres, assuming a globally twisted dipole field (Thompson et al., 2002; Pavan et al., 2009). The mass and radius of the NS are assumed to be $M = 1.5 M_{\odot}$ and $R = 12$ km, respectively. Based on observational studies of representative sources such as XTE J1810−197 and CXOU J164710.2−455216 (Albano et al., 2010), the thermal emission from the magnetar is modeled assuming it is dominated by one hot polar cap, located at one of the magnetic poles, covering $\sim 15\%$ of the star surface.

Furthermore, it is assumed that during an outburst, at the X–ray flux peak, the magnetosphere has a twist angle $\Delta\Phi = 1.0$ rad and the hot polar cap has a uniform temperature of $T = 1.0$ keV. When quiescence is reached, at the end of the X–ray flux decay, the magnetosphere has untwisted by $\Delta\Phi = 0.5$ rad and the polar cap cooled down to $T = 0.5$ keV. These values are reminiscent of those inferred by Albano et al. (2010), while analysing the outburst decay of XTE J1810−197 and CXOU J164710.2−455216. As it is going to be explained in the following sections, the model here presented can also give us information about the properties of persistent magnetars.

The X–ray thermal radiation is assumed to be produced in a magnetised atmosphere composed of fully-ionised hydrogen. The intensities for the O-mode and X-mode are obtained by solving the radiative transfer equation coupled with the hydrostatic and energy balance equations and using the same atmosphere model presented in Chapter §2 and §3. I assume a polar magnetic field $B_{\rm p} = 10^{14}$ G, perpendicular to the surface. These intensities are, then, used to model the thermal emission from the hot polar cap, neglecting the variation of the magnetic field over the relatively small extension of the emitting region. For obtaining the polarisation quantities accounting for vacuum birefringence, the models are computed following the procedure previously discussed for XDINSs (see Chapter §2), in which the

Stokes parameters are calculated at the adiabatic radius. I consider thermal emission from the magnetar in the $E = 2 - 6$ keV energy range, which is potentially detectable by IXPE (see Appendix §4.A) and eXTP missions (see Appendix §4.B). Due to the relatively hot temperature of magnetars, it is unlikely that condensation occurs, therefore I do not consider the case in which the emission originates from a solid crust.

4.4 Results

4.4.1 Phase-averaged polarisation fraction

First, the polarisation properties are studied by varying the size of the hot polar cap. Figure 4.1 shows the phase-averaged polarisation fraction for a NS with a twisted field and accounting for vacuum birefringence effects. As generally expected, for some viewing angles the phase-averaged polarisation fraction can be as high as $\sim$ 99% due to vacuum birefringence effects. If the size of the polar cap (semi-angle of the polar cap aperture, β_c) is reduced from $\beta_c = 65^\circ$ to $\beta_c = 15^\circ$, the most significant difference is produced for regions of viewing geometry in which $\chi \gtrsim 140^\circ$ (line of sight relative to the spin axis) and $\xi \lesssim 40^\circ$ (magnetic axis relative to the spin axis), where the polar cap is not visible and, as a consequence, no polarisation is observable.

If vacuum birefringence is not accounted for and the size of the polar cap is relatively small ($\beta_c = 15^\circ$), as shown in Figure 4.2 (left panel), the phase-averaged polarisation fraction can be substantially high. In fact, for some viewing angles, the polarisation can be as high as $\sim 99\%$. Here, as the emitting area of the star is small, the depolarisation effects due the rotation of the Stokes parameters are less important since the the magnetic field distribution over the small region in view looks more uniform. On the contrary, if the size of the polar cap is increased, $\beta_c = 65^\circ$, then the depolarisation effects due to the rotation of the Stokes parameters become more important since the region in view contains a larger area with a non-uniform magnetic field topology.

It should be also noticed that, when the size of the polar cap is relatively large,

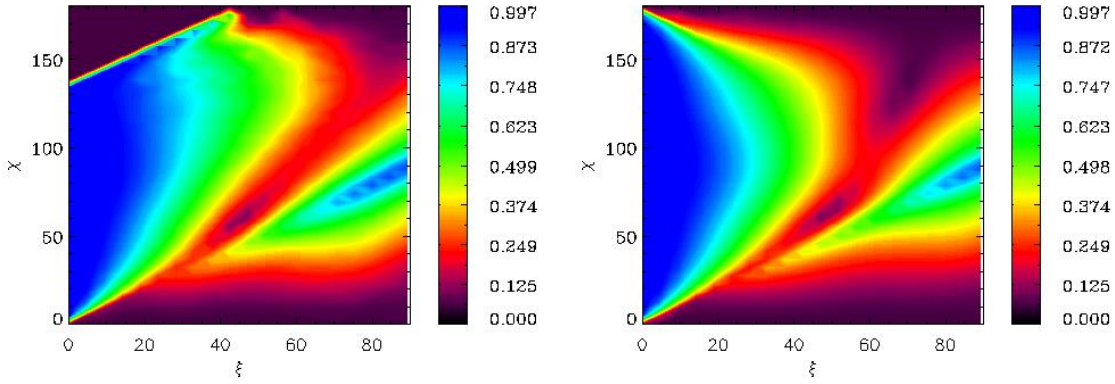

Figure 4.1: Phase-averaged polarisation fraction accounting for vacuum birefringence effects for a NS with one hot polar cap, temperature $T = 0.5$ keV, magnetic field strength $B_{\rm p} = 10^{14}$ G and magnetic twist $\Delta\Phi = 0.5$. **Left panel**: polar cap size $\beta_c = 15^{\circ}$. **Right panel**: polar cap size $\beta_c = 65^{\circ}$.

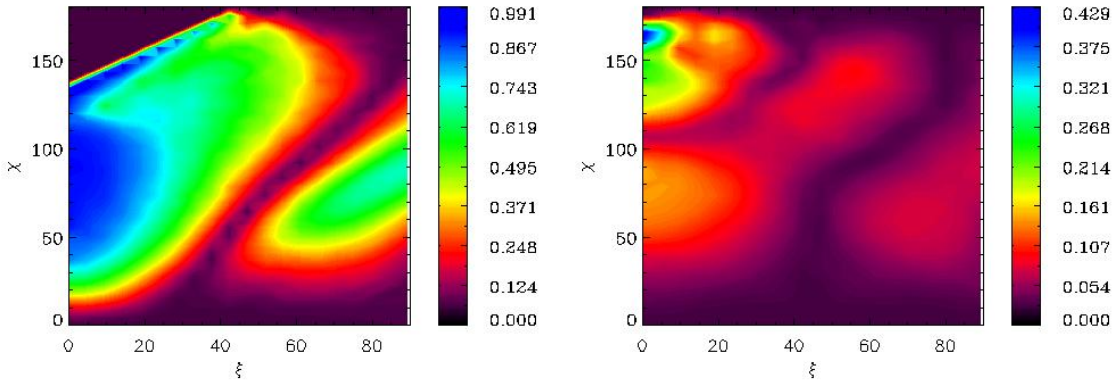

Figure 4.2: Same as Figure 4.1, but vacuum birefringence is not accounted for.

even if QED is not accounted for, there are still viewing angles at which a relatively high phase-averaged polarisation fraction can be observed. As shown in Figure 4.2 (right panel), for viewing angles $\chi \gtrsim 150^{\circ}$ and $\xi \approx 0^{\circ}$, the phase-averaged polarisation fraction can be as high as $\sim 43\%$, which corresponds to the viewing geometry in which only a small fraction of the emitting polar cap is within line of sight. As already explained above, for a small area in view the depolarisation effects due the magnetic topology (at the surface) are not important and, so, the observed polarisation can be relatively high. In principle, this means that one can conclude that the detection of a polarisation signal as high as $\sim 43\%$ from a relatively large polar cap ($\sim 65^{\circ}$) is not sufficient to discriminate models with or without QED account for. However, since in the case QED off the visible emitting area is small,

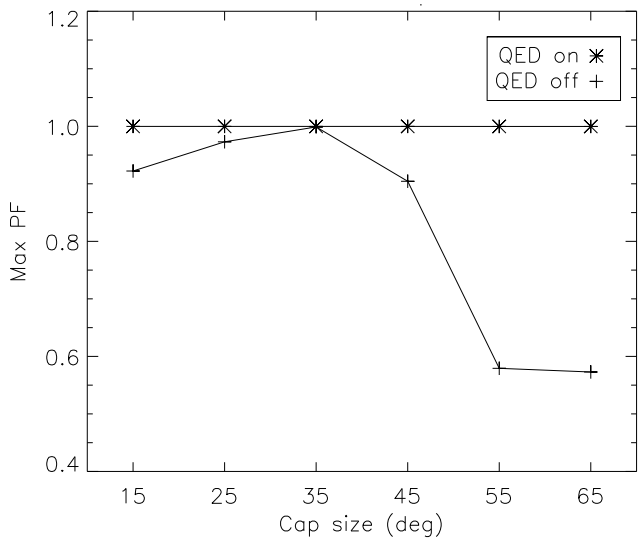

Figure 4.3: Maximum phase-averaged polarisation fraction for different sizes of the polar cap β_c, accounting (asterisks) or not (crosses) for vacuum birefringence.

the total flux for this viewing geometry should be also lower, which in practice could make this polarisation undetectable. In fact, for this viewing geometry, less than $\sim 2\%$ of the total luminosity from the polar cap would be observable.

The results discussed above do not show significant variations by changing either the temperature of the polar cap (for instance setting $T = 1.0$ keV) or the twist of the magnetic field (increasing to $\Delta\Phi = 1.0$ or assuming just an untwisted dipole field). Once again, this means that at least qualitatively the same results are representative of the thermal emission observed in persistent magnetars. However, as shown in Figure 4.2, when vacuum birefringence is not accounted for, the polarisation pattern can change substantially for different polar cap sizes. In order to re-assess and maximise this effect, the phase-averaged polarisation fraction was recomputed for different sizes of the polar cap and for the viewing geometry that produce the largest polarisation fraction (pretty close to an aligned rotator $\chi \sim 90^\circ$ and $\xi \sim 0^\circ$).

Figure 4.3 shows that when vacuum birefringence is accounted for, as already discussed, the phase-averaged polarisation fraction is almost 100%, independent on the size of the polar cap. However, when vacuum birefringence is not present, the phase-averaged polarisation fraction can change from $\approx 60\%$ (for a relative large

polar cap) to nearly $\approx 100\%$ (for a small polar cap). In particular, this may be an interesting result since in the magnetar model an untwisting magnetosphere is expected to produce a hot polar cap that shrinks over time (Beloborodov, 2009). Therefore, if vacuum birefringence is not present, the associated polarisation fraction should increase as the magnetosphere untwists, while it should remain constant if QED is at work.

4.4.2 Phase-averaged polarisation angle

As discussed in Chapter §2 and §3, measurements of phase-averaged polarisation angles can give us important information about the geometry of XDINS systems, such as inclination of the magnetic axis with respect to the spin axis. However, those calculations are based on the assumption of a NS with a core centered dipole magnetic field. In magnetars, instead, the magnetic field topology might be more complex, with e.g., extra multipolar components and twisted external fields. Here, using the model discussed in the previous sections, the impact of an untwisting magnetosphere (predicted by the magnetar model) on the polarisation angles is also assessed.

Figure 4.4 shows the variation of the phase-averaged polarisation angle, after an outburst, from the onset (globally twisted dipole with $\Delta\Phi = 1.0$ and polar cap with $T = 1.0$ keV) until the the end of the X–ray flux decay ($\Delta\Phi = 0.5$ and $T = 0.5$ keV). If vacuum birefringence is accounted for, and the region of viewing angles is restricted to the case in which the phase-averaged polarisation fraction is higher than 50% (i.e., which provides a real chance to measure the polarisation angle), the variation of the phase-averaged polarisation angle from the onset until the end of the flux decay can be as large as $\approx 23^\circ$ (Figure 4.4, left panel). Instead, if vacuum birefringence is not operating, the variation of the polarisation angle is lower than $\approx 14^\circ$ (Figure 4.4, right panel). Notice that in this case **a)** the range of modelled viewing angles is restricted to phase-averaged polarisation fraction larger than 5% and **b)** the largest variation of the polarisation angle is attained at viewing angles $\chi \approx 135^\circ$ and $\xi \lesssim 5^\circ$, where just small fraction of the polar cap is in view (and so, the flux is substantially reduced). From these results, it is possible to conclude

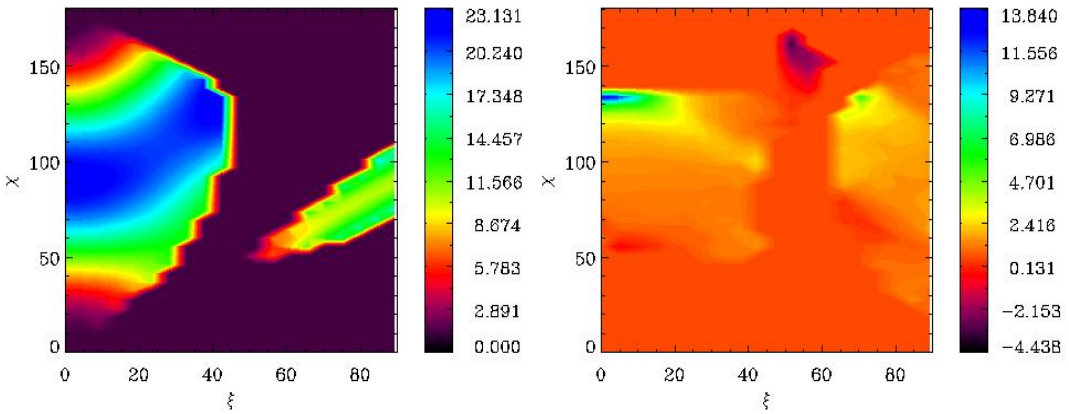

Figure 4.4: Variation of the phase-averaged polarisation angle for a NS with a polar cap size $\beta_c = 45^\circ$ and $B_p = 10^{14}$ G. The magnetosphere untwist from $\Delta\Phi = 1.0$ rad to $\Delta\Phi = 0.5$ rad. **Left panel**: accounting for vacuum birefringence. **Right panel**: vacuum birefringence is not present.

that a potential measurement of a variation of the phase-averaged polarisation angle larger than $\approx 15^\circ$ may be a strong evidence of both vacuum birefringence effects and an untwisting magnetosphere (as predicted by the magnetar model).

4.4.3 Phase-resolved polarisation fraction

The polarisation properties are also expected to change at different phases of the star rotation. For completeness, phase-resolved calculation are discussed in this section for thermal emission of magnetars with twisted magnetospheres.

Figure 4.5 and 4.6 shows the results for fixed viewing angles $\chi = 90^\circ$ and $\chi = 150^\circ$ (i.e, angle between spin axis and line of sight), respectively, and varying the ξ angle (spin axis and magnetic axis). If vacuum birefringence is accounted for, the phase-resolved polarisation fraction is always nearly 100% (see fourth panel) as long as a fraction of the polar cap is in view (see third panel). Of course, for large inclinations of the magnetic axis respect to the spin axis ($\xi \gtrsim 70^\circ$) the polar cap disappears at some rotational phases, which is reflected in the absence of signal in both the light curve and the polarisation fraction.

Instead, if vacuum birefringence is not present, the polarisation fraction shows a strong dependency on the rotational phase. In particular, a high (low) polarisation fraction is produced at rotational phases in which a small (large) fraction of

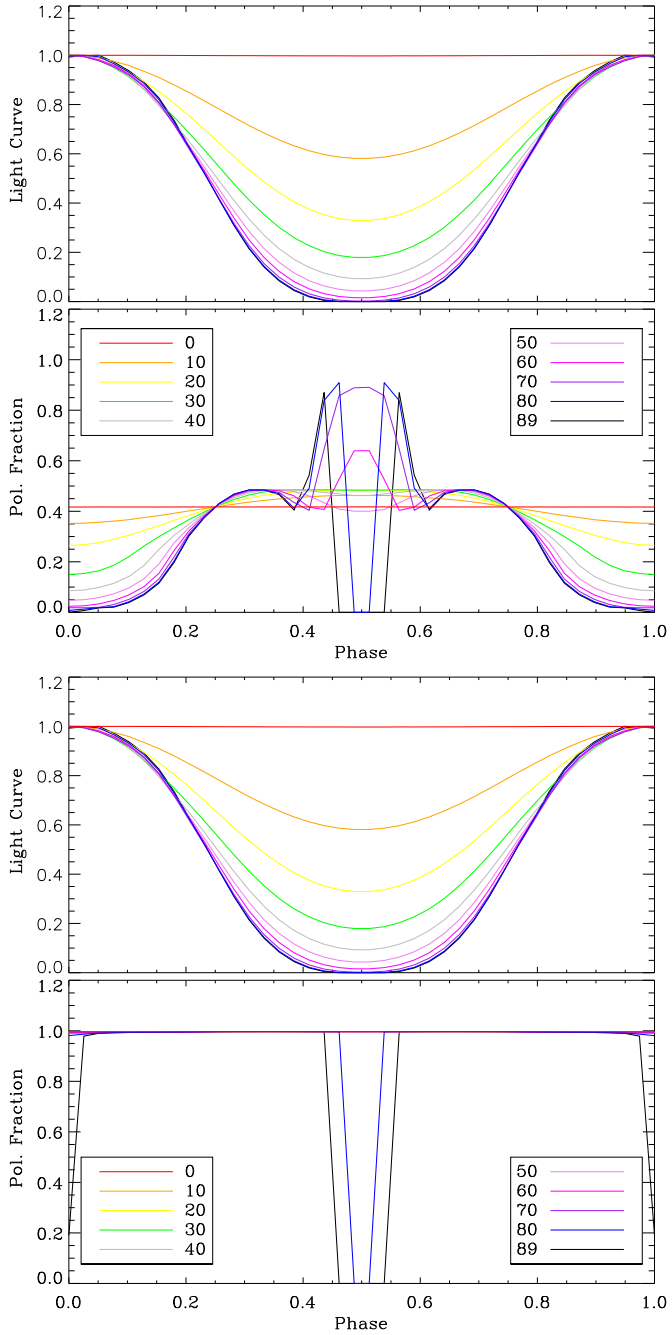

Figure 4.5: Phase-resolved polarisation fraction for $\chi = 90^\circ$ and different ξ angles. All curves are computed for the magnetar at the onset of the X–ray flux decay ($\Delta\Phi = 1.0$ rad and $T = 1.0$ keV). The panel above the phase-resolved polarisation fraction show the X–ray light curve. **First and second panel**: vacuum birefringence is not present. **Third and fourth panel**: accounting for vacuum birefringence.

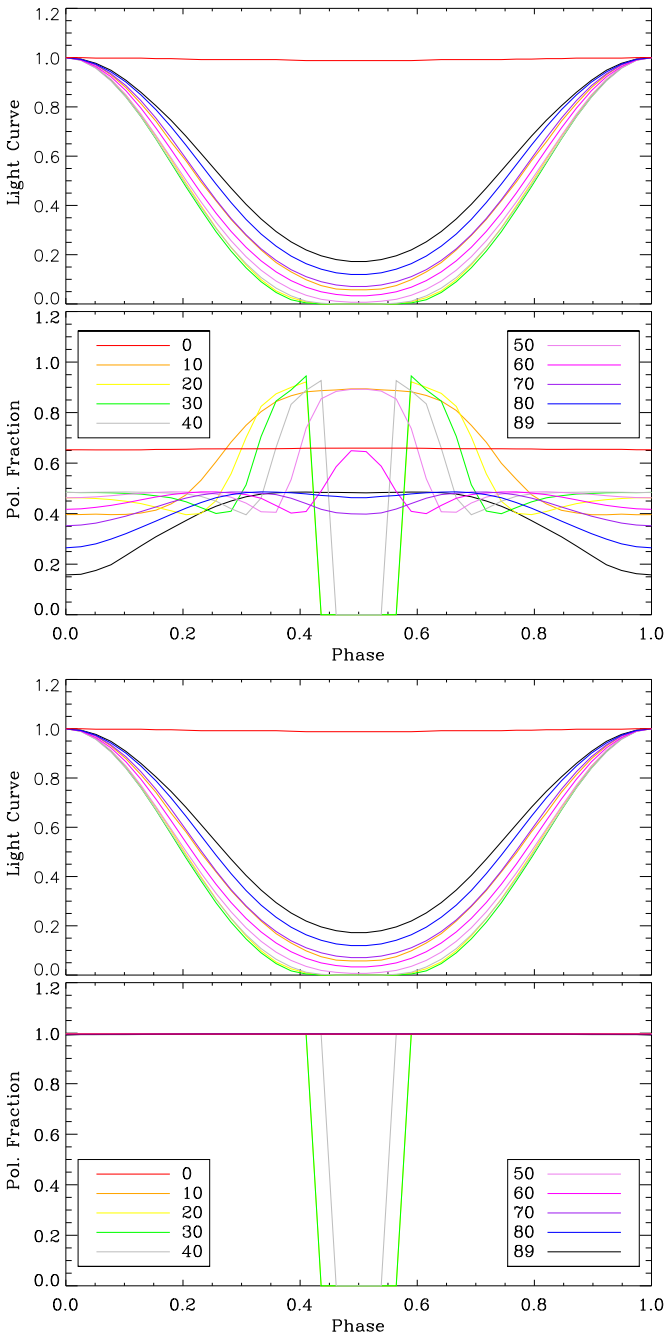

Figure 4.6: Same as Figure 4.5, but for $\chi = 150^\circ$ and different ξ angles.

the polar cap is in view. As discussed in previous sections, this is due to the depolarisation effects by the magnetic topology (and rotation of the Stokes parameters), which are not important for small emitting regions, and so translates in a signal with substantially high polarisation fraction.

The results discussed above confirm the large effects introduced by vacuum birefringence, which are also consistent with previous studies (Heyl and Shaviv, 2002; Fernández and Davis, 2011; Taverna et al., 2014). It should be noticed that in principle these results were computed for values of surface temperature and twist angle which are representative of the onset of the X–ray flux decay of sources as XTE J1810–197 and CXOU J164710.2–455216 ($\Delta\Phi = 1.0$ rad and $T = 1.0$ keV, Albano et al., 2010). However, no substantial differences are produced in the polarisation fraction by varying either the twist of the external magnetic field or the temperature of the polar cap, making the qualitative behaviour more general and applicable to persistent and transient magnetars with similar properties.

4.4.4 Phase-resolved polarisation angle

Figures 4.7 and 4.8 show the phase-resolved polarisation angle at the onset and at the end of the X–ray flux decay. If vacuum birefringence is operating, it is interesting to notice how the whole polarisation angle swing, for $\xi \lesssim 20^\circ$, is shifted by $\approx 20^\circ$ from the onset (Figure 4.7, fourth panel) to the end of the X–ray flux decay (Figure 4.8, fourth panel). This result is consistent with the analysis discussed for the variation of the phase-averaged polarisation angle (see Section §4.4.2). In addition, it can be noticed that the twisted field introduces a remarkable deviation from a sinusoidal shape in the polarisation angle swing, for viewing angles $\xi \gtrsim 20^\circ$, consistent with the results discussed in Fernández and Davis (2011) and Taverna et al. (2015). However, as the magnetosphere untwists (end of the X–ray flux decay), this deviation becomes smaller (in the limit of $\Delta\Phi = 0$ rad, i.e., dipole field, the polarisation angle swing recovers the sinusoidal shape).

If vacuum birefringence is not present (Figure 4.7 and 4.8, second panel), there is nearly no change in the polarisation angle for viewing angles $\xi \lesssim 40^\circ$. Instead, for a relatively large inclination of the magnetic axis respect to the spin axis, $\xi \gtrsim 40^\circ$,

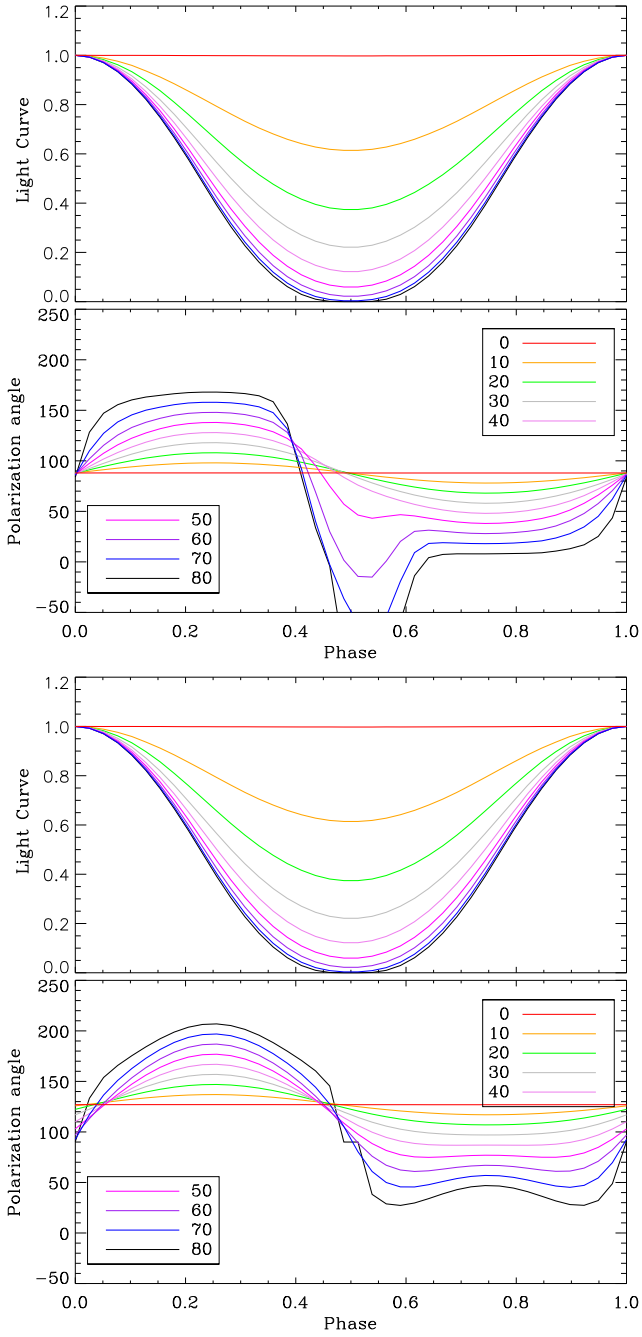

Figure 4.7: Phase-resolved polarisation angle for $\chi = 90^\circ$ and different ξ angles, at the onset of the flux decay ($\Delta\Phi = 1.0$ rad and $T = 1.0$ keV). The panel above the phase-resolved polarisation angle show the X–ray light curve. **First and second panel**: vacuum birefringence is not present. **Third and fourth panel**: accounting for vacuum birefringence.

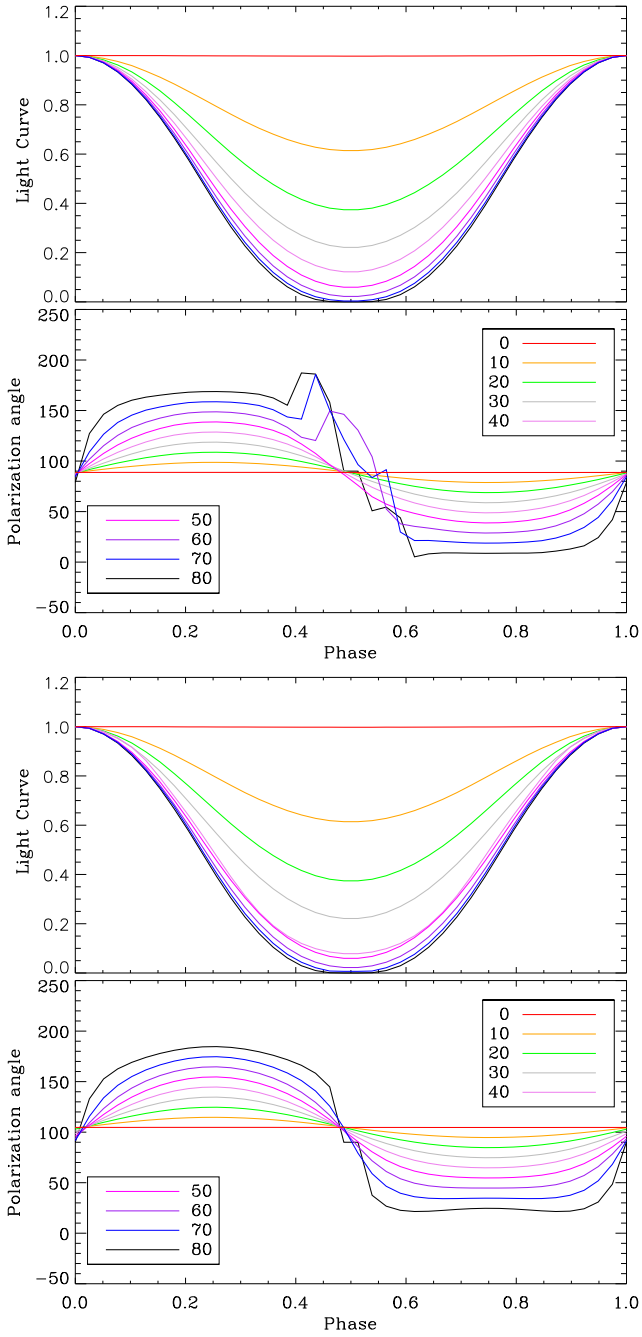

Figure 4.8: Same as Figure 4.7, but at the end of the X–ray flux decay ($\Delta\Phi = 0.5$ rad and $T = 0.5$ keV).

the polarisation angle swing shows a large variation as the magnetosphere untwists. This variation is particularly large at phases in which the polar cap is moving out of the line of sight.

The results discussed above show again that phase-averaged and phase-resolved measurements of the polarisation angle can complement each other and give us clear signal of vacuum polarisation effects and, in sources with a flux decay after an outburst, also of an untwisting magnetosphere (predicted in the magnetar model).

4.5 Chapter summary and discussion

The results of this chapter can be summarised as follows:

a) Similar to previous results obtained for XDINSs (see Chapter §2), the super-strong magnetic field surrounding magnetars can boost the observed polarisation fraction (either phase-averaged or phase-resolved measurements) of the thermal radiation, via the effect of vacuum birefringence, up to $\sim 99\%$ (considering the most favourable viewing geometry $\chi \sim 90^{\circ}$ and $\xi \sim 0^{\circ}$ for phase-averaged measurements).

b) When vacuum birefringence is operating and the magnetar has an untwisting magnetosphere, the value of the phase-averaged polarisation angle can change up to 23° (from the onset until the end of the X–ray flux decay, assuming an untwist of 0.5 rad). This offers an interesting test for both, the magnetar model and the vacuum birefringence effect.

c) If vacuum birefringence is not present and the polar cap shrinks during the magnetar flux decay, it was found that the phase-averaged polarisation fraction may increase from $\sim 65\%$ up to $\sim 99\%$. Instead, if vacuum birefringence is operating, the phase-averaged polarisation fraction remains almost constant independently on the cap size. This is an interesting result as it represents a further test on the magnetar model and the detection of a nearly constant phase-averaged polarisation fraction as the decay proceeds will provide a further evidence for the presence of vacuum birefringence effects.

The IXPE and eXTP missions (Appendix §4.B and 4.A) will be able to perform X–ray polarimetry in 2−6 keV energy range, relevant for the study of magnetars. Simulations (based on parameters for XTE J1810−197 and CXOU J164710.2−455216, Albano et al., 2010) show that in order to observe a phase-averaged polarisation fraction $\sim 70\%$ and to measure a polarisation angle with a precision[2] of $\sim 5^\circ$, at the onset of the outburst (with a flux $\sim 10^{-11}$ erg/cm^2/s, Bernardini et al., 2009; An et al., 2013), the observation time required by eXTP and IXPE are ~ 3 ks and ~ 20 ks, respectively. At the end of the X–ray flux decay, when the magnetar is in quiescence (flux $\sim 5\times 10^{-13}$ erg/cm^2/s, Bernardini et al., 2009; An et al., 2013), the observation time required to perform the same measurements of the phase-averaged polarisation fraction and polarisation angle by eXTP and IXPE are ~ 60 ks and ~ 380 ks, respectively. Furthermore, IXPE will likely allow to detect 1-2 transient magnetars during the planned mission lifetime.

The results presented in this chapter rely on a few assumptions. The first one: RCS has not a strong effect in the thermal component (soft X–ray) of the magnetar spectra. If this is not true, then it is expected a substantial reduction of the polarisation fraction (see Fernández and Davis, 2011; Taverna et al., 2014, for a discussion on RCS effects). On the other hand, for globally twisted magnetospheres, the polarisation angle depends only on the shear imparted on the field. In fact, as shown in Fernández and Davis (2011), the polarisation angle scales as $\Psi = \arctan(B_\phi/B_\theta) + \pi/2$, i.e., it shows no dependency on RCS effects, which means that the variation of the polarisation angle during the magnetar untwisting (when vacuum birefringence and RCS effects are operating) may be still observable.

The second assumption is that of an atmosphere in which the transport of radiation is driven by the cooling of the NS. However, in the magnetar model, the polar cap is heated by the particle bombardment (e^+e^- pairs) from returning magnetospheric currents. If the particle bombardment penetrates to very high optical depths, producing just a deep atmospheric heating, then the results discussed in this

[2]This precision can allow us to detect a potential variation of the polarisation angle of 10° during X–ray flux decay of a transient magnetar.

chapter might be still valid as the transport of radiation in the atmosphere would be similar to the case of a passively cooling NS. Instead, if the particle bombardment deposit some energy at low optical depths, then a hot layer might be present in the external region of the atmosphere (see Zane et al., 2000, for a discussion of the case of magnetised NSs accreting at low rates), which can modify substantially the thermal emission from the magnetar. This issue motivates the next research chapter, in which I study and compute a model for a magnetised grey atmosphere that accounts for particle bombardment.

X–ray polarimetry missions

Appendix 4.A IXPE mission

The Imaging X–ray Polarimetry Explorer (IXPE, Weisskopf et al. 2013) is a Small Explorer (SMEX) mission under development by NASA (Figure 4.10). This mission was selected on January 3, 2017. IXPE is planned to be launched by 2021, with an expected duration of 2 yr. Besides magnetars, the mission will observe targets such as active galactic nuclei, microquasars, pulsars (and pulsar wind nebulae), accreting X–ray binaries, supernova remnants, and the Galactic center. The

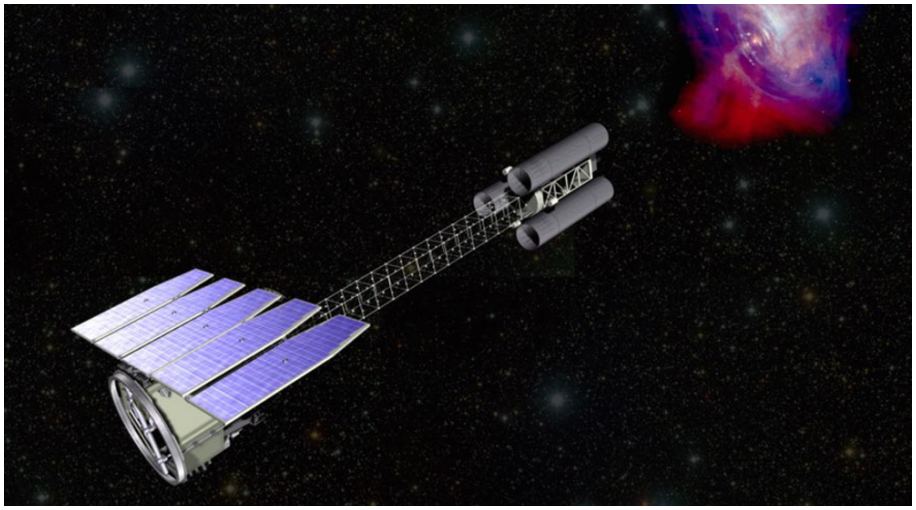

Figure 4.9: Artistic impression of the IXPE mission under development by NASA Marshall Space Flight Center (MSFC) in collaboration with Ball Aerospace, the Italian Space Agency (ASI) with Institute for Space Astrophysics and Planetology / National Institute of Astrophysics (IAPS/INAF), the National Institute for Nuclear Physics (INFN) besides the University of Colorado Laboratory for Atmospheric and Space Physics (LASP), Stanford University, McGill University, and the Massachusetts Institute of Technology. Image credit: NASA, https://ixpe.msfc.nasa.gov.

mission is aimed to determine, for example, the mechanisms for particle acceleration and X–ray emission, the magnetic field configuration and system geometry of X–ray sources, and to explore general relativistic and quantum effects in extreme environments.

The IXPE payload includes three X–ray telescopes with identical mirror modules and polarisation sensitive imaging detectors. Their main characteristics are listed below (Weisskopf et al., 2013).

- Polarimetry in the $2-8$ keV energy range.
- 100 μs time resolution.
- 5.5% minimum detectable polarization (MDP) for 0.5 mCrab[3] (exposure time of 10 days).
- $12'$ field of view.
- $\leq$ 30" angular resolution.

In particular, the technology of the X–ray polarimetry system consists of Gas Pixel Detectors (GPDs, Costa et al., 2001; Bellazzini et al., 2013). The concept is based on the anisotropy of the emission direction of photoelectrons produced by polarised photons. The GPD is able to track the path of these photoelectrons and, so, to infer with high sensitivity the polarisation state of incidents X–rays photons.

Appendix 4.B eXTP mission

The enhanced X–ray Timing and Polarimetry mission (eXTP, Zhang et al. 2016) is under development by the Chinese Academy of Sciences (CAS). The mission was selected by CAS on March 2, 2018 and it is planned to be launched by 2025. The mission is aimed to determine the equation of state of matter at supra-nuclear density, perform measurements of QED effects in highly magnetised stars, and study accretion in the strong-field regime of gravity. Primary targets include isolated and

[3] $0.5\ \text{mCrab} = 1 \times 10^{-11} \text{erg/s/cm}^2$

Figure 4.10: Artistic impression of the eXTP mission under development by CAS with the collaboration of institutions in several European countries and other international partners (see the full list in https://www.isdc.unige.ch/extp/consortium.html). Image credit: eXTP consortium.

binary NSs, strong magnetic field systems like magnetars, and stellar-mass and supermassive black holes.

The eXTP payload includes the following four instruments (Zhang et al., 2016):

- The Spectroscopic Focusing Array (SFA), which is an array of 11 X–ray telescopes that allow to perform observations in the $0.5 - 30$ keV band, with an angular resolution better than $1'$ and FOV of $12'$

- The Polarimetry Focusing Array (PFA), which consist of 2 telescopes that can perform observations in the $2 - 10$ keV band with angular resolution better than 30" (can reach 15") and FOV of $12'$. The time resolution of the instrument is 500 µs, the total effective area is 250 cm^2 (at 2 keV), and the sensitivity is about of 1 % MDP for a 100 mCrab source (with an exposure time of 50 ks). As the IXPE mission, the technology of the polarimetry detector is based on the GPD concept.

- The Large Area Detector (LAD), which is designed to observe in the $2 -$ 30 keV band (can be extended up to 80 keV for bright events). The LAD

effective area can be as large as ~ 3.4 m^2 (at 6 keV). The absolute time accuracy of the instrument is 1 μs and its sensitivity is 0.01 mCrab (for an exposure time of 10^4 s).

- The Wide Field Monitor (WFM), which has 3 pairs of coded mask cameras that can cover 3.7 sr of the sky, at sensitivity of 4 mCrab (for an exposure time of 1 day) in the $2-50$ keV band. The effective FOV of each camera pair is $\sim 70^\circ \times 70^\circ$. The absolute time accuracy of the instrument is 1 μs.

Chapter 5

Atmosphere of magnetars

The magnetosphere of strongly magnetised NSs, such as magnetars, can sustain large electric currents. The charged particles return to the surface with large Lorentz factors, producing a particle bombardment. In this chapter, I investigate the transport of radiation in the atmosphere of strongly magnetised NSs, in the presence of particle bombardment heating. I solve the hydrostatic and energy balance equations coupled with the radiative transfer equations for a grey atmosphere in the Eddington approximation, accounting for the polarisation induced by a strong magnetic field.

The solutions show the formation of a hot external layer and a low (uniform) temperature atmospheric interior. This suggests that the emergent spectrum may be described by a single blackbody with the possible formation of a optical/infrared excess (below ~ 1 eV). I also found that the polarisation fraction of the emergent X-ray radiation is strongly dependent on both the luminosity and penetration length of the particle bombardment. Therefore, the thermal emission from active sources, such as transient magnetars, in which the luminosity decreases by orders of magnitude, may show a substantial variation in the polarisation pattern during the outburst decline. These results are relevant in view of future X-ray polarimetric missions such as IXPE (NASA, Weisskopf et al. 2013) and eXTP (CAS, Zhang et al. 2016).

5.1 Introduction

The soft X-ray thermal component of the spectrum of magnetars is expected to be produced in an atmosphere. The existing atmospheric models of magnetised NSs are computed under the assumption that the NS is a "passive cooler", i.e. that the only heat source in the atmosphere originates from the star interior (see Chapter §1). This is quite an unrealistic simplifications for sources like magnetars, which are characterised by strong magnetospheric activity and are believed to possess complex magnetospheric configurations. For instance, as discussed in Chapter §4, in magnetars the external magnetic field is expected to be twisted. This non-potential, twisted magnetic field is sustained by large currents of charged particles that move along the twisted field lines and return toward the star surface (Thompson et al., 2002; Beloborodov, 2009). The energy deposited in the atmosphere is expected to raise the temperature of the most external atmospheric layers (Turolla et al., 1994; Zane et al., 2000) and affect the transport of radiation ("particle bombardment" effect). As such, the spectrum of magnetars may have substantial deviations from that of "passively" cooling NSs.

In this chapter, I present a model for the thermal emission from magnetised NSs under particle bombardment. I study the transport of radiation, in an atmosphere heated by a back-flow of charged particles from the magnetosphere. These particles are decelerated, by a number of physical processes, and deposit their energy in the atmospheric layer. I consider the case of a "grey" plane-parallel atmosphere and solve the polarised transport equations in the Eddington approximation coupled with the energy balance and hydrostatic equilibrium equations. Vacuum polarisation effects are accounted for as well as the effects of vacuum-induced resonances in the plasma layers, and model results are discussed. This work has been presented in detail in a journal paper (González-Caniulef et al., 2019).

5.2 Theoretical framework

5.2.1 Stopping length

Fast, returning, magnetospheric particles decelerate and deposit energy as they penetrate the atmosphere. In the case of an unmagnetised atmosphere, the stopping length for fast electrons is dominated by relativistic bremsstrahlung (Bethe and Heitler 1934; Heitler 1954; Tsai 1974, see also Ho 2007). For moderate magnetic fields, below $B \sim 10^{13}$ G, fast particles lose their kinetic energy mainly due to Magneto-Coulomb interactions[1], and the corresponding cross sections have been derived by Kotov and Kelner (1985) and Kotov et al. (1986). Since the particle stopping length in the case of strongly magnetised plasma, i.e. $B \gg 10^{13}$ G, is still not very well understood, the cross sections computed by Kotov and Kelner (1985) and Kotov et al. (1986) have also been used by Lyubarsky and Eichler (2007) in order to derive approximated results for the deceleration of fast particles at larger field strengths ($B \approx 10^{14} - 10^{15}$ G). In this work I will adopt the simplified approach.

The process that produces the particle deceleration can be explained as follows (see Figure 5.1). After impinging onto the atmospheric layer, returning magnetospheric particles move along the magnetic field lines, while occupying the fundamental Landau level. After a scattering with a plasma nucleus, the fast particle can make a transition to an excited Landau level. If the timescale for collisions between fast particles and plasma nuclei is larger than the de-excitation timescale to return to the fundamental Landau level, then a high energy photon is emitted and the fast particle returns to the fundamental Landau level before experiencing a new scattering. In the following I will refer to this regime as "low density plasma", which occurs when (Kotov and Kelner, 1985)

$$c\sigma_{01}n \ll \frac{1}{\gamma\tau}, \tag{5.1}$$

[1] Collisionless processes such as beam-instability (e.g., Godfrey et al. 1975) have been also proposed to contribute to the stopping length, although detailed calculations still need to be done (see Thompson and Beloborodov 2005; Beloborodov and Thompson 2007). However, Lyubarsky and Eichler (2007), have shown that collisionless dissipation does not work in the atmosphere of a NS because the two-stream instability is stabilised by the inhomogeneity (density gradient) of the atmosphere.

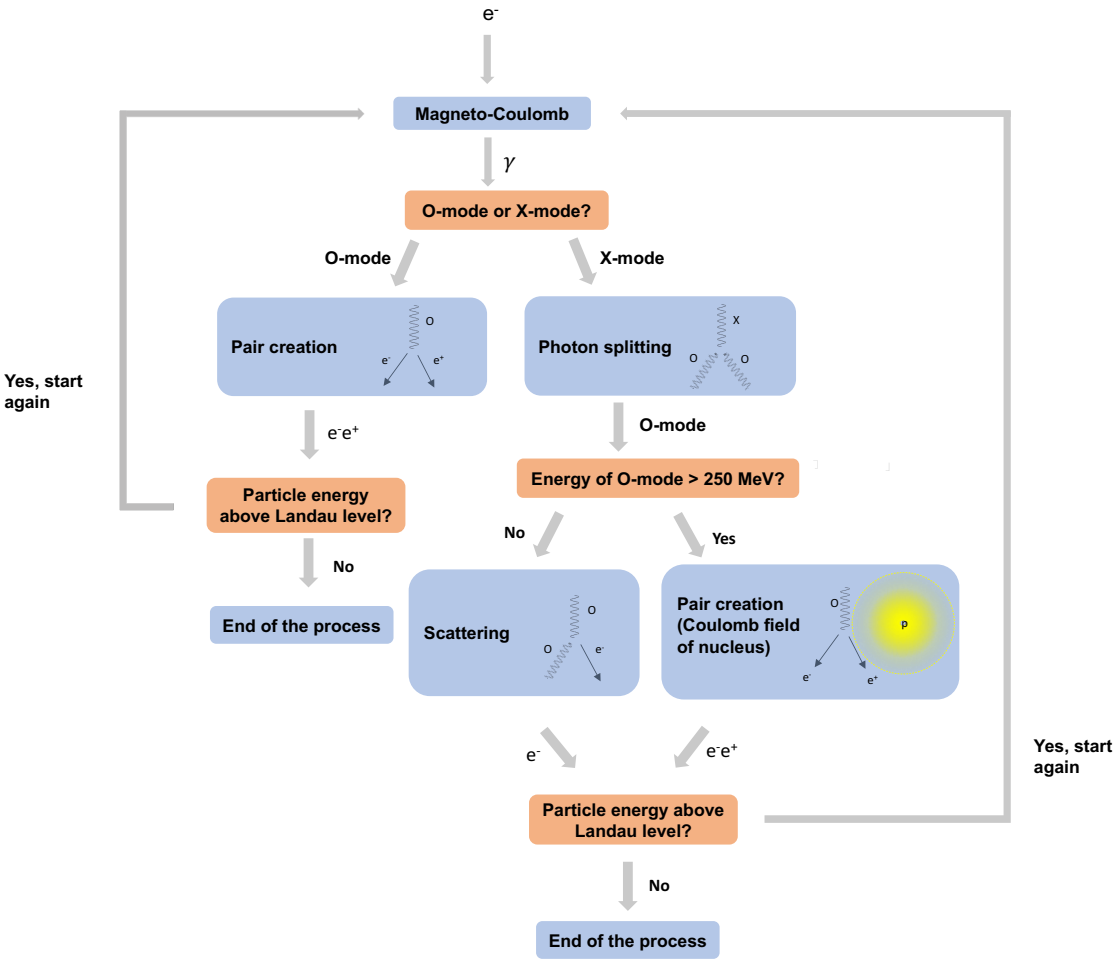

Figure 5.1: Electron-positron avalanche due to particle bombardment. The figure refers to magnetic field $B \sim 10^{15}$ G, in which case, after the initial Magneto-Coulomb interaction most of the energy is transferred to photons (either O- or X-mode) and the electron retains a limited fraction of its kinetic energy. The long, right hand side branch that departs after the Magneto-Coulomb interaction describes the different mechanisms triggered by an initial X-mode photon generated in a magneto-Coulomb interaction (under the assumption that O-mode photons resulting from the photon splitting have energy below the threshold for direct pair creation). In this branch, after a scattering, the O-mode photon transfer most of its energy to an electron (González-Caniulef et al., 2019).

where c is the speed of light, σ_{01} is the cross section for exciting the charged particle to the first Landau level, n is the number density of nuclei, γ is the Lorentz factor of the impinging particle, and τ is the life–time of the first excited Landau level.

As discussed by Lyubarsky and Eichler (2007), during collisional Landau level

excitations most of the energy is transferred to photons (the seed electrons retain only a small fraction of the total energy). The resulting gamma-rays can trigger an electron-positron pairs avalanche, ultimately leading to electrons with the energy below the Landau energy. If the pair avalanche is triggered by O-mode gamma rays (see the left hand branch after initial Magneto-Coulomb interaction in Figure 5.1), the typical length scale in which it occurs is roughly coincident with the stopping length of the charged particles and is given by (Lyubarsky and Eichler, 2007)

$$l_{Low} \approx \frac{2B}{3\xi_k B_q Z^2 n_i \sigma_T} \ln\left[\ln\left(\frac{0.4\gamma^2 B_q}{B}\right)\right], \tag{5.2}$$

where $\xi_k \approx 0.15(B/10^{15}\ \mathrm{G})^{-1/2}$ is the fraction of the kinetic energy retained by the electron after one scattering, $B_q = m_e c^3/\hbar e = 4.4\times10^{13}$ G is the critical quantum field, Z is the atomic number, σ_T is the Thomson cross section, and n_i is the number density of ions. For Lorentz factors $\gamma \sim 100-1000$ (as those attained by charged particles in untwisting magnetospheres, see Beloborodov 2009), this translates into a Thomson depth of

$$\tau_0 = \sigma_T Z n l_{Low} \approx 200 Z^{-1}\left(\frac{B}{10^{15}\,\mathrm{G}}\right)^{3/2}. \tag{5.3}$$

X-mode gamma rays do not produce pairs directly but they first split into O-mode photons (see the right hand side branch after the initial Magneto-Coulomb interaction in Figure 5.1). If the energy of the resulting O-mode photon is below the energy threshold for direct pair creation then **a)** pairs may be created via the interaction with the Coulomb field of a nucleus or **b)** the O-mode photon may transfer the energy to an electron via Compton scattering, which then may undergo a Magneto-Coulomb interaction. Lyubarsky and Eichler (2007) calculated the mean free path for successive production of X-mode photons for particles with Lorentz factor $\gamma = 10^3$, moving in a magnetic field of $B = 10^{15}$ G, finding that the avalanche can extend up to a relatively large optical depth

$$\tau_0 \approx 300 Z^{-1}. \tag{5.4}$$

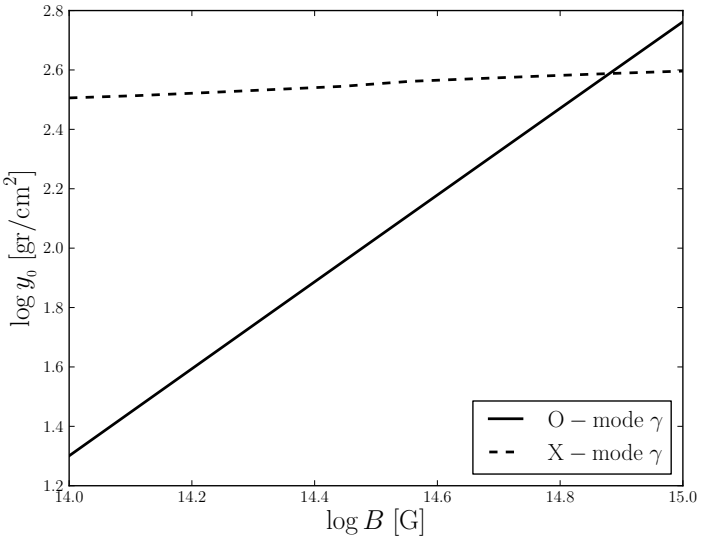

Figure 5.2: Stopping column density for different magnetic fields. The solid line shows the penetration length of the electron-positron avalanche produced by the initial O-mode photon branch (after a magneto-Coulomb interaction for particles with Lorentz factor $\gamma = 10^3$). The dashed line shows the penetration length of the electron-positron avalanche due to X-mode photons (González-Caniulef et al., 2019).

In a hydrogen atmosphere, this translates into a relatively large column density for stopping the successive production of X-mode photons $y_0 \sim 750$ g cm^{-2}, while seed electrons from the particle bombardment are stopped at $y_0 \sim 570$ g cm^{-2}. I have repeated the same calculations for a magnetic field $B = 10^{14}$ G, which is more representative of the sources that I aim to model, finding that the stopping column density is reduced to $y_0 \sim 250$ g cm^{-2} for X-ray photons, and to $y_0 \sim 20$ g cm^{-2} for seed electrons[2]. It should be noticed that, in the case in which the energy of the O-mode photon is above the threshold for direct pair creation, the pair avalanche penetrates the atmosphere up to a depth significantly less than that of equation (5.3). The stopping column densities for different magnetic fields for both the X-mode and O-mode branches are also shown in Figure 5.2.

[2]Notice that in a magnetised vacuum with $B \sim 10^{14}$ G, pair creation triggered by X-mode photons can also occur (see Section §5 of Weise and Melrose 2006). However, this process may change in presence of a magnetised plasma and no computations for the corresponding cross sections are available. In the following, I do not take this effect further into account.

In a "high" density plasma, i.e. such that $c\sigma_{01}n \gg 1/(\gamma\tau)$, the impinging charged particles can be excited, via successive scatterings, to Landau levels with large quantum numbers (Kotov et al., 1986). In this case, the electron mean free path has been calculated by Kotov et al. (1986), and is given by

$$l_{High} = 2.35 \times 10^8 \frac{B_q}{ZB} \left(\frac{\xi_k}{n\Lambda} \right)^{1/2}, \tag{5.5}$$

where Λ is the Coulomb logarithm. Potekhin (2014) compared this result with the geometrical depth obtained from the NS envelope models of Ventura and Potekhin (2001) and performed a numerical fit to find a simple analytic formula for the column density at which particles decelerate. Assuming that $\Lambda = 1$, this column density is given by[3]

$$y_{0,High} \approx \left[\left(\frac{A}{Z^2} \frac{\gamma}{700} \right) \left(\frac{B}{10^{12}\ \mathrm{G}} \right)^{-2} \right]^{0.43} \left(\frac{T}{10^6 \mathrm{K}} \right)\ \mathrm{g\ cm^{-2}}, \tag{5.6}$$

where T is the temperature of the atmosphere, which enters in the expression of the stopping length because a certain atmospheric model was used (Potekhin et al., 1999; Potekhin, 2000). It should be noticed that equation (5.6) scales with the magnetic field as $\propto B^{-0.86}$, which means that for stronger magnetic fields the stopping column density decreases, as well as the density at which particles lose most of their kinetic energy. Then, for strong magnetic fields, large Lorentz factors are required in equation (5.6) to satisfy the criterion of high density plasma. It is worth noticing also that, since the low stopping lengths inferred by equation (5.6) have been invoked to suggest the existence of a self-regulating mechanism driven by magnetospheric currents which may produce thin hydrogen layers on the surface of ultra magnetised NSs (Ho, 2007; Potekhin, 2014), the existence of such ultra-relativistic particles ($\gamma \sim 10^{14}$ for $B \sim 10^{13}$ G) is necessary in order to make the scenario self–consistent.

In a twisted magnetosphere, particles are accelerated to typical Lorentz factor

[3]Note that this expression differs from that presented by Potekhin (2014), since it contains corrections discussed in a private communication with Dr. Potekhin.

$\gamma \sim 10^3$. Considering magnetic fields $B \sim 10^{14}$ G, the cross section to excite particles to the first Landau level is $\sigma_{01} \sim 10^{-25}$ cm^2 (assuming $\Lambda = 1$), and the typical life-time of the process is $\tau \sim 10^{-19}$ s (Kotov and Kelner, 1985). This means that the condition of low density plasma (equation 5.1) requires $n \ll 10^{29}$ cm^{-3}, which is typically met across the NS atmosphere. Thus, in the following, only the stopping length corresponding to the low density case is considered. It should be noticed that the estimates for the stopping optical depth, equations (5.3) and (5.4), are based on cross sections for magneto-Coulomb interactions, photon splitting induced by the the magnetic field (or the Coulomb field of a nucleus), and Compton scattering processes (Klein-Nishina cross section) that are not accounting for all the complex physics of plasma in super strong magnetic fields. Detailed calculations for these processes in the magnetar regime are outside the scope of this study. Therefore, the analysis is done for a range of stopping column densities $y_0 = 65 - 500$ g cm^{-2}, fairly compatible with values previously discussed for particles decelerated in a low density plasma, in which the lower limit is representative of the penetration of the particle bombardment for magnetic fields $B \sim 10^{14}$ G, while the upper limit is representative of the penetration of successive X-mode photons production for $B \sim 10^{15}$ G. Both cases assume initial particle bombardment with Lorentz factor $\gamma = 10^3$.

Another important process that can contribute to the stopping length is resonant Compton drag. In fact, upon impinging on the atmosphere, electrons feel a hot photon bath (with typical temperature of $T \sim 10^7$ K, see next sections) and, in presence of a high magnetic field, may undergo significant resonant Compton cooling. This process has been investigated by Daugherty and Harding (1989), Sturner et al. (1995) and, more recently, by Baring et al. (2011) who calculated the electron cooling rate using the fully relativistic, quantum magnetic Compton cross section. As shown by Baring et al. (2011, see their Fig. 6), the electron cooling length scale varies considerably with both, the Lorentz factor of the charges and the photon temperature and reaches a minimum at the onset of the resonant contribution, in correspondence of $\gamma_r \approx B/(\Theta B_q)$, where $\Theta = kT/m_e c^2$. They found that, for $B \gg B_q$,

the absolute minimum of the Compton stopping length is

$$\lambda_C \sim \frac{2\tilde{\lambda} B}{B_q \alpha_F \Theta^3}\,, \tag{5.7}$$

where $\tilde{\lambda}$ is the reduced electron Compton wavelength, and α_F the fine structure constant. The previous expression strongly depends on the temperature.

For $B = 10^{14}$ G and $T = 10^7$ K, this gives $\lambda_C \sim 100$ cm, in correspondence of a Lorentz factor $\gamma \sim 10^3$. In turns, assuming a density $\rho \sim 10^{-3}$ g cm^{-3}, this translates into a stopping column density as small as $y_0 \sim 0.1$ g cm^{-2}. Indeed, by assuming that the Compton stopping length grows linearly with γ for $\gamma > \gamma_r$ (see the curves in Fig. 6 of Baring et al., 2011), it is possible to estimate that the Compton stopping length becomes larger than the stopping length for magneto-Coulomb collisions (so the latter effect becomes dominant) only if the charge Lorentz factor is $\gamma > 10^6$.

On the other hand, even considering $\gamma \sim 10^3$, it is important to stress that an expected value $y_0 \sim 0.1$ g cm^{-2} is an absolute lower limit, for several reasons. First, it assumes monoenergetic particles at γ_r. As soon as the Lorentz factor departs from this value, the resonant process becomes more inefficient and the Compton stopping length increases (extremely rapidly at lower γ, and almost linearly for $\gamma > \gamma_r$). Moreover, this value is estimated assuming that the radiation field is isotropic (while this is not expected to be the case in the external layers of our magnetized atmospheres) and the resonant conditions (which is in general angle-dependent) is met by all impinging charges.

In any case, while experiencing Compton drag, the cooling electrons produce hard X-ray/soft gamma-ray photons, primarily but not exclusively in the X-mode (Beloborodov, 2013; Wadiasingh et al., 2018), and these X-mode photons can split into O-mode photons, which can produce a pair cascade, contributing to the process previously described. In order to estimate the stopping length at which the pair cascade (and heat deposition) end, I can then repeat the same calculation as before, by using again a magnetic field $B = 10^{14}$ G. By assuming that a seed electron (stopped

at $y_0 = 0.1$ g cm^{-2}) with Lorentz factor $\gamma = 10^3$ transfers all the energy, or 1/2 of the energy, or 1/4 of the energy to a single X-mode photon, then the results are similar to the ones discussed before, i.e. the e^+e^- cascade stops at $y_0 = 326$ g cm^{-2}, $y_0 = 321$ g cm^{-2} or $y_0 = 187$ g cm^{-2}, respectively. This is because, during the cascade, the stopping column density is dominated by the characteristic length travelled by O-mode photons (produced by splitting of X-mode photons) before producing pairs, rather than the path travelled by the pairs themselves (which can be effectively stopped by resonant Compton drag at the site of creation).

In the following, I will carry on the analysis by considering a range of stopping column densities $y_0 \approx 65 - 500$ g cm^{-2}, which covers the scenarios described before for charges with impinging Lorentz factor $\sim 10^3$. In this range of values, it is possible to ensure the convergence of the numerical code. The potential effects of a larger Lorentz factor are briefly discussed in the conclusions and summary section.

For simplicity, it is assumed that the heat deposition is distributed uniformly along this depth, and is given by

$$W_H = L_\infty / 4\pi R^2 y_0 \tag{5.8}$$

where L_∞ is the luminosity at infinity and R is the star radius. This expression is valid as long as the velocity, v, of incoming magnetospheric particles is much higher than the thermal velocity of the plasma, v_{th}, which allows us to ignore collective plasma oscillation (Alme and Wilson, 1973; Bildsten et al., 1992). It is also assumed that the only heating source in the atmosphere is due to the particle bombardment, which means that $W_H = 0$ for $y > y_0$.

5.2.2 Radiative transfer

In the next sections, the transport of radiation is computed for magnetised atmospheres heated by particle bombardment induced by a twisted magnetosphere. According to Beloborodov and Thompson (2007), the twist current $\mathbf{j} = (c/4\pi)\nabla \times \mathbf{B}$ is maintained by a voltage Φ that is regulated by a e^+e^- discharge along the magnetic field lines. For a non-rotating NS with a twisted dipole, as the magnetosphere un-

twists, the cavity in which $\nabla \times \mathbf{B} = 0$ expands out from the equatorial plane, and the currents become concentrated in a "j-bundle" whose footprints are anchored near the magnetic poles. The evolution of the j-bundle, where the back bombarding currents are accelerated, produces a polar hot spot that shrinks over time. The luminosity associated to currents returning onto the NS surface is given by (Beloborodov, 2009).

$$L \approx 1.3 \times 10^{36} B_{14} R_6 \psi \mathscr{V}_9 u_\star^2 \text{ erg s}^{-1}, \tag{5.9}$$

where ψ is twist angle, $\mathscr{V}_9$ is a threshold voltage in units of 10^9 V, and

$$u_\star(t) \approx \frac{cR\mathscr{V}}{2\mu\psi}(t_{end} - t) \tag{5.10}$$

defines the (time dependent) magnetic flux surface in which is located the current front (or sharp boundary of the cavity), with $t_{end} = \mu\psi_0/cR\mathscr{V}$ the time required to erase the twist. Here, ψ_0 is the amplitude if the twist imparted by the starquake and μ is the magnetic dipole moment. Owing to the gravitational redshift, the total luminosity seen by a distant observer, L_∞, is related to the local luminosity at the top of the atmosphere by $L_\infty = y_G^2 L(0)$, where $y_G = (1 - R/R_s)^{1/2}$ is the gravitational redshift factor in a Schwarzschild spacetime for a star with radius R and Schwarzschild radius R_s.

The envelope material is assumed to be completely ionised hydrogen. In order to solve the energy balance and radiative transfer, I use the plane-parallel approximation and compute equilibrium solutions in the frequency-integrated case. I follow the same approach that has been used by Turolla et al. (1994), Zampieri et al. (1995), and Zane et al. (2000) for computing model atmospheres at low accretion rates in the non-magnetised and moderately magnetised regime (see also Zel'dovich and Shakura, 1969; Alme and Wilson, 1973, for earlier works).. The structure of the atmosphere is obtained by solving the hydrostatic equilibrium equation

$$\frac{\mathrm{d}P}{\mathrm{d}y} = \frac{GM}{y_G^2 R^2}, \tag{5.11}$$

where G is the gravitational constant, M is the mass of the star and $P = k\rho T/\mu_e m_p$ is the gas pressure, with T the gas temperature. Equation (5.11) can be solved analytically, giving the density as a function of the column density

$$\rho = \frac{GMm_p}{2y_G^2 R^2}\frac{y}{kT(y)}\,. \tag{5.12}$$

For typical luminosities of magnetar sources, $L = 10^{34} - 10^{36}$ erg s^{-1}, both the ram pressure by the particle bombardment and the radiative force are negligible with respect to the thermal pressure and the gravitational force, respectively.

The differential equation for the total luminosity is given by (Zampieri et al., 1995)

$$\frac{1}{4\pi R^2}\frac{\mathrm{d}L}{\mathrm{d}y} = -\frac{W_H}{y_G}, \tag{5.13}$$

which can be combined with equation (5.8) to derive an analytical solution for the luminosity,

$$L(y) = \begin{cases} \dfrac{L_\infty}{y_G}\dfrac{y_0 - y}{y_0} & y < y_0 \\ 0 & y \geqslant y_0 \end{cases} \tag{5.14}$$

In a magnetised plasma, the polarised radiative transfer problem can be described by a system of two coupled differential equations for the specific intensities of ordinary and extraordinary photons (see Chapter §1). In the Eddington and plane-parallel approximation, the first and second moments of the radiative transfer equations can be written in terms of the luminosity, L_i, and radiation energy density, U_i, of each normal mode (with $i = 1, 2$), both measured by the local observer, as

$$\frac{1}{4\pi cR^2}\frac{\mathrm{d}L_i}{\mathrm{d}y} = \kappa_i^P\left(\frac{aT^4}{2} - U_i\right) + \bar{S}(U_{3-i} - U_i), \tag{5.15}$$

$$\frac{1}{3}\frac{\mathrm{d}U_i}{\mathrm{d}y} = \kappa_i^R\frac{L_i}{4\pi R^2 c y_G}, \tag{5.16}$$

where $\bar{S}$ is the scattering mean opacity from one normal mode to the other

$$\bar{S} = \int\int \kappa_{12}^s(\mu\prime, \mu)\mathrm{d}\mu\prime\mathrm{d}\mu\,, \tag{5.17}$$

κ_i^P is the Planck mean opacity of mode i

$$\kappa_i^P = \frac{\int \bar{\kappa}_i^a B_\nu \mathrm{d}\nu}{\int B_\nu \mathrm{d}\nu}, \tag{5.18}$$

and

$$\frac{1}{\kappa_i^R} = \frac{\int \frac{\mathrm{d}B}{\mathrm{d}T}\mathrm{d}\nu \int \frac{1}{\kappa_i^s + \kappa_i^a}\mathrm{d}\mu}{\frac{3}{2}\int \frac{\mathrm{d}B}{\mathrm{d}T}\mathrm{d}\nu} \tag{5.19}$$

defines the Rosseland mean opacity κ_i^R for mode i. Here $\bar{\kappa}_i^a$ is the angle averaged free-free absorption opacity, κ_i^s is the total scattering opacity averaged over all the scattered photon directions, and $\kappa_{12}^s = \kappa_{21}^s$ is the scattering opacity from one mode to the other (see all details in Chapter §1). Note that, in the previous expressions, in absence of a complete frequency-dependent calculation (which is outside the purpose of this investigation), the absorption mean opacity and the flux mean opacity have been approximated by κ_i^P and κ_i^R, respectively, for each mode of propagation (see Section §5.2.3 for details about their numerical evaluation). This is a standard procedure, but it also means that the approximation for the opacities holds better in the internal atmospheric layers, where thermal equilibrium is reached.

In the following, collective plasma effects are neglected, considering only the limit $\omega_p^2/\omega^2 \ll 1$, where ω_p is the plasma frequency. I also considered only frequencies lower than the electron cyclotron frequency, so the semitransverse approximation can be assumed to hold. With the exclusion of the very external layers, the temperature in the atmosphere is always lower than $\sim 10^7$ K, so that scattering dominates over true absorption only for $\tau \sim 1$ and Comptonisation is negligible. For this reason, only conservative scattering is accounted for in the transfer equations. The plasma is assumed to be composed of protons and electrons, accounting for vacuum corrections in the polarisation eigenmodes, that start to be important when the magnetic field approaches the quantum critical limit, $\sim B_q$. These corrections induce the breakdown of the normal mode approximation at the mode collapse points (MCPs), where the two normal modes can cross each other or have a close

approach, depending on the photon propagation angle (see Section §5.2.3).

Despite Comptonisation is expected to be negligible as far as the radiative transfer equations are concerned (see Section §5.2.3), in analogy to the case of accreting atmospheres, it is expected to have an important role in establishing the correct energy balance in the external, optically thin layers (Alme and Wilson, 1973; Turolla et al., 1994; Zampieri et al., 1995; Zane et al., 2000) where the heating deposited by the incoming charges needs to be balanced by Compton cooling. Accordingly, the energy balance equation is written as

$$\frac{\kappa^P}{\kappa_s}\left(\frac{aT^4}{2}-\frac{\kappa_1^P}{\kappa^P}U_1-\frac{\kappa_2^P}{\kappa^P}U_2\right)+(\Gamma-\Lambda)_c=\frac{W_H}{c\kappa_s} \tag{5.20}$$

where $(\Gamma-\Lambda)_c$ is the Compton heating-cooling term, evaluated using the approximation of Arons et al. (1987), κ^s is the total (summed over the two modes) scattering opacity and $\kappa^P=\kappa_1^P+\kappa_2^P$ is the total Planck mean opacity. One complication is that the Compton heating-cooling term in equation (5.20) depends on the radiation temperature, T_γ, which in turn could be obtained by solving the frequency-dependent transport of radiation. To overcome this problem, it is assumed that the energy exchange between photons and the gas particles, due to multiple Compton scatterings, is governed by the equation (Wandel et al., 1984; Park and Ostriker, 1989; Park, 1990; Turolla et al., 1994; Zampieri et al., 1995)

$$\frac{y}{T_\gamma}\frac{\mathrm{d}T_\gamma}{\mathrm{d}y}=2Y_c\left(\frac{T_\gamma}{T}-1\right), \tag{5.21}$$

where $Y_c = (4kT/m_ec^2)\max(\tau_{\rm es},\tau_{\rm es}^2)$ is the Comptonisation parameter and $\tau_{es} = \kappa_s y$ is the unmagnetised Thomson scattering optical depth.

The system of differential equations given by equation 5.15 (solved for mode 1 only, since the luminosity of mode 2 can then be obtained by difference using equation 5.14 for the total luminosity), equation 5.16 (solved for both modes) and equation 5.21 needs to be solved coupled to a set of 4 boundary conditions. First, a non-illuminated atmosphere is assumed, which translates into a free streaming condition relating the total energy density of the radiation to the total luminosity, at

the outer layer of the atmosphere,

$$U(y_{min}) = U_1(y_{min}) + U_2(y_{min}) = \frac{L_1^{\infty} + L_2^{\infty}}{2\pi R^2 c y_G},$$

where y_{min} corresponds to the minimum value of the column density grid used in the atmosphere model. Second, energy equipartition is assumed in the inner, optically thick, atmospheric region, where the energy density of each mode approaches $\sim aT^4/2$, and we set $U_1(y_{max}) = U_2(y_{max})$, where y_{max} is the maximum value of the column density grid used in the model calculation. Furthermore, photons are assumed to be in thermodynamic equilibrium with the gas in the inner layers of the atmosphere, therefore the radiation temperature must be equal to the gas temperature, $T_\gamma(y_{max}) = T(y_{max})$. Finally, since the observed luminosity is produced by re-irradiation of the the heat deposited by particle bombardment, with $W_H = 0$ for $y > y_0$, the condition $L_1(y > y_0) = L_2(y > y_0) = 0$ is used in the inner regions of the atmosphere.

5.2.3 Vacuum resonance and opacities

A strong magnetic field can give rise to three MCPs for the electromagnetic waves propagating in a plasma plus vacuum system (all of them within the energy range of the thermal spectrum of magnetars): two vacuum resonances and one further MCP near the proton cyclotron frequency (Mészáros, 1992; Zane et al., 2000). At these MCPs the normal mode approximation, i.e., the assumption of transverse electromagnetic waves, linearly polarised in the O- or X-mode, is not longer valid. Formally, the treatment of the transport of radiation considering the effects of the MCPs need to be solved via the evolution of the Stokes parameters.

In particular, at the vacuum resonance MCPs, a mode conversion from one to another mode may occur (Gnedin et al., 1978; Pavlov and Shibanov, 1979; Meszaros and Ventura, 1979). The location of the vacuum resonance MCPs depends on the density and photon frequency. Therefore, a linearly polarised electromagnetic wave propagating in the atmosphere (and thus propagating across a density-gradient) can encounter a vacuum resonance at which it becomes circularly

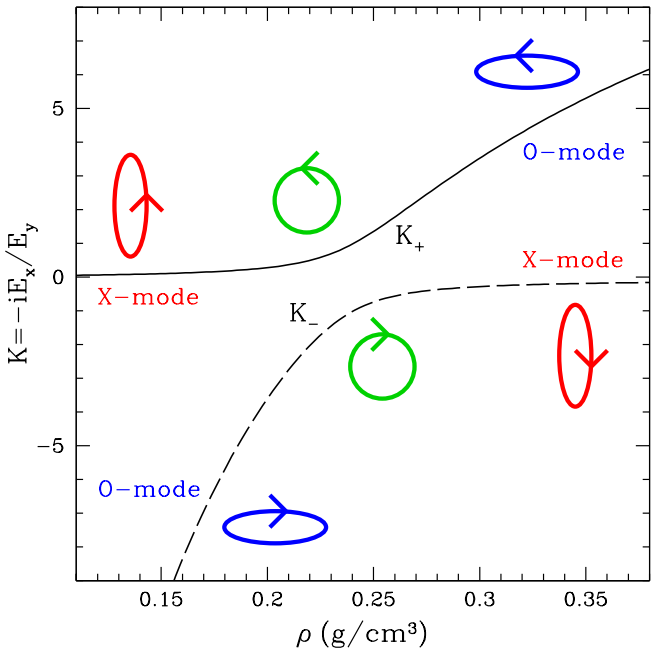

Figure 5.3: Mode evolution (ellipticity K) across the vacuum resonance in a H atmosphere for for a NS with $B = 10^{13}$ G. The electromagnetic wave is at energy $E = 5$ keV and photon propagation direction $\theta = 45°$ (Harding and Lai, 2006).

polarised (see Figure 5.3). If the density gradient across the MCP is gentle enough, then the electromagnetic wave may undergo an "adiabatic" conversion (Ho et al., 2003a) from the X-mode to the O-mode (and viceversa). Since the opacities depend on the polarisation vector (Chapter §1), mode conversion can strongly affect the level of opacity exerted on the wave.

In the following, I include mode conversion in the opacities at the vacuum resonance MCPs, but no mode conversion is assumed at the proton cyclotron MCP. The mode conversion at the vacuum resonance MCPs is accounted for following the formalism of Pavlov and Shibanov (1979) and Gnedin et al. (1978) (see also Zane et al. 2000), in which the vacuum parameter is given by

$$W = \left(\frac{3\times10^{28}\mathrm{cm}^{-3}}{n_e}\right)\left(\frac{B}{B_q}\right)^4 \tag{5.22}$$

where n_e is the electron number density. The ellipticities of the normal modes for electromagnetic waves in the magnetised plasma can be obtained from Kaminker

et al. (1982)

$$\beta = \frac{\sin^2\theta}{2\cos\theta}\sqrt{u}\left(1 - W\frac{u-1}{u^2}\right), \tag{5.23}$$

where $u = \omega_{c,e}^2/\omega^2$, $\omega_{c,e} = eB/m_e c$ is the electron cyclotron frequency and θ is the angle between the wave propagation direction and the magnetic field. The normal modes, then, can be obtained by replacing this β term in equation 1.11 of Chapter §1. As already mentioned, the effects of the plasma frequency are neglected.

The condition $\beta = 0$ determines the frequencies and photon directions (for each value of density and magnetic field) at which the normal modes approximation breaks downs (due to vacuum corrections and proton resonance). As mentioned above, at these MCPs a proper treatment of radiative transfer should be performed via the Stokes parameters, while the transport equations used in this work are written assuming that the normal mode approximation holds for all photon propagation directions. Following Pavlov and Shibanov (1979), the critical angle of photon propagation associated to the normal modes breakdown at the vacuum MCP is obtained from the expression

$$\frac{\cos\theta_n}{\sin^2\theta_n} = \pm\frac{1}{2\sqrt{u}}\left[\gamma_{\parallel}(u-1) + \gamma_{\perp}\left(1 - \frac{2W}{u}\right)\right]_{\beta=0}, \tag{5.24}$$

where $\gamma_{\parallel,\perp} = (\nu_{\parallel,\perp} + \nu_r)/\omega \sim 10^{-5} - 10^{-3}$. Here, ν_r is a radiative width and $\nu_{\parallel,\perp}$ is an effective electron-ion collision frequency (for details see Pavlov and Shibanov 1979). At θ_n the normal modes have maximum non-orthogonality (i.e. maximum coincidence). If $\theta_n \to \pi/2$, the interval of non-orthogonality collapses to a point and, for almost all waves (i.e. all those with $\alpha = |\pi/2 - \theta| > \alpha_n = |\pi/2 - \theta_n|$), the polarisation ellipses are rotated through 90° while crossing the resonance (mode switching). Vice versa, if θ_n is small the evolution of the electromagnetic waves across the resonance is not well understood. In the numerical simulation, complete mode conversion at the vacuum resonance is set as long as the condition $\theta_n > 50°$ is satisfied.

As an example, Figure 5.4 shows the energy dependent free-free absorption and the mode exchange scattering opacity used in the calculations. In general, for

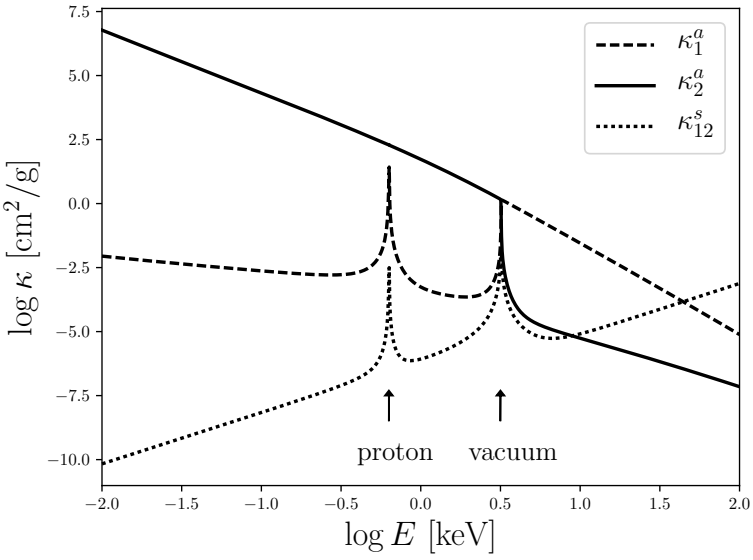

Figure 5.4: Angle integrated opacities for a fully ionised H atmosphere with magnetic field $B = 10^{14}$ G (normal to the surface), temperature $T = 10^7$ K and density $\rho = 10$ g cm^{-3}. The dashed and solid lines correspond to the free-free absorption opacities in mode 1 (X-mode) and mode 2 (0-mode), respectively. The dotted line corresponds to the scattering opacity from mode 1 to mode 2. Notice that due to opacity symmetry $\kappa_{12}^s = \kappa_{21}^s$. The arrows indicate the proton and vacuum resonances (González-Caniulef et al., 2019).

most energies, opacities are dominated by photon-electron interaction. However, for the magnetic fields considered, $B \sim 10^{14}$ G, protons also play an important role as they produce a sharp feature in the X-mode opacities at the proton cyclotron energy, which lies within the soft X-ray band (see Zane et al. 2001, Ho and Lai 2001 and Özel 2003 for the discussion of the impact of this feature in the emergent spectrum from atmospheres of magnetised NSs). On the other hand, vacuum effects introduce additional features to the opacity profiles. In fact, when complete mode conversion is present, vacuum effects produce a step change in the free-free opacities across the vacuum resonance, due to the exchange of the X-mode opacity with the O-mode opacity (and vice versa; see Ho and Lai 2003 for a discussion of the vacuum resonance with and without mode conversion). Instead, vacuum effects produce a raise (spike feature) in the (angle-integrated) mode exchange scattering opacity at the vacuum resonance.

As mentioned in Section §5.2.2, the above opacities are suitably integrated in

frequency in strict analogy with the definition of the Planck mean opacity and the Rosseland mean opacity in the unmagnetised case (see equations 5.18 and 5.19). A further problem encountered while performing the integration in energy is related to the fact that the vacuum resonance is located at different energies in different layers of the atmosphere (because of the density gradient). To avoid overestimating the mean opacity due to the finite size of the energy grid, which can lead to numerical problems of convergence in the calculations, the opacity near the vacuum resonance feature at the energy point E_v is obtained as an average between its values at two adjacent energies $E_- = E_v - \Delta E_{bin}/3$ and $E_+ = E_v + \Delta E_{bin}/3$. Numerical tests show that varying the way in which the adjacent energies are chosen produces negligible differences in the resulting integral.

5.3 Numerical solutions

The numerical calculation was performed by readapting the code presented by Turolla et al. (1994), which was meant for unmagnetized atmospheres under accretion, to the case of magnetized NS atmospheres heated by particle bombardment. I started from the numerical routines for the opacities from Zane et al. (2000) and created all necessary routines for the computation of the energy integrated opacities required by this work. Solutions are then found using a numerical iterative scheme. First, an initial temperature profile is specified, taking as trial solution the temperature profile of a non-magnetised atmosphere from Turolla et al. (1994). This, together with equation (5.12) sets also the initial density profile. Then, the transport of radiation is solved via equations (5.15), (5.16) and (5.21) to obtain the profiles for L_i, U_i and T_γ. These, in turn, are used to compute a new temperature profile, that satisfies the energy balance, equation (5.20). The procedure is iterated until the fractional difference between two successive solutions is $< 10^{-5}$, in each variable. Convergence is typically reached after ~ 15 iterations.

In all models, a NS with mass $M = 1M_\odot$ and radius $R = 10$ km is assumed. Solutions are computed by using a logarithmic grid of 100 equally spaced points for the column density y in the range $[10^{-5} - 10^2]$ g cm^{-2}. Numerical solutions are

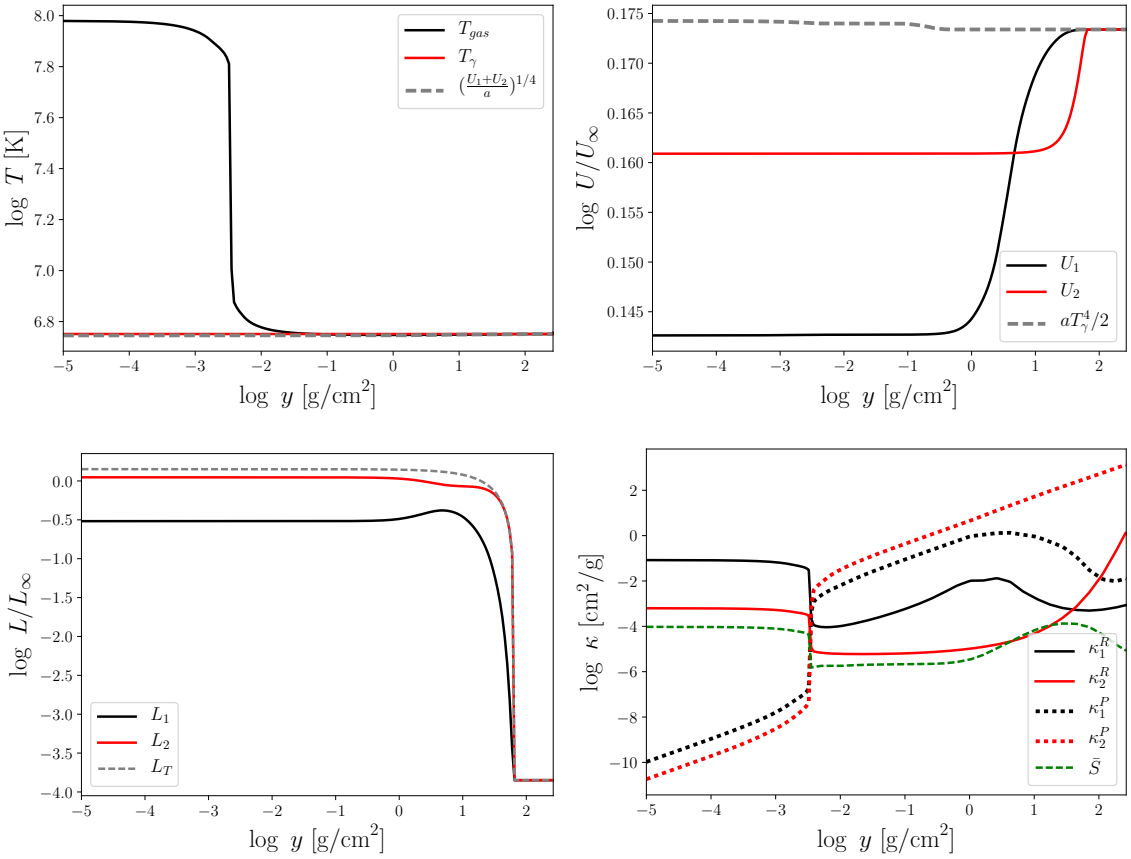

Figure 5.5: grey atmosphere solution for total luminosity $L_\infty = 10^{36}$ erg/s, stopping column density $y_0 = 65$ g/cm^2 and magnetic field $B = 10^{14}$ G. **Top-left panel**: gas temperature profile, T (black solid line), and photon temperature profile, T_γ (red solid line). The temperature associated to the total energy density is shown in the grey dashed line. **Top-right panel**: energy densities associated to U_1 (black solid line), U_2 (red solid line) and T_γ (dashed grey line) normalised to $U_\infty = L_\infty/4\pi R^2 c$. **Bottom-left panel**: luminosity profiles L_1 (black solid line) and L_2 (red solid line). The total (analytical) luminosity L_T is shown in the grey dashed line. **Bottom-right panel**: Planck mean opacities, κ_1^P (black dotted line) and κ_2^P (red dotted line), and Rosseland mean opacities, κ_1^R (black solid line) and κ_2^R (red solid line). The scattering mean opacity from mode 1 to mode 2 (and vice versa), $\bar{S}$, is shown in the green dashed line (González-Caniulef et al., 2019).

reported for magnetic field values $B \approx 10^{14} - 10^{15}$ G and luminosities $L_\infty \approx 10^{35} - 10^{36}$ erg s^{-1}, which are characteristics of the brightest magnetars, and stopping lengths in the range $y_0 = 65 - 500$ g cm^{-2} (see Section §5.2.1).

5.3.1 Results

Figure 5.5 shows the temperature, energy density, luminosity and opacity profiles for a NS atmosphere with $B = 10^{14}$ G, stopping length $y_0 = 65$ g cm^{-2} and total luminosity $L_\infty = 10^{36}$ erg s^{-1}. The temperature profile (top-left panel) shows the formation of a hot layer in the most external part of the atmosphere. This external temperature profile is similar to those obtained in the case of atmospheres of NSs accreting at low rate from the interstellar medium (see Turolla et al. 1994 and Zane et al. 2000). As discussed in previous works, free-free cooling is not effective in balancing the heating (in this case caused by the particle bombardment) in this region. As a consequence, the plasma temperature raises until a point in which Compton cooling becomes efficient (see Zane et al. 2000 and references therein). Since the radiation is produced only by the particle bombardment (or, alternatively, the luminosity by particle bombardment is much larger than the NS cooling luminosity), in the deepest layers the luminosity vanishes and the temperature profile becomes constant. The radiation temperature shows that most of the radiation decouples from the plasma in the internal region of the atmosphere, before photons start travelling across the hot external layer.

The top-right and bottom-left panels of Figure 5.5 show the energy density and the luminosity of the two modes. Clearly, U_i is constant in the internal layers where the luminosity vanishes and energy equipartition is reached between the two radiation modes. As matter and radiation start decoupling, most of the luminosity is produced in an internal region, characterised by a substantial and non vanishing radiation energy density gradient, $\mathrm{d}U_i/\mathrm{d}y$, in which diffusion approximation holds. It is interesting to notice how the energy density profiles cross, at some point within the atmosphere, reflecting the mode conversion due to vacuum effects (Figure 5.5, bottom-right panel). This is an interesting effect since it can impact on the expectations for the polarisation signal. In fact, since the plasma is highly magnetised, the emerging radiation is expected to be highly polarised, in principle even up to 100%: the large difference in the plasma opacities of the two modes implies that most of the radiation should be carried by the mode for which the atmosphere is

more transparent (see for example Özel 2001 and Ho and Lai 2003 for a discussion in the context of atmosphere for passively cooling NSs). However, I found that vacuum mode conversion partly reduces the difference in the opacities, and therefore in luminosity, of the two modes, potentially reducing the polarisation signal. If an "intrinsic" polarisation fraction is defined as $PF = (L_{\infty,1} - L_{\infty,2})/(L_{\infty,1} + L_{\infty,2})$, then $PF \approx 0.6$ in the model at hand.

In the following, the numerical solutions are explored for different values of luminosity, stopping length and magnetic field. In order to isolate the effects of each parameter, I vary one of these quantities at each time, keeping fixed the other model parameters. I present the profiles for temperature, luminosity, absorption and Rosseland mean opacities as they are the most relevant to discuss the behaviour or the solution (the scattering opacity is in fact negligible in most of the atmosphere).

5.3.1.1 Models with different luminosity

Figure 5.6 shows a set of solutions computed for $y_0 = 100$ g cm^{-2}, $B = 3 \times 10^{14}$ G, and by varying the total luminosity in the range $L_\infty = 10^{35} - 10^{36}$ erg s^{-1}. As expected, higher luminosities, which are related to larger energy deposition in the atmosphere, correspond to hotter atmospheres. Moreover, by increasing the luminosity, the hot atmospheric layer extends inwards, to higher column densities. Luminosity and temperature profiles scaled in a roughly self–similar way. However, the expected emergent polarisation increases for higher luminosities. This can be understood noticing that, in the inner regions where most of the luminosity is produced, the difference between the Rosseland mean opacities associated to each normal mode (lower right panel), is larger for higher luminosities. In diffusion approximation, this translates in a larger suppression of the radiation carried by a mode with respect to the other. The difference in luminosity, then, propagates until the top of the atmosphere. For the models presented here, the resulting emergent polarisation varies between $0.4 < PF < 0.9$ for the range of luminosities L_∞ considered.

The behaviour for the opacities in these models can be understood as follows. The Planck mean opacity, κ_i^P, is obtained by performing an integration over energies

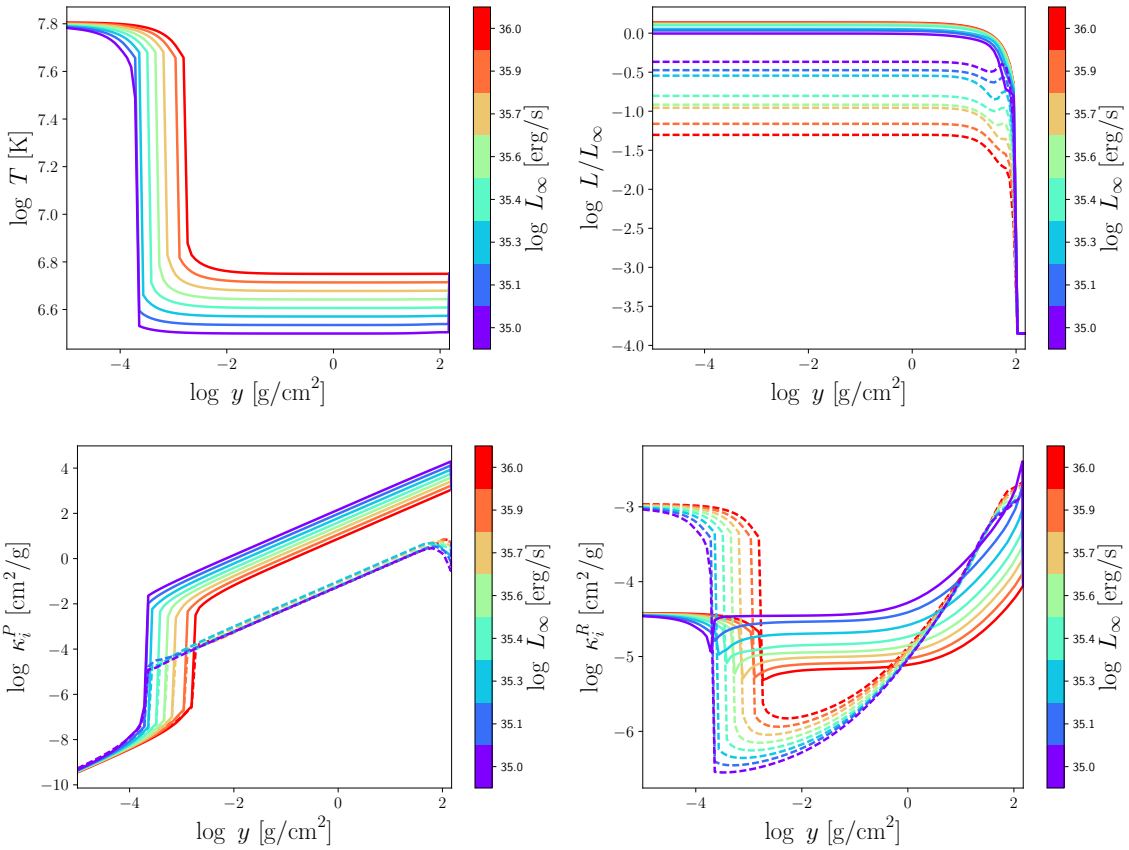

Figure 5.6: grey atmosphere solutions for different luminosities (see vertical color bar), fixed magnetic field $B = 3 \times 10^{14}$ G, and fixed stopping column density $y_0 = 100$ g cm^{-2}. The temperature profile for the atmospheric plasma is shown in the top-left panel. The luminosity L_1 (top-right panel), Planck mean opacity κ_1^P (bottom-left panel), and Rosseland mean opacity κ_1^R (bottom right panel) are shown by dashed lines. Similarly, the corresponding profiles for L_2, κ_2^P, and κ_2^R are shown by solid lines (González-Caniulef et al., 2019).

of the free-free absorption opacity weighted by a blackbody. In turn, the integrand over energy is dominated by the contribution of the free-free opacities at relatively low energies, which are less sensitive to the presence of the vacuum resonance and subsequent mode switching. It follows that, for a fixed magnetic field, the integrand in the opacity scales approximatively as $\kappa_i^{\rm ff} \propto yT^{-7/2} f_i(E)$, where $f_i(E)$ is a function of the energy. Since most of the atmosphere has a uniform temperature, this translates into a Planck mean opacity with a linear dependency on y. In the external hot layer the temperature increases, and this produces the observed drop in the Planck mean opacities according to the $T^{-7/2}$ dependency of the free-free

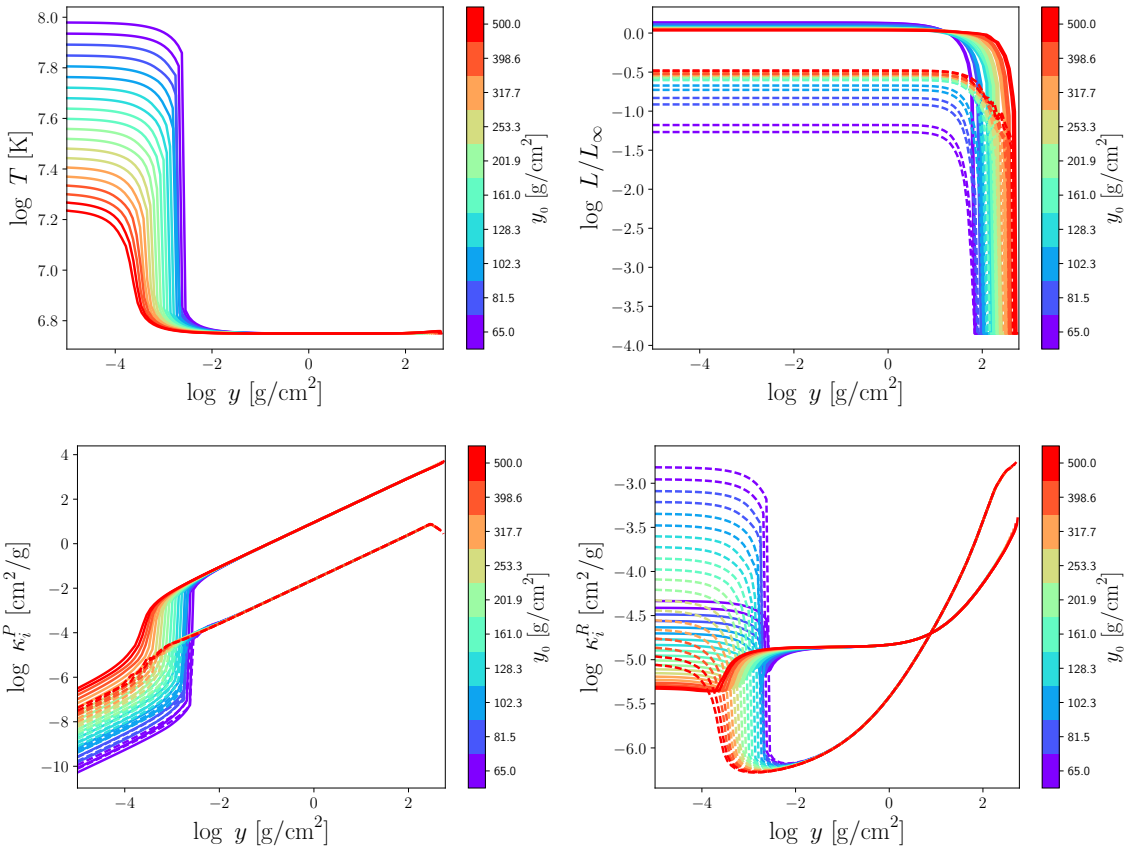

Figure 5.7: Same as Figure 5.6, but varying the stopping column density y_0. Here, the total luminosity is set to $L_\infty = 10^{36}$ erg/s and the magnetic field to $B = 4 \times 10^{14}$ G (González-Caniulef et al., 2019).

opacity.

The Rosseland mean opacities, instead, are computed considering the contribution of both, the free-free and scattering opacities. In particular, scattering opacities are dominant at low densities, which is reflected on fact that, in the most external atmospheric layers, the Rosseland mean opacity tends toward a constant. Instead, the free-free opacity is dominant at high densities. Moreover, since in the Rosseland mean opacity the associated integration is performed over the inverse of the energy-dependent opacity, the major contribution from free-free opacities is from the higher energies which are more sensitive to the vacuum resonance. This in turn introduces an additional density dependency, which is reflected in the non linear growth of the Rosseland means at large y.

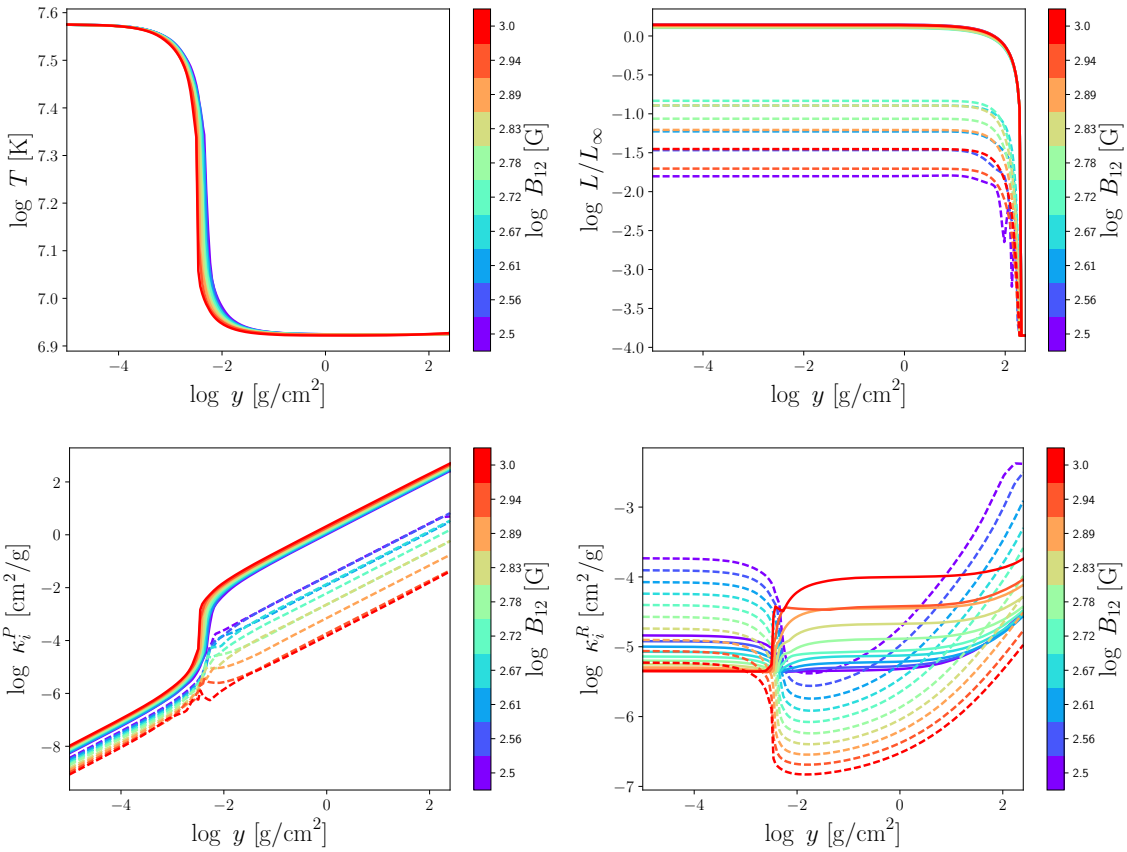

Figure 5.8: Same as Figure 5.6, but varying the magnetic field. Here, the total luminosity is set to $L_\infty = 5 \times 10^{36}$ erg/s and the stopping column density to $y_0 = 200$ g/cm^2 (González-Caniulef et al., 2019).

5.3.1.2 Models with different stopping column density

Figure 5.7 shows the solutions for stopping column densities in the range $y_0 = 50 - 500$ g cm^{-2}, total luminosity $L_\infty = 10^{36}$ erg s^{-1}, and magnetic field $B = 4 \times 10^{14}$ G. At variance with the models in Section §5.3.1.1, the stopping column density y_0 is anticorrelated with temperature of the hot external layer. Indeed, for smaller stopping column densities, the energy deposition is distributed in a smaller region (see equation 5.2.1), which leads to external layers with higher temperatures, as shown in the top-left panel. In this case, the hot layer moves inwards as y_0 decreases. In addition, the most internal layers of the atmosphere have the same temperature for different y_0. This is interesting for future frequency-dependent calculations since it indicates that the typical photon energy deep in the atmosphere is quite insensitive to variations of y_0. Therefore, the spectrum produced in the atmosphere interior may

be determined only by the total luminosity and magnetic field strength.

The luminosity carried by each normal mode is shown in the right upper panel of Figure 5.7. Similar to the solutions for the temperature profile, the polarisation is also anticorrelated with the stopping column density. At variance with models presented in Section §5.3.1.1, the region where a significant difference in the Rosseland mean opacities of the two modes, κ_1^R and κ_2^R, leads to a larger polarisation, is now located in the most external layers of the atmosphere.

As shown on the left top panel, for the models presented in this section the only change between the solutions is in the temperature (and location) of the external hot layer, while the density profile and the magnetic field are the same for the different models. Accordingly, the strong dependency on $T^{-7/2}$ of the free-free absorption introduces the drop and dispersion between the various curves of the Planck mean opacities seen in the most external atmospheric layers.

The corresponding dispersion in the values of the Rosseland mean opacities at low y (scattering dominated) is instead due to the fact that they are evaluated by convolving the energy-dependent opacity over the derivative of the blackbody, $\mathrm{d}B_E(T)/\mathrm{d}T$, calculated at the local value of T. For higher temperatures, the peak of this function is located at higher energies. In other words, if the photon bath in the external layer is hotter, then the major contribution to the averaged Rosseland opacity is due to scattering of photons with higher frequency (which in turn may also be more largely affected by vacuum effects).

5.3.1.3 Models with different magnetic field

Figure 5.8 shows the solutions for magnetic fields in the range $B = 3 \times 10^{14} - 10^{15}$ G, stopping column density $y_0 = 200$ g cm^{-2}, and total luminosity $L = 5 \times 10^{36}$ erg cm^{-3}. As shown in the top-left panel, by varying the magnetic field, and thus the opacities, no significant changes are produced in the temperature profile. Therefore, this suggests that the temperature profile is, instead, determined just by the total luminosity and stopping column density, as discussed in the previous section (Section §5.3.1.2).

The right lower panel shows how the variation of the magnetic fields introduces

significant differences in the Rosseland mean opacities κ_1^R and κ_2^R. However, for these opacities, the polarisation does not change monotonically with the magnetic field. Instead, the polarisation increases as the solutions approach to both the lower and upper end range of the magnetic field considered.

The behaviour of the mean opacities is now much more complicated. By increasing the magnetic field, the X-mode opacities decrease because of the X-mode-reduction factor $\sim 1/(\omega_{c,e}^2\omega)$ and $\sim (\omega/\omega_{c,e})^2$ present in the free-free and scattering opacities, respectively. However, it should be noticed that by varying the magnetic field also changes the energy associated to the mode switch at the vacuum resonance and its location in the atmosphere. This effect is responsible for **a)** the fact that the curves of the various Planck mean opacities become closer to each other in the external atmospheric layers and **b)** the different location of the crossing points of the Rosseland mean opacities (for the two modes) in different models.

5.3.1.4 Models with different magnetic field and different stopping length

It is interesting to test a scenario in which, as expected, the stopping column density depends on the magnetic field. By performing a linear fit in logarithmic scale to the stopping column densities discussed in Section §5.2.1, that describes the deceleration of fast magnetospheric particles with Lorentz factor $\gamma = 10^3$, I found that this dependency is fairly compatible with the law $\log y_0 = -8.7 + 0.75 \log B$ (in cgs units). It is important to notice that the length scale at which the pair cascade propagates (produced from X-mode photons) is, for these values of parameters, roughly independent on whether the bombarding charge is stopped by a Magneto-Coulomb interaction or by Compton drag. The models are run for a total luminosity $L_\infty = 5 \times 10^{36}$ erg s^{-1}, a value that is more convenient to ensure numerical convergence. In addition, it is also numerically convenient to solve the transport of radiation for the luminosity in mode 2 (see equation 5.14). For doing that, the modes in the Rosseland and absorption mean opacities are exchanged as $\kappa_i^R \rightarrow \kappa_{3-i}^R$ and $\kappa_i^a \rightarrow \kappa_{3-i}^a$ (with $i = 1,2$), respectively, in the numerical routines that perform their calculations. Notice that there is no need to perform this operation in the mode

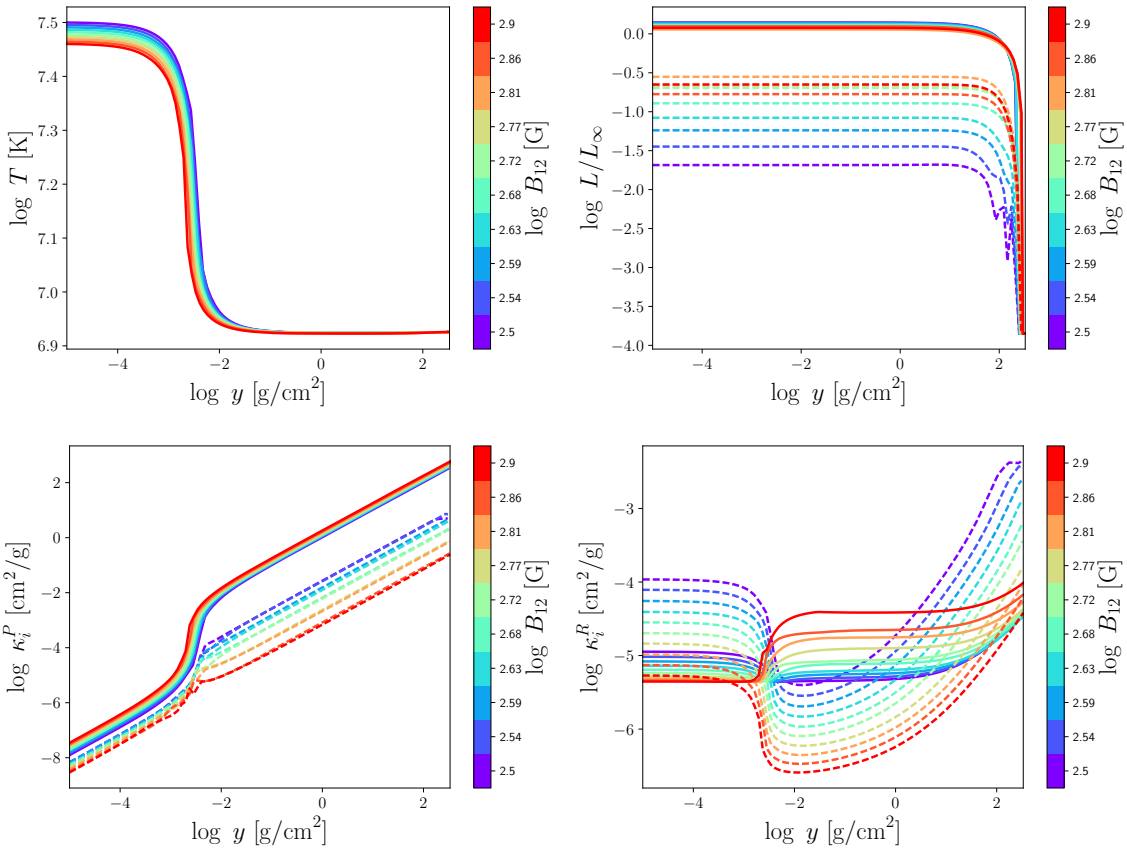

Figure 5.9: Same as Figure 5.6, but varying the magnetic field (vertical color bar) and the stopping column density (see Section §5.3.1.4 for details). Here, the total luminosity is set to $L_\infty = 5 \times 10^{36}$ erg/s (González-Caniulef et al., 2019).

exchange scattering opacity as $\kappa_{12} = \kappa_{21}$.

Figure 5.9, top-left panel, shows the solution for the temperature profile. Since lower magnetic fields produce smaller stopping column densities, consequently, the temperature of the external layer increases for lower magnetic fields (as in the results discussed in Section §5.3.1.2). I also found that, by varying the luminosity this trend, qualitatively, still holds (although no quantitative solutions are shown, since, at column densities just below $\sim y_0$, numerical oscillations start to grow in the region with steep luminosity gradient).

The solutions for the luminosities in each normal mode, top-right panel, show that the polarisation decreases almost monotonically with the magnetic field (except at the upper end of the magnetic field range). This is at variance with the results shown in Section §5.3.1.3, and it shows that the polarised signal is affected more

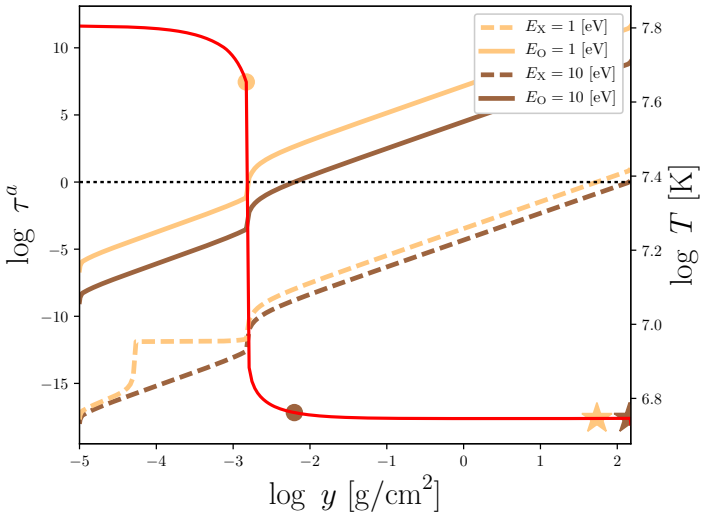

Figure 5.10: Optical depth as a function of column density for photons in the optical ($E = 1$ eV) and ultraviolet band ($E = 10$ eV). The model is computed for $L_\infty = 10^{36}$ erg/s, $y_0 = 100$ g/cm^2 and $B = 4 \times 10^{14}$ G. Solid and dashed lines correspond to O-mode and X-mode photons, respectively. The temperature profile is shown by the red solid line (the temperature scale is on the right-hand side). The yellow (brown) circle and yellow (brown) star show the location of the radiation-atmosphere decoupling, $\tau \sim 1$, for O-mode and X-mode photons in the optical (soft X-ray) band, respectively (González-Caniulef et al., 2019).

strongly by the magnetic field effects on the stopping column density rather than those on the opacities.

5.3.1.5 Spectral expectations

Some information about the spectral properties of the emerging radiation can be obtained even from this grey model, by looking at the depth at which photons of different energies decouple. In particular, I compute the energy dependent optical depth (for optical and soft X-rays photons) as

$$\tau_E^i = \int_{y_{min}}^{y} \kappa_E^{a,i} \mathrm{d}y\prime , \tag{5.25}$$

where $\kappa_E^{a,i}$ (with $i = 1, 2$) is the energy dependent, angle integrated absorption opacity (using $\tau_E^i = 0$ at $y = y_{min}$).

Figure 5.10 shows the location of the photon decoupling for the two normal modes. In particular, the O-mode photons with energy $E = 1$ eV, i.e. in the optical

band, decouple in the region of the hot layer. This suggests that the spectrum in the optical, and potentially also in the infrared, may have a flux excess due to the radiation from this hot layer. Instead, X-mode photons with energy $E = 10$ eV (in the ultraviolet band), as well as photons with higher energies (in both normal modes) decouple deeper in the atmosphere. These photons are produced in regions with lower and nearly uniform temperature, and so their spectrum may be potentially described by a single black body. These results suggest that the spectrum from a magnetised atmosphere heated by a particle bombardment (single black body with optical/infrared excess), may show substantial deviations from those produced by passively cooling NSs (spectrum harder than a blackbody). Models accounting for the full frequency transport of radiation are definitely required to assess this issue and will be the focus of my future work.

5.4 Summary and conclusions

In this chapter, I presented numerical models for grey atmospheres of magnetised NSs heated by particle bombardment. A pure, fully ionised hydrogen composition is assumed, accounting for the polarised transport of radiation induced by the strong magnetic field. The main results can be summarised as follows.

- A hot layer is created in the most external region of the atmosphere ($T \sim 10^8$ K), similar to what has been found in previous studies of atmospheres heated by accretion (Turolla et al., 1994; Zane et al., 2000). I found that, in the case presented here, the spatial extent of the layer is primary determined by the luminosity and the stopping column density for the particle bombardment. If there is no significant contribution from the NS cooling (i.e. the luminosity vanishes in the internal layer, as assumed here) then the internal regions of the atmosphere are characterised by a lower (below $T \sim 10^7$ K), uniform temperature that is primary determined by the total model luminosity.

- As a consequence, it is expected that in the range of frequencies that decouple in the deeper atmospheric layers (i.e. above ~ 1 keV) the emergent spectrum may be well approximated by a single blackbody. Instead, photons that de-

couple in the hot layer (below ~ 1 eV) may produce an optical/infrared flux excess, significantly above the extrapolation of the blackbody spectrum coming from the atmosphere interior (see Zane et al. 2000 for similar discussions).

- The expected degree of linear polarisation in the emergent spectrum is correlated with the luminosity and anticorrelated with the stopping column density (and almost similarly with the magnetic field, see text for details). Depending on these parameters, the expected intrinsic linear polarisation, defined here as $PF = (L_2 - L_1)/(L_2 + L_1)$, for a single patch in the atmosphere, may vary between $0.4 < PF < 0.9$.

- Therefore, variations in the intrinsic polarisation may be present in the thermal emission from transient magnetar, as the luminosity in these sources can decrease by orders of magnitude.

These results have been obtained under a number of assumptions and simplifications. A major simplification is the assumption of pure H and fully ionised atmosphere. Strong magnetic fields, $B = 10^{14} - 10^{15}$ G, increase significantly the binding energy of the atoms, and this can lead to additional contributions to the opacities. From Figure 3 of Potekhin and Chabrier (2004), it is possible to infer that, for the parameters typical of the models studied in my work, partial ionisation can be safely neglected in the most external (hot) layers of the atmosphere, where the atomic fraction should be much lower than 0.1%. Although for intermediate atmospheric layers the expected atomic fraction should be $\sim 0.1 - 1\%$, this may be still important as bound-bound and bound-free transitions (particularly in the energies range $E = 1 - 10$ keV) may change the opacities by orders of magnitude (see e.g. Figure 4 and 5 in Ho et al. 2003b). In addition, strong magnetic fields can also induce the formation of complex molecules. However, Potekhin et al. (2004) showed that the formation of those molecules can be suppressed for effective temperatures slightly above $T_{\rm eff} \sim 4 \times 10^5 (B/10^{14}\ {\rm G})^{1/4}$. Therefore this effect is not expected to be relevant in the range of T and B studied in this work.

Furthermore, vacuum polarisation and mode conversion induced by the strong

magnetic field can also produce substantial effect on the opacities. For example, Ho and Lai (2003) studied two simplified limiting cases: full mode conversion and no-mode conversion, showing that both cases can lead to large polarisation in the spectrum, i.e., almost $\sim 100\%$ in the soft X-ray band. However, as also pointed out by Ho and Lai (2003) the effect is not well understood yet and a realistic scenario may lie between the two limiting cases. In spite of the crude expression that I have used to estimate the polarisation degree, my work shows that intermediate cases for mode conversion can produce a much smaller (and luminosity-dependent) degree of polarisation. However, it should be also noticed that non-orthogonality of the normal modes may affect a substantial range of photon propagation directions at the vacuum MCP. In these cases, a proper calculation of the transport of radiation should be performed via the evolution of the Stokes parameters. The mode conversion effect basically tends to decrease the difference between the opacity of the two normal modes, and therefore the way in which this effect is treated affects critically the expected degree of polarisation. Further work on this important issue needs therefore to be carried on in order to produce more quantitative predictions. Future observations of magnetars with X-ray polarimeters (IXPE, Weisskopf et al. 2013; eXTP, Zhang et al. 2016) may provide crucial information in directing the theoretical effort.

Finally, the calculations of the stopping column density are also affected by additional uncertainties, and in particular I caveat that the cross section for magneto-Coulomb interaction, for photon splitting (either induced by the magnetic field or the Coulomb field of a nucleus) and the scattering cross sections that are commonly used in literature and that I used in this work are in principle valid for $B < 10^{14}$ G, i.e., below the range of field strengths I have considered.

This affects directly the calculation of the energy deposition in the atmospheric layer. To mitigate this, I have considered a large range of stopping column density values, $65 - 500$ g cm^{-2}. Notice that across the paper I have considered a representative value $\gamma = 10^3$ for the Lorentz factor of the (monoenergetic) bombarding electrons, but the problem of the determination of the spectrum of the impinging

charges is far from being understood. In principle this is a reasonable first guess if the Lorentz factor of the charges near the star surface is kept around the threshold for efficient resonant Compton drag to occur, since it is $\gamma \sim B/\Theta \sim 10^3$ for $B \sim 10^{14}$ G and $T \sim 1$ keV. However, the value of this Lorentz factor depends on the magnetic field and photon temperature at the surface, so it may vary considerably. If the Lorentz factor of the charges is as high as $\sim 10^6 - 10^7$, electrons are still efficiently stopped by magneto-Coulomb collisions (which length scale depends weakly on γ, see Eq. 2), but the resulting photon can be much more energetic and in turn the resulting pair cascade can penetrate much further, up to $\sim 700 - 1000$ g cm^{-2}.

In principle, the atmosphere may also modulate its penetration depth and atmospheric profile to ultrarelativistic electrons. The exploration of possible equilibrium solutions that account for the backreaction of the atmosphere would require to modify the scheme developed in this work and calculate (numerically) y_0 either assuming an approximated scaling with the temperature, as e.g. in Baring et al. (2011), or solving the full kinetic particle transport. This is, however, outside the scope of this first investigation. The results have shown that, when treating y_0 as a model parameter, the main effects of varying the stopping column length are actually restricted in the most external layers. Therefore, the conclusion regarding the creation of a blackbody like spectrum from the most internal atmospheric layers should hold, as it showed to be pretty much independent of the stopping column density.

Chapter 6

Conclusions

6.1 Thesis summary

In this thesis I studied the thermal emission from two classes of NSs: XDINSs and magnetars. While XDINSs are passive sources, magnetars are active sources with outburst activity in which their X-ray luminosity can change by orders of magnitude. Theoretical arguments and observational evidences point out that these sources may have strong magnetic fields, above $B \sim 10^{13}$ G. The study of the thermal emission and polarisation from XDINSs and magnetars can give us, thus, important information about the state of matter (at the star surface) and the vacuum (surrounding the NS) under strong magnetic fields.

First, I studied the polarisation properties of the thermal emission from XDINSs. These sources are characterised by their nearly pure thermal emission, non contaminated neither by a supernova remnant nor by magnetospheric activity. Although the thermal emission from NSs is generally expected to be reprocessed by an atmosphere, the strong magnetic field present in XDINSs, $B \sim 10^{13}$ G, may lead to phase transition, turning the gaseous atmosphere into a condensed metallic surface. Furthermore, the strong magnetic field may induce a QED vacuum birefringence, an effect for which there is not direct detection in terrestrial laboratories, yet.

In Chapter §2 I modelled the polarisation properties of XDINSs by considering the emission from a gaseous atmosphere or a condensed surface. The numerical

models were computed using a ray tracing method that allowed me to explore the polarisation properties for different viewing geometries. In the models I included the effects of vacuum birefringence by computing the polarisation properties at the adiabatic radius, i.e., a sharp region at a few NS radii ($\sim 10\ R_{\rm NS}$) in which the properties of the radiation are determined by the local direction of the magnetic field (beyond this region electromagnetic waves are not longer affected by the NS magnetic field). By doing this, the polarisation properties of the radiation can be fairly well obtained without solving the, numerically demanding, evolution of the Stokes parameters in the magnetised vacuum around the star. I considered a dipolar magnetic field topology and a temperature distribution over the NS as that inferred from the observation of RX J1856, the nearest and brightest XDINS. The results of the simulation show that **a)** QED vacuum birefringence increases substantially the expected polarisation fraction of the radiation compared to that produced from the whole NS surface (depolarised by the non-uniform topology of the magnetic field at the star surface), **b)** for a gaseous atmosphere, the expected phase-averaged polarisation fraction can be as high as $\approx 80\%$ in the optical band and $\approx 99\%$ in the X-ray band. Instead, for a condensed surface, while in the optical band the phase averaged polarisation fraction can be as high as $\approx 35\%$, in the X-ray band the phase averaged polarisation fraction is substantially reduced, **c)** for a gaseous atmosphere, the phase averaged polarisation angle is the same in the optical and X-ray band. However, for a condensed surface, the phase averaged polarisation angle in the X-ray band is shifted by 90° with respect to the optical band. Therefore, combined polarimetric observation in the optical and X-ray band may allow us to discriminate the whether the surface of XDINSs is composed by an atmosphere or condensed surface.

Motivated by previous results, optical polarimetric observations were carried out for the very fist time of a XDINS system. In Chapter §3, I presented and discussed the linear (phase averaged) polarisation fraction, 16.43 ± 5.26 %, and (phase averaged) polarisation angle, $145.^\circ 39 \pm 9.^\circ 44$, measured for RX J1856, using the VLT in Chile. Potential sources of contamination of the polarisation signal, such

a relatively close cloud complex, interstellar dust, or bow shock nebula were ruled out. The observations were confronted with theoretical models (developed in Chapter §2) calculated in two cases: accounting or not for vacuum birefringence. I found that, if vacuum birefringence is not present, neither the emission from a gaseous atmosphere nor a condensed surface can reproduce the central value of the observed (phase averaged) polarisation fraction. Instead, if vacuum birefringence is accounted for, then both emission models atmosphere and condensed surface can reproduce the observed polarisation fraction. Furthermore, by combining the information of the measured polarisation fraction and the X-ray pulsed fraction it was possible to constrain the viewing geometry for RX J1856. It turned out that the constraints on the viewing geometry are compatible with previous studies of RX J1856 (Ho, 2007) only when vacuum birefringence is accounted for in the models. Therefore, it was possible to conclude that the observed (phase averaged) polarisation fraction 16.43 ± 5.26 % in thermal emission from RX J1856 suggests a first evidence for QED vacuum birefringence induced by a strong magnetic field.

The potential detection of the signal of vacuum birefringence in RX J1856 needs to be confirmed in other sources. Future missions of X-ray polarimetry such as IXPE and eXTP will allow us to perform polarimetric observation of persistent and transient magnetars in the $2-8$ keV energy range. These sources have magnetic fields as strong as 10^{14} G, with outburst activity in which the X-ray luminosity can increase up to 3 orders of magnitude in time scale of hours and decay in time scale of months. In the magnetar model, this decay of the X-ray luminosity is explained in term of an untwisting magnetosphere. In Chapter §4, I model the polarisation properties of magnetars with globally twisted dipole fields. I investigated the case in which thermal emission is produced from one hot polar cap (located at the magnetic pole) and it is not affected by RCS effects. I found that if vacuum birefringence is accounted for, then **a)** the (phase-averaged) polarisation fraction can be substantially high (up to 99 %) for some viewing geometries and it should remain unchanged during the untwist of the magnetosphere and **b)** the (phase-averaged) polarisation angle can change up to 23° for an untwisting of $\Delta\Phi = 0.5$ (from the

onset until the end of the X-ray flux decay). Instead, if vacuum birefringence is not present, then **a)** the (phase-averaged) polarisation fraction should increase during the X-ray flux decay (as the hot polar cap shrinks over time) and **b)** the (phase-averaged) polarisation angle should remain unchanged during the X-ray flux decay. These results show that the observation of thermal emission from magnetars (not affected by RCS), can be used as a test for both the magnetar model and vacuum birefringence effects.

In the last research chapter I studied the atmosphere of magnetars. As mentioned above, these sources may have twisted magnetospheres which are sustained by large currents of charged particles. These particles move along the twisted field lines and return to the surface, producing a particle bombardment. This particle bombardment will affect the transport of radiation in the atmosphere of the magnetar and produce a thermal spectrum substantially different from those of "passively" cooling NSs. In Chapter §5, I presented the solutions of the equations for the polarised transport of radiation in the atmosphere of magnetars coupled with the hydrostatic equilibrium and the energy balance equations. I have taken into account for vacuum resonance and vacuum conversion in the transport of radiation. I considered the case of a grey atmosphere in which fast magnetospheric particles are primary decelerated by magneto-Coulomb interaction, followed by an e^+e^- avalanche. I found that the temperature profile of the atmosphere is described by an external hot layer, with a nearly uniform interior at a lower temperature. From this result, it was possible to infer that the emergent spectrum may be described by nearly blackbody spectrum with a potential optical/infrared excess. Furthermore, the solutions show that the linear polarisation fraction of the emergent radiation depends on the luminosity of the source. Again, this is a relevant result in view of future missions of X-ray polarimetry such as XIPE and eXTP, that will allow us to observe transient magnetars at different flux levels during their outburst decay, in turn allowing to monitor the variation of the source X-ray polarisation signal.

6.2 Future work

The work presented in this thesis can be further developed in multiple directions. Following Chapter §5, on the numerical side, the next step would be to compute the frequency dependent transport of radiation in the magnetar atmosphere (under particle bombardment) in a self-consistent way i.e., solving iteratively the frequency dependent transfer equations (for each normal mode) coupled with energy balance and hydrostatic equilibrium equations. The goal of this work would be to obtain the thermal spectrum of magnetars and to asses a potential optical/infrared excess suggested by the results obtained in the "grey" case (studied in Chapter §5).

Linked to the study of atmosphere of magnetars, but rather on the theoretical side, there are also a number of studies to be developed such as the distribution of the energy deposition in the atmosphere by the particle bombardment and the stopping column density associated to this. For instance, these investigations need a further detailed study of the plasma physics under ultra strong magnetic fields and the cross sections for the processes involved in the calculations of the stopping column density such as Magneto-Coulomb interactions, photon splitting, electron scattering, etc. In particular, available cross section are either valid for magnetic field lower than those found in magnetars (as the case of Magneto-Coulomb interactions and Compton scattering) or do not account for plasma effects (as the case of photon splitting).

The models computed in Chapters §2 and §3, for the study the polarisation properties the thermal emission from XDINSs may be extended to include other magnetic field topologies. For instance, recent X-ray observations of XDINSs show a phase dependent proton cyclotron signature associated to a localised mutipolar component close to the NS surface (Borghese et al., 2015). Computing the polarisation pattern for this kind of source would be useful as a scientific case for future missions of soft X-ray polarimetry (below 1 keV) under study (e.g., Marshall et al., 2015).

The models presented in Chapters §2 and §3 were extended, in Chapter §4, for studying the polarisation properties of magnetars with twisted magnetospheres.

One of the main simplifications was that RCS process were not accounted for, which means that the models are valid for magnetospheres with a relatively small twist that would not produce significant currents of charged particles. Of course, if the magnetosphere of the magnetar presents a large twist, then RCS effects are expected to largely affect the thermal component of the spectrum. This may be an interesting study in view of the IXPE (NASA, Weisskopf et al., 2013) and eXTP (CAS, Zhang et al., 2016) missions that will allow us to perform X-ray (2-8 keV) polarimetric observations of magnetars. Furthermore, if it will be possible to solve the frequency dependent transport of radiation for the atmosphere heated by a particle bombardment (discussed in Chapter §5), the next step would be to compute the polarisation properties (as well as the spectrum and pulsed fraction) of magnetars for different viewing geometries in a self consistent way i.e., to develop a unitary model that includes the atmosphere (with particle bombardment) plus RCS effects due a twisted magnetosphere, plus QED vacuum birefringence. The development of such model is a challenging and long sought goal in the community working in magnetar science.

In addition, the models presented in Chapters §2 and §3 need to be confronted with observational data of XDINSs. In particular, **a)** follow up VLT optical polarimetric observations of RX J1856 (with larger exposure time) are going to be very important to confirm the potential signal of QED vacuum birefringence found in this source. **b)** Observation of circular polarisation should be also pursued. The polarisation properties of XDINSs discussed in Chapter §2 were computed at the "adiabatic" radius considering that the thermal emission is linearly polarised. This was justified by performing the full evolution of the Stokes parameters in the magnetised vacuum around the star, which resulted in circularly polarised radiation less than 2%. This result can be tested with further observations aimed to detect circular polarisation in RX J1856. A non-detection, of course, would be compatible with the theoretical framework of the model presented in Chapter §2. However, a significant detection of circular polarisation would mean that there are missing physics ingredients in the models, which would be interesting to study. **c)** Although, X-

ray polarimetric missions below 1 keV are still under study (e.g., Marshall et al., 2015), if developed in the future, this kind of instrument will allow us to perform observations that would be also very important (combined with optical polarimetric observations) to determine the state of the matter in the surface of XDINSs, for which the models discussed in Chapter §2 show clear differences if the polarised thermal emission from the XDINSs is produced either in a gaseous atmosphere or a condensed surface.

Furthermore, future polarimetric observations of transient and persistent magnetars can be confronted with the models discussed in Chapter §4 and §5. In particular, **a)** it would be interesting the find a significant variation of the polarisation angle during the flux decay of a transient magnetar with X-ray observations by the IXPE and eXTP missions (to be lunched during the next years). This may be a clear signature of QED vacuum polarisation effects and a validation of the magnetar model with untwisting magnetospheres. **b)** Finally, optical and infrared observations of magnetars may be also interesting to be pursued in view of the potential optical/infrared excess in the thermal emission suggested by the grey atmosphere model studied in Chapter §5. These kind of observations are going to be also important to drive further studies on the atmospheric structure of magnetars and its connection with the magnetospheric activity.

In closing, studies as described in this thesis are important to understand the properties of matter, vacuum and radiation under super strong magnetic fields. They have also shown the potential of developing numerical models and techniques to study the polarised thermal emission from XDINSs and magnetars, which can be tested, for example, by future missions of X-ray polarimetry. These missions promise to open a new golden age for the study of compact objects and fundamental physics.

Bibliography

Akmal A., Pandharipande V. R., and Ravenhall D. G. (1998), "Equation of state of nucleon matter and neutron star structure." Phys. Rev. C, 58, 1804–1828.

Albano A., Turolla R., Israel G. L., Zane S., Nobili L., and Stella L. (2010), "A Unified Timing and Spectral Model for the Anomalous X-ray Pulsars XTE J1810-197 and CXOU J164710.2-455216." ApJ, 722, 788–802.

Alme M. L. and Wilson J. R. (1973), "X-Ray Emission from a Neutron Star Accreting Material." ApJ, 186, 1015–1026.

An H., Kaspi V. M., Archibald R., and Cumming A. (2013), "Spectral and Timing Properties of the Magnetar CXOU J164710.2-455216." ApJ, 763, 82.

Appenzeller I., Fricke K., Fürtig W., Gässler W., Häfner R., Harke R., Hess H.-J., Hummel W., Jürgens P., Kudritzki R.-P., et al. (1998), "Successful commissioning of FORS1 - the first optical instrument on the VLT." *The Messenger*, 94, 1–6.

Arons J., Klein R. I., and Lea S. M. (1987), "Radiation gasdynamics of polar CAP accretion onto magnetized neutron stars - Basic theory." ApJ, 312, 666–699.

Baade W. and Zwicky F. (1934), "Cosmic Rays from Super-novae." *Proceedings of the National Academy of Science*, 20, 259–263.

Baring M. G. and Harding A. K. (2008), "Modeling the Non-Thermal X-ray Tail Emission of Anomalous X-ray Pulsars." In *Astrophysics of Compact Objects* (Y.-F. Yuan, X.-D. Li, and D. Lai, eds.), volume 968 of *American Institute of Physics Conference Series*, 93–100.

Baring M. G., Wadiasingh Z., and Gonthier P. L. (2011), "Cooling Rates for Relativistic Electrons Undergoing Compton Scattering in Strong Magnetic Fields." ApJ, 733, 61.

Bellazzini R., Brez A., Costa E., Minuti M., Muleri F., Pinchera M., Rubini A., Soffitta P., and Spandre G. (2013), "Photoelectric X-ray Polarimetry with Gas Pixel Detectors." *Nuclear Instruments and Methods in Physics Research A*, 720, 173–177.

Beloborodov A. M. (2009), "Untwisting Magnetospheres of Neutron Stars." ApJ, 703, 1044–1060.

Beloborodov A. M. (2013), "On the Mechanism of Hard X-Ray Emission from Magnetars." ApJ, 762, 13.

Beloborodov A. M. and Thompson C. (2007), "Corona of Magnetars." ApJ, 657, 967–993.

Bernardini F., Israel G. L., Dall'Osso S., Stella L., Rea N., Zane S., Turolla R., Perna R., Falanga M., Campana S., et al. (2009), "From outburst to quiescence: the decay of the transient AXP XTE J1810-197." A&A, 498, 195–207.

Bethe H. and Heitler W. (1934), "On the Stopping of Fast Particles and on the Creation of Positive Electrons." *Proceedings of the Royal Society of London Series A*, 146, 83–112.

Bildsten L., Salpeter E. E., and Wasserman I. (1992), "The fate of accreted CNO elements in neutron star atmospheres - X-ray bursts and gamma-ray lines." ApJ, 384, 143–176.

Bogdanov S. (2014), "Modeling the X-Rays from the Central Compact Object PSR J1852+0040 in Kesteven 79: Evidence for a Strongly Magnetized Neutron Star." ApJ, 790, 94.

Borghese A., Rea N., Coti Zelati F., Tiengo A., and Turolla R. (2015), "Discovery of a Strongly Phase-variable Spectral Feature in the Isolated Neutron Star RX J0720.4-3125." ApJ, 807, L20.

Braithwaite J. and Spruit H. C. (2006), "Evolution of the magnetic field in magnetars." A&A, 450, 1097–1106.

Burrows A., Dessart L., Livne E., Ott C. D., and Murphy J. (2007), "Simulations of Magnetically Driven Supernova and Hypernova Explosions in the Context of Rapid Rotation." ApJ, 664, 416–434.

Burwitz V., Haberl F., Neuhäuser R., Predehl P., Trümper J., and Zavlin V. E. (2003), "The thermal radiation of the isolated neutron star RX J1856.5-3754 observed with Chandra and XMM-Newton." A&A, 399, 1109–1114.

Cameron R., Cantatore G., Melissinos A. C., Ruoso G., Semertzidis Y., Halama H. J., Lazarus D. M., Prodell A. G., Nezrick F., Rizzo C., et al. (1993), "Search for nearly massless, weakly coupled particles by optical techniques." Phys. Rev. D, 47, 3707–3725.

Camilo F., Ransom S. M., Halpern J. P., and Reynolds J. (2007), "1E 1547.0-5408: A Radio-emitting Magnetar with a Rotation Period of 2 Seconds." ApJ, 666, L93–L96.

Camilo F., Ransom S. M., Halpern J. P., Reynolds J., Helfand D. J., Zimmerman N., and Sarkissian J. (2006), "Transient pulsed radio emission from a magnetar." Nature, 442, 892–895.

Chadwick J. (1932), "The Existence of a Neutron." *Proceedings of the Royal Society of London Series A*, 136, 692–708.

Chen S.-J., Mei H.-H., and Ni W.-T. (2007), "Q a Experiment to Search for Vacuum Dichroism, Pseudoscalar-Photon Interaction and Millicharged Fermions." *Modern Physics Letters A*, 22, 2815–2831.

Cheng K. S. and Zhang L. (2001), "High-Energy Gamma-Ray Emission from Anomalous X-Ray Pulsars." ApJ, 562, 918–924.

Cikota A., Patat F., Cikota S., and Faran T. (2017), "Linear spectropolarimetry of polarimetric standard stars with VLT/FORS2." MNRAS, 464, 4146–4159.

Costa E., Soffitta P., Bellazzini R., Brez A., Lumb N., and Spandre G. (2001), "An efficient photoelectric X-ray polarimeter for the study of black holes and neutron stars." Nature, 411, 662–665.

Cropper M., Haberl F., Zane S., and Zavlin V. E. (2004), "Timing analysis of the isolated neutron star RX J0720.4-3125 revisited." MNRAS, 351, 1099–1108.

Daugherty J. K. and Harding A. K. (1989), "Comptonization of thermal photons by relativistic electron beams." ApJ, 336, 861–874.

den Hartog P. R., Kuiper L., Hermsen W., Kaspi V. M., Dib R., Knödlseder J., and Gavriil F. P. (2008), "Detailed high-energy characteristics of AXP 4U 0142+61. Multi-year observations with INTEGRAL, RXTE, XMM-Newton, and ASCA." A&A, 489, 245–261.

Dhillon V. S., Marsh T. R., Hulleman F., van Kerkwijk M. H., Shearer A., Littlefair S. P., Gavriil F. P., and Kaspi V. M. (2005), "High-speed, multicolour optical photometry of the anomalous X-ray pulsar 4U 0142+61 with ULTRACAM." MNRAS, 363, 609–614.

Dhillon V. S., Marsh T. R., Littlefair S. P., Copperwheat C. M., Hickman R. D. G., Kerry P., Levan A. J., Rea N., Savoury C. D. J., Tanvir N. R., et al. (2011), "The first observation of optical pulsations from a soft gamma repeater: SGR 0501+4516." MNRAS, 416, L16–L20.

Dhillon V. S., Marsh T. R., Littlefair S. P., Copperwheat C. M., Kerry P., Dib R., Durant M., Kaspi V. M., Mignani R. P., and Shearer A. (2009), "Optical pulsations from the anomalous X-ray pulsar 1E1048.1-5937." MNRAS, 394, L112–L116.

Donati J.-F., Howarth I. D., Bouret J.-C., Petit P., Catala C., and Landstreet J. (2006), "Discovery of a strong magnetic field on the O star HD 191612: new clues to the future of θ^1 Orionis C*." MNRAS, 365, L6–L10.

Draine B. T. (2004), "Astrophysics of Dust in Cold Clouds." In *The Cold Universe, Saas-Fee Advanced Course 32, Springer-Verlag, 308 pages, 129 figures, Lecture Notes 2002 of the Swiss Society for Astronomy and Astrophysics (SSAA), Springer, 2004. Edited by A.W. Blain, F. Combes, B.T. Draine, D. Pfenniger and Y. Revaz, ISBN 354040838x, p. 213* (A. W. Blain, F. Combes, B. T. Draine, D. Pfenniger, and Y. Revaz, eds.), 213.

Duncan R. C. and Thompson C. (1992), "Formation of very strongly magnetized neutron stars - Implications for gamma-ray bursts." ApJ, 392, L9–L13.

Eatough R. P., Falcke H., Karuppusamy R., Lee K. J., Champion D. J., Keane E. F., Desvignes G., Schnitzeler D. H. F. M., Spitler L. G., Kramer M., et al. (2013), "A strong magnetic field around the supermassive black hole at the centre of the Galaxy." Nature, 501, 391–394.

Fernández R. and Davis S. W. (2011), "The X-ray Polarization Signature of Quiescent Magnetars: Effect of Magnetospheric Scattering and Vacuum Polarization." ApJ, 730, 131.

Fernández R. and Thompson C. (2007), "Resonant Cyclotron Scattering in Three Dimensions and the Quiescent Nonthermal X-ray Emission of Magnetars." ApJ, 660, 615–640.

Ferrario L. and Wickramasinghe D. (2006), "Modelling of isolated radio pulsars and magnetars on the fossil field hypothesis." MNRAS, 367, 1323–1328.

Flowers E. and Ruderman M. A. (1977), "Evolution of pulsar magnetic fields." ApJ, 215, 302–310.

Ginzburg V. L. (1970), *The propagation of electromagnetic waves in plasmas*. International Series of Monographs in Electromagnetic Waves, Oxford: Pergamon, 1970, 2nd rev. and enl. ed.

Gnedin Y. N. and Pavlov G. G. (1974), "The transfer equations for normal waves and radiation polarization in an anisotropic medium." *Soviet Journal of Experimental and Theoretical Physics*, 38, 1806–1817.

Gnedin Y. N., Pavlov G. G., and Shibanov Y. A. (1978), "Influence of polarization of vacuum in a magnetic field on the propagation of radiation in a plasma." *Soviet Journal of Experimental and Theoretical Physics Letters*, 27, 305.

Godfrey B. B., Shanahan W. R., and Thode L. E. (1975), "Linear theory of a cold relativistic beam propagating along an external magnetic field." *Physics of Fluids*, 18, 346–355.

Gold T. (1968), "Rotating Neutron Stars as the Origin of the Pulsating Radio Sources." Nature, 218, 731–732.

Goldreich P. and Reisenegger A. (1992), "Magnetic field decay in isolated neutron stars." ApJ, 395, 250–258.

González Caniulef D., Zane S., Taverna R., Turolla R., and Wu K. (2016), "Polarized thermal emission from X-ray dim isolated neutron stars: the case of RX J1856.5-3754." MNRAS, 459, 3585–3595.

González-Caniulef D., Zane S., Turolla R., and Wu K. (2019), "Atmosphere of strongly magnetized neutron stars heated by particle bombardment." MNRAS, 483, 599–613.

Goriely S., Chamel N., and Pearson J. M. (2010), "Further explorations of Skyrme-Hartree-Fock-Bogoliubov mass formulas. XII. Stiffness and stability of neutron-star matter." Phys. Rev. C, 82, 035804.

Gotthelf E. V., Perna R., and Halpern J. P. (2010), "Modeling the Surface X-ray Emission and Viewing Geometry of PSR J0821-4300 in Puppis A." ApJ, 724, 1316–1324.

Götz D., Mereghetti S., Tiengo A., and Esposito P. (2006), "Magnetars as persistent hard X-ray sources: INTEGRAL discovery of a hard tail in SGR 1900+14." A&A, 449, L31–L34.

Greenstein G. and Hartke G. J. (1983), "Pulselike character of blackbody radiation from neutron stars." ApJ, 271, 283–293.

Haberl F. (2007), "The magnificent seven: magnetic fields and surface temperature distributions." Ap&SS, 308, 181–190.

Haberl F., Motch C., Zavlin V. E., Reinsch K., Gänsicke B. T., Cropper M., Schwope A. D., Turolla R., and Zane S. (2004a), "The isolated neutron star X-ray pulsars RX J0420.0-5022 and RX J0806.4-4123: New X-ray and optical observations." A&A, 424, 635–645.

Haberl F., Schwope A. D., Hambaryan V., Hasinger G., and Motch C. (2003), "A broad absorption feature in the X-ray spectrum of the isolated neutron star RBS1223 (1RXS J130848.6+212708)." A&A, 403, L19–L23.

Haberl F., Zavlin V. E., Trümper J., and Burwitz V. (2004b), "A phase-dependent absorption line in the spectrum of the X-ray pulsar RX J0720.4-3125." A&A, 419, 1077–1085.

Haensel P., Potekhin A. Y., and Yakovlev D. G., eds. (2007), *Neutron Stars 1 : Equation of State and Structure*, volume 326 of *Astrophysics and Space Science Library*.

Halpern J. P. and Gotthelf E. V. (2010), "Spin-Down Measurement of PSR J1852+0040 in Kesteven 79: Central Compact Objects as Anti-Magnetars." ApJ, 709, 436–446.

Halpern J. P. and Gotthelf E. V. (2011), "On the Spin-down and Magnetic Field of the X-ray Pulsar 1E 1207.4-5209." ApJ, 733, L28.

Harding A. K. and Lai D. (2006), "Physics of strongly magnetized neutron stars." *Reports on Progress in Physics*, 69, 2631–2708.

Heisenberg W. and Euler H. (1936), "Folgerungen aus der Diracschen Theorie des Positrons." *Zeitschrift fur Physik*, 98, 714–732.

Heitler W. (1954), *Quantum theory of radiation*. International Series of Monographs on Physics, Oxford: Clarendon, 1954, 3rd ed.

Helfand D. J., Gotthelf E. V., and Halpern J. P. (2001), "Vela Pulsar and Its Synchrotron Nebula." ApJ, 556, 380–391.

Hewish A., Bell S. J., Pilkington J. D. H., Scott P. F., and Collins R. A. (1968), "Observation of a Rapidly Pulsating Radio Source." Nature, 217, 709–713.

Heyl J. S. and Shaviv N. J. (2000), "Polarization evolution in strong magnetic fields." MNRAS, 311, 555–564.

Heyl J. S. and Shaviv N. J. (2002), "QED and the high polarization of the thermal radiation from neutron stars." Phys. Rev. D, 66, 023002.

Heyl J. S., Shaviv N. J., and Lloyd D. (2003), "The high-energy polarization-limiting radius of neutron star magnetospheres - I. Slowly rotating neutron stars." MNRAS, 342, 134–144.

Ho W. C. G. (2007), "Constraining the geometry of the neutron star RX J1856.5-3754." MNRAS, 380, 71–77.

Ho W. C. G., Kaplan D. L., Chang P., van Adelsberg M., and Potekhin A. Y. (2007), "Magnetic hydrogen atmosphere models and the neutron star RX J1856.5-3754." MNRAS, 375, 821–830.

Ho W. C. G. and Lai D. (2001), "Atmospheres and spectra of strongly magnetized neutron stars." MNRAS, 327, 1081–1096.

Ho W. C. G. and Lai D. (2003), "Atmospheres and spectra of strongly magnetized neutron stars - II. The effect of vacuum polarization." MNRAS, 338, 233–252.

Ho W. C. G., Lai D., Potekhin A. Y., and Chabrier G. (2003a), "Atmospheres and Spectra of Strongly Magnetized Neutron Stars. III. Partially Ionized Hydrogen Models." ApJ, 599, 1293–1301.

Ho W. C. G., Lai D., Potekhin A. Y., and Chabrier G. (2003b), "Atmospheres and Spectra of Strongly Magnetized Neutron Stars. III. Partially Ionized Hydrogen Models." ApJ, 599, 1293–1301.

Ho W. C. G., Potekhin A. Y., and Chabrier G. (2008), "Model X-Ray Spectra of Magnetic Neutron Stars with Hydrogen Atmospheres." ApJS, 178, 102–109.

Kaminker A. D., Pavlov G. G., and Shibanov I. A. (1982), "Radiation for a strongly-magnetized plasma - The case of predominant scattering." Ap&SS, 86, 249–297.

Kaplan D. L., Chatterjee S., Gaensler B. M., and Anderson J. (2008), "A Precise Proper Motion for the Crab Pulsar, and the Difficulty of Testing Spin-Kick Alignment for Young Neutron Stars." ApJ, 677, 1201–1215.

Kaplan D. L., Kamble A., van Kerkwijk M. H., and Ho W. C. G. (2011a), "New Optical/Ultraviolet Counterparts and the Spectral Energy Distributions of Nearby, Thermally Emitting, Isolated Neutron Stars." ApJ, 736, 117.

Kaplan D. L., Kamble A., van Kerkwijk M. H., and Ho W. C. G. (2011b), "New Optical/Ultraviolet Counterparts and the Spectral Energy Distributions of Nearby, Thermally Emitting, Isolated Neutron Stars." ApJ, 736, 117.

Kaplan D. L. and van Kerkwijk M. H. (2005a), "A Coherent Timing Solution for the Nearby Isolated Neutron Star RX J0720.4-3125." ApJ, 628, L45–L48.

Kaplan D. L. and van Kerkwijk M. H. (2005b), "A Coherent Timing Solution for the Nearby Isolated Neutron Star RX J1308.6+2127/RBS 1223." ApJ, 635, L65–L68.

Kaplan D. L. and van Kerkwijk M. H. (2009a), "Constraining the Spin-down of the Nearby Isolated Neutron Star RX J0806.4-4123, and Implications for the Population of Nearby Neutron Stars." ApJ, 705, 798–808.

Kaplan D. L. and van Kerkwijk M. H. (2009b), "Constraining the Spin-Down of the Nearby Isolated Neutron Star RX J2143.0+0654." ApJ, 692, L62–L66.

Kaplan D. L. and van Kerkwijk M. H. (2011), "A Coherent Timing Solution for the Nearby, Thermally Emitting Isolated Neutron Star RX J0420.0-5022." ApJ, 740, L30.

Kaplan D. L., van Kerkwijk M. H., and Anderson J. (2002), "The Parallax and Proper Motion of RX J1856.5-3754 Revisited." ApJ, 571, 447–457.

Kaspi V. M. and Beloborodov A. M. (2017), "Magnetars." ARA&A, 55, 261–301.

Keane E. F. and Kramer M. (2008), "On the birthrates of Galactic neutron stars." MNRAS, 391, 2009–2016.

Kern B. and Martin C. (2002), "Optical pulsations from the anomalous X-ray pulsar 4U0142+61." Nature, 417, 527–529.

Kotov Y. D. and Kelner S. R. (1985), "The magneto-Coulomb radiation of ultrarelativistic electrons in a strong magnetic field." *Soviet Astronomy Letters*, 11, 392–394.

Kotov Y. D., Kelner S. R., and Bogovalov S. V. (1986), "Radiation by Ultrarelativistic Electrons Entering a Dense Medium in a Strong Magnetic Field." *Soviet Astronomy Letters*, 12, 168–171.

Lai D. (2001), "Matter in strong magnetic fields." *Reviews of Modern Physics*, 73.

Lai D. and Ho W. C. G. (2002), "Resonant Conversion of Photon Modes Due to Vacuum Polarization in a Magnetized Plasma: Implications for X-Ray Emission from Magnetars." ApJ, 566, 373–377.

Lasker B. M., Lattanzi M. G., McLean B. J., Bucciarelli B., Drimmel R., Garcia J., Greene G., Guglielmetti F., Hanley C., Hawkins G., et al. (2008), "The Second-Generation Guide Star Catalog: Description and Properties." AJ, 136, 735–766.

Lattimer J. M. (2012), "The Nuclear Equation of State and Neutron Star Masses." *Annual Review of Nuclear and Particle Science*, 62, 485–515.

Levin L., Bailes M., Bates S., Bhat N. D. R., Burgay M., Burke-Spolaor S., D'Amico N., Johnston S., Keith M., Kramer M., et al. (2010), "A Radio-loud Magnetar in X-ray Quiescence." ApJ, 721, L33–L37.

Lloyd D. A. (2003), "Model atmospheres and thermal spectra of magnetized neutron stars." *ArXiv Astrophysics e-prints*.

Lloyd D. A., Perna R., Slane P., Nicastro F., and Hernquist L. (2003), "A pulsar-atmosphere model for PSR 0656+14." *ArXiv Astrophysics e-prints*.

Lyne A. G. and Graham-Smith F. (1998), *Pulsar astronomy*.

Lyubarsky Y. and Eichler D. (2007), "On the corona of magnetars." *ArXiv e-prints*.

Manchester R. N., Hobbs G. B., Teoh A., and Hobbs M. (2005), "The Australia Telescope National Facility Pulsar Catalogue." AJ, 129, 1993–2006.

Marshall H. L., Schulz N. S., Windt D. L., Gullikson E. M., Craft M., Blake E., and Ross C. (2015), "The use of laterally graded multilayer mirrors for soft x-ray polarimetry." volume 9603 of Proc. SPIE, 960319. Society of Photo-Optical Instrumentation Engineers (SPIE) Conference Series.

Mathewson D. S. and Ford V. L. (1971), "Polarization observations of 1800 stars." MNRAS, 153, 525.

McLaughlin M. A., Lyne A. G., Lorimer D. R., Kramer M., Faulkner A. J., Manchester R. N., Cordes J. M., Camilo F., Possenti A., Stairs I. H., et al. (2006), "Transient radio bursts from rotating neutron stars." Nature, 439, 817–820.

Medin Z. and Lai D. (2007), "Condensed surfaces of magnetic neutron stars, thermal surface emission, and particle acceleration above pulsar polar caps." MNRAS, 382, 1833–1852.

Melrose D. B. and Zhelezniakov V. V. (1981), "Quantum theory of cyclotron emission and the X-ray line in HER X-1." A&A, 95, 86–93.

Meng Y., Lin J., Zhang L., Reeves K. K., Zhang Q. S., and Yuan F. (2014), "An MHD Model for Magnetar Giant Flares." ApJ, 785, 62.

Mereghetti S. (2011), "X-ray emission from isolated neutron stars." *Astrophysics and Space Science Proceedings*, 21, 345.

Mereghetti S., Pons J. A., and Melatos A. (2015), "Magnetars: Properties, Origin and Evolution." Space Sci. Rev., 191, 315–338.

Mészáros P. (1992), *High-energy radiation from magnetized neutron stars.* High-energy radiation from magnetized neutron stars., by Mészáros, P.. University of Chicago Press, Chicago, IL (USA), 1992, 544 p., ISBN 0-226-52093-5, Price US98.00.$ISBN 0-226-52094-3 (paper)$.

Meszaros P. and Ventura J. (1979), "Vacuum polarization effects on radiative opacities in a strong magnetic field." Phys. Rev. D, 19, 3565–3575.

Mignani R. P. (2011), "Optical, ultraviolet, and infrared observations of isolated neutron stars." *Advances in Space Research*, 47, 1281–1293.

Mignani R. P., Moran P., Shearer A., Testa V., Słowikowska A., Rudak B., Krzeszowski K., and Kanbach G. (2015), "VLT polarimetry observations of the middle-aged pulsar PSR B0656+14." A&A, 583, A105.

Mignani R. P., Testa V., González Caniulef D., Taverna R., Turolla R., Zane S., and Wu K. (2017), "Evidence for vacuum birefringence from the first optical-polarimetry measurement of the isolated neutron star RX J1856.5-3754." MNRAS, 465, 492–500.

Mignani R. P., Vande Putte D., Cropper M., Turolla R., Zane S., Pellizza L. J., Bignone L. A., Sartore N., and Treves A. (2013), "The birthplace and age of the isolated neutron star RX J1856.5-3754." MNRAS, 429, 3517–3521.

Mitchell J. P., Braithwaite J., Reisenegger A., Spruit H., Valdivia J. A., and Langer N. (2015), "Instability of magnetic equilibria in barotropic stars." MNRAS, 447, 1213–1223.

Mori K. and Ho W. C. G. (2007), "Modelling mid-Z element atmospheres for strongly magnetized neutron stars." MNRAS, 377, 905–919.

Motch C., Pires A. M., Haberl F., Schwope A., and Zavlin V. E. (2009), "Proper motions of thermally emitting isolated neutron stars measured with Chandra." A&A, 497, 423–435.

Motch C., Zavlin V. E., and Haberl F. (2003), "The proper motion and energy distribution of the isolated neutron star RX J0720.4-3125." A&A, 408, 323–330.

Nobili L., Turolla R., and Zane S. (2008), "X-ray spectra from magnetar candidates - I. Monte Carlo simulations in the non-relativistic regime." MNRAS, 386, 1527–1542.

Noutsos A., Kramer M., Carr P., and Johnston S. (2012), "Pulsar spin-velocity alignment: further results and discussion." MNRAS, 423, 2736–2752.

Olausen S. A. and Kaspi V. M. (2014), "The McGill Magnetar Catalog." ApJS, 212, 6.

Oosterbroek T., Parmar A. N., Mereghetti S., and Israel G. L. (1998), "The two-component X-ray spectrum of the 6.4 S pulsar 1E 1048.1-5937." A&A, 334, 925–930.

Oppenheimer J. R. and Volkoff G. M. (1939), "On Massive Neutron Cores." *Physical Review*, 55, 374–381.

Özel F. (2001), "Surface Emission Properties of Strongly Magnetic Neutron Stars." ApJ, 563, 276–288.

Özel F. (2003), "The Effect of Vacuum Polarization and Proton Cyclotron Resonances on Photon Propagation in Strongly Magnetized Plasmas." ApJ, 583, 402–409.

Pacini F. (1967), "Energy Emission from a Neutron Star." Nature, 216, 567–568.

Page D. (1995), "Surface temperature of a magnetized neutron star and interpretation of the ROSAT data. 1: Dipole fields." ApJ, 442, 273–285.

Parfrey K., Beloborodov A. M., and Hui L. (2013), "Dynamics of Strongly Twisted Relativistic Magnetospheres." ApJ, 774, 92.

Park M.-G. (1990), "Self-consistent Models of Spherical Accretion onto Black Holes. II. Two-Temperature Solutions with Pairs." ApJ, 354, 83.

Park M.-G. and Ostriker J. P. (1989), "Spherical accretion onto black holes - A new, higher efficiency type of solution with significant pair production." ApJ, 347, 679–683.

Patel S. K., Kouveliotou C., Woods P. M., Tennant A. F., Weisskopf M. C., Finger M. H., Göğüş E., van der Klis M., and Belloni T. (2001), "Chandra Observations of the Anomalous X-Ray Pulsar 1E 2259+586." ApJ, 563, L45–L48.

Pavan L., Turolla R., Zane S., and Nobili L. (2009), "Topology of magnetars external field - I. Axially symmetric fields." MNRAS, 395, 753–763.

Pavlov G. G., Kargaltsev O. Y., Sanwal D., and Garmire G. P. (2001), "Variability of the Vela Pulsar Wind Nebula Observed with Chandra." ApJ, 554, L189–L192.

Pavlov G. G. and Panov A. N. (1976), "Photon absorption and emission in Coulomb collisions in a magnetic field." *Soviet Journal of Experimental and Theoretical Physics*, 44, 300.

Pavlov G. G. and Shibanov Y. A. (1979), "Influence of vacuum polarization by a magnetic field on the propagation of electromagnetic waves in a plasma." *Soviet Journal of Experimental and Theoretical Physics*, 49, 741.

Pavlov G. G., Shibanov Y. A., Ventura J., and Zavlin V. E. (1994), "Model atmospheres and radiation of magnetic neutron stars: Anisotropic thermal emission." A&A, 289, 837–845.

Pavlov G. G., Shibanov Y. A., Zavlin V. E., and Meyer R. D. (1995), "Neutron Star Atmospheres." volume 450 of *NATO Advanced Science Institutes (ASI) Series C*, 71. NATO Advanced Science Institutes (ASI) Series C.

Pavlov G. G. and Zavlin V. E. (2000), "Polarization of Thermal X-Rays from Isolated Neutron Stars." ApJ, 529, 1011–1018.

Perna R. and Pons J. A. (2011), "A Unified Model of the Magnetar and Radio Pulsar Bursting Phenomenology." ApJ, 727, L51.

Perna R., Viganò D., Pons J. A., and Rea N. (2013), "The imprint of the crustal magnetic field on the thermal spectra and pulse profiles of isolated neutron stars." MNRAS, 434, 2362–2372.

Pires A. M., Haberl F., Zavlin V. E., Motch C., Zane S., and Hohle M. M. (2014), "XMM-Newton reveals a candidate period for the spin of the "Magnificent Seven" neutron star RX J1605.3+3249." A&A, 563, A50.

Potekhin A. (2000), "Heat and charge transport in envelopes of weakly and strongly magnetized neutron stars." volume 202 of *Astronomical Society of the Pacific Conference Series*, 621. IAU Colloq. 177: Pulsar Astronomy - 2000 and Beyond.

Potekhin A. Y. (2014), "Atmospheres and radiating surfaces of neutron stars." *Physics Uspekhi*, 57, 735-770.

Potekhin A. Y., Baiko D. A., Haensel P., and Yakovlev D. G. (1999), "Transport properties of degenerate electrons in neutron star envelopes and white dwarf cores." A&A, 346, 345–353.

Potekhin A. Y. and Chabrier G. (2003), "Equation of State and Opacities for Hydrogen Atmospheres of Neutron Stars with Strong Magnetic Fields." ApJ, 585, 955–974.

Potekhin A. Y. and Chabrier G. (2004), "Equation of State and Opacities for Hydrogen Atmospheres of Magnetars." ApJ, 600, 317–323.

Potekhin A. Y., Chabrier G., and Ho W. C. G. (2014), "Opacities and spectra of hydrogen atmospheres of moderately magnetized neutron stars." A&A, 572, A69.

Potekhin A. Y., De Luca A., and Pons J. A. (2015a), "Neutron Stars - Thermal Emitters." Space Sci. Rev., 191, 171–206.

Potekhin A. Y., Lai D., Chabrier G., and Ho W. C. G. (2004), "Electromagnetic Polarization in Partially Ionized Plasmas with Strong Magnetic Fields and Neutron Star Atmosphere Models." ApJ, 612, 1034–1043.

Potekhin A. Y., Pons J. A., and Page D. (2015b), "Neutron Stars-Cooling and Transport." Space Sci. Rev., 191, 239–291.

Potekhin A. Y., Suleimanov V. F., van Adelsberg M., and Werner K. (2012), "Radiative properties of magnetic neutron stars with metallic surfaces and thin atmospheres." A&A, 546, A121.

Rajagopal M., Romani R. W., and Miller M. C. (1997), "Magnetized Iron Atmospheres for Neutron Stars." ApJ, 479, 347–356.

Rea N. and Esposito P. (2011), "Magnetar outbursts: an observational review." *Astrophysics and Space Science Proceedings*, 21, 247.

Rea N., Turolla R., Zane S., Tramacere A., Stella L., Israel G. L., and Campana R. (2007), "Spectral Modeling of the High-Energy Emission of the Magnetar 4U 0142+614." ApJ, 661, L65–L68.

Rea N., Viganò D., Israel G. L., Pons J. A., and Torres D. F. (2014), "3XMM J185246.6+003317: Another Low Magnetic Field Magnetar." ApJ, 781, L17.

Rea N., Zane S., Turolla R., Lyutikov M., and Götz D. (2008), "Resonant Cyclotron Scattering in Magnetars' Emission." ApJ, 686, 1245–1260.

Reisenegger A. (2001), "Magnetic Fields of Neutron Stars: an Overview." In *Magnetic Fields Across the Hertzsprung-Russell Diagram* (G. Mathys, S. K. Solanki, and D. T. Wickramasinghe, eds.), volume 248 of *Astronomical Society of the Pacific Conference Series*, 469.

Romani R. W. (1987), "Model atmospheres for cooling neutron stars." ApJ, 313, 718–726.

Ruderman M. (1972), "Pulsars: Structure and Dynamics." ARA&A, 10, 427.

Rybicki G. B. and Lightman A. P. (1979), *Radiative processes in astrophysics*. New York, Wiley-Interscience, 1979. 393 p.

Sartore N., Tiengo A., Mereghetti S., De Luca A., Turolla R., and Haberl F. (2012), "Spectral monitoring of RX J1856.5-3754 with XMM-Newton. Analysis of EPIC-pn data." A&A, 541, A66.

Schwope A. D., Hambaryan V., Haberl F., and Motch C. (2007), "The complex X-ray spectrum of the isolated neutron star RBS1223." Ap&SS, 308, 619–623.

Serkowski K. (1973), "Interstellar Polarization (review)." volume 52 of *IAU Symposium*, 145. Interstellar Dust and Related Topics.

Serkowski K., Mathewson D. S., and Ford V. L. (1975), "Wavelength dependence of interstellar polarization and ratio of total to selective extinction." ApJ, 196, 261–290.

Shabaltas N. and Lai D. (2012), "The Hidden Magnetic Field of the Young Neutron Star in Kesteven 79." ApJ, 748, 148.

Shafranov V. D. (1967), "Electromagnetic Waves in a Plasma." *Reviews of Plasma Physics*, 3, 1.

Shannon R. M. and Johnston S. (2013), "Radio properties of the magnetar near Sagittarius A* from observations with the Australia Telescope Compact Array." MNRAS, 435, L29–L32.

Shapiro S. L. and Teukolsky S. A. (1983), *Black holes, white dwarfs, and neutron stars: The physics of compact objects*. Research supported by the National Science Foundation. New York, Wiley-Interscience, 1983, 663 p.

Shibanov I. A., Zavlin V. E., Pavlov G. G., and Ventura J. (1992), "Model atmospheres and radiation of magnetic neutron stars. I - The fully ionized case." A&A, 266, 313–320.

Spruit H. and Phinney E. S. (1998), "Birth kicks as the origin of pulsar rotation." Nature, 393, 139–141.

Sturner S. J., Dermer C. D., and Michel F. C. (1995), "Magnetic Compton-induced pair cascade model for gamma-ray pulsars." ApJ, 445, 736–755.

Suleimanov V., Potekhin A. Y., and Werner K. (2009), "Models of magnetized neutron star atmospheres: thin atmospheres and partially ionized hydrogen atmospheres with vacuum polarization." A&A, 500, 891–899.

Suleimanov V. F., Pavlov G. G., and Werner K. (2012), "Magnetized Neutron Star Atmospheres: Beyond the Cold Plasma Approximation." ApJ, 751, 15.

Tauris T. M. and Manchester R. N. (1998), "On the Evolution of Pulsar Beams." MNRAS, 298, 625–636.

Taverna R., Muleri F., Turolla R., Soffitta P., Fabiani S., and Nobili L. (2014), "Probing magnetar magnetosphere through X-ray polarization measurements." MNRAS, 438, 1686–1697.

Taverna R., Turolla R., Gonzalez Caniulef D., Zane S., Muleri F., and Soffitta P. (2015), "Polarization of neutron star surface emission: a systematic analysis." MNRAS, 454, 3254–3266.

Tetzlaff N., Eisenbeiss T., Neuhäuser R., and Hohle M. M. (2011), "The origin of RX J1856.5-3754 and RX J0720.4-3125 - updated using new parallax measurements." MNRAS, 417, 617–626.

Thompson C. and Beloborodov A. M. (2005), "High-Energy Emission from Magnetars." ApJ, 634, 565–569.

Thompson C. and Duncan R. C. (1993), "Neutron star dynamos and the origins of pulsar magnetism." ApJ, 408, 194–217.

Thompson C. and Duncan R. C. (1995), "The soft gamma repeaters as very strongly magnetized neutron stars - I. Radiative mechanism for outbursts." MNRAS, 275, 255–300.

Thompson C., Lyutikov M., and Kulkarni S. R. (2002), "Electrodynamics of Magnetars: Implications for the Persistent X-Ray Emission and Spin-down of the Soft Gamma Repeaters and Anomalous X-Ray Pulsars." ApJ, 574, 332–355.

Tiengo A., Esposito P., and Mereghetti S. (2008), "XMM-Newton Observations of CXOU J010043.1-721134: The First Deep Look at the Soft X-Ray Emission of a Magnetar." ApJ, 680, L133.

Tiengo A., Esposito P., Mereghetti S., Turolla R., Nobili L., Gastaldello F., Götz D., Israel G. L., Rea N., Stella L., et al. (2013), "A variable absorption feature in the X-ray spectrum of a magnetar." Nature, 500, 312–314.

Tiengo A. and Mereghetti S. (2007), "XMM-Newton Discovery of 7 s Pulsations in the Isolated Neutron Star RX J1856.5-3754." ApJ, 657, L101–L104.

Tsai Y.-S. (1974), "Pair production and bremsstrahlung of charged leptons." *Reviews of Modern Physics*, 46, 815–851.

Turbiner A. V. and López Vieyra J. C. (2006), "One-electron molecular systems in a strong magnetic field." Phys. Rep., 424, 309–396.

Turolla R. (2009), "Isolated Neutron Stars: The Challenge of Simplicity." volume 357 of *Astrophysics and Space Science Library*, 141. Astrophysics and Space Science Library.

Turolla R., Zampieri L., Colpi M., and Treves A. (1994), "Spherical accretion onto neutron stars revisited: Are hot solutions possible?" ApJ, 426, L35–L38.

Turolla R., Zane S., and Drake J. J. (2004), "Bare Quark Stars or Naked Neutron Stars? The Case of RX J1856.5-3754." ApJ, 603, 265–282.

Turolla R., Zane S., Pons J. A., Esposito P., and Rea N. (2011), "Is SGR 0418+5729 Indeed a Waning Magnetar?" ApJ, 740, 105.

Turolla R., Zane S., and Watts A. L. (2015), "Magnetars: the physics behind observations. A review." *Reports on Progress in Physics*, 78, 116901.

Uzdensky D. A. (2011), "Magnetic Reconnection in Extreme Astrophysical Environments." Space Sci. Rev., 160, 45–71.

van Adelsberg M. and Lai D. (2006), "Atmosphere models of magnetized neutron stars: QED effects, radiation spectra and polarization signals." MNRAS, 373, 1495–1522.

van Adelsberg M., Lai D., Potekhin A. Y., and Arras P. (2005), "Radiation from Condensed Surface of Magnetic Neutron Stars." ApJ, 628, 902–913.

van Kerkwijk M. H. and Kaplan D. L. (2008), "Timing the Nearby Isolated Neutron Star RX J1856.5-3754." ApJ, 673, L163.

van Kerkwijk M. H., Kaplan D. L., Durant M., Kulkarni S. R., and Paerels F. (2004), "A Strong, Broad Absorption Feature in the X-Ray Spectrum of the Nearby Neutron Star RX J1605.3+3249." ApJ, 608, 432–443.

van Kerkwijk M. H. and Kulkarni S. R. (2001a), "An unusual Hα nebula around the nearby neutron star RX J1856.5-3754." A&A, 380, 221–237.

van Kerkwijk M. H. and Kulkarni S. R. (2001b), "Optical spectroscopy and photometry of the neutron star RX J1856.5-3754." A&A, 378, 986–995.

Ventura J. (1979), "Scattering of light in a strongly magnetized plasma." Phys. Rev. D, 19, 1684–1695.

Ventura J. and Potekhin A. (2001), "Neutron Star Envelopes and Thermal Radiation from the Magnetic Surface." volume 567 of .., 393. The Neutron Star - Black Hole Connection.

Wadiasingh Z., Baring M. G., Gonthier P. L., and Harding A. K. (2018), "Resonant Inverse Compton Scattering Spectra from Highly Magnetized Neutron Stars." ApJ, 854, 98.

Walter F. M., Eisenbeiß T., Lattimer J. M., Kim B., Hambaryan V., and Neuhäuser R. (2010), "Revisiting the Parallax of the Isolated Neutron Star RX J185635-3754 Using HST/ACS Imaging." ApJ, 724, 669–677.

Walter F. M. and Lattimer J. M. (2002), "A Revised Parallax and Its Implications for RX J185635-3754." ApJ, 576, L145–L148.

Walter F. M. and Matthews L. D. (1997), "The optical counterpart of the isolated neutron star RX J185635-3754." Nature, 389, 358–360.

Wandel A., Yahil A., and Milgrom M. (1984), "Nonadiabatic self-consistent spherical accretion as a model for quasars and active galactic nuclei." ApJ, 282, 53–60.

Weise J. I. and Melrose D. B. (2006), "Vacuum polarization in supercritical fields and at frequencies above 2m." Phys. Rev. D, 73, 045005.

Weisskopf M. C., Baldini L., Bellazini R., Brez A., Costa E., Dissly R., Elsner R. F., Fabiani S., Matt G., Minuti M., et al. (2013), "A small mission featuring an imaging x-ray polarimeter with high sensitivity." volume 8859 of Proc. SPIE, 885908. UV, X-Ray, and Gamma-Ray Space Instrumentation for Astronomy XVIII.

Weisskopf V. (1936), "The electrodynamics of the vacuum based on the quantum theory of the electron." *Kong. Dan. Vid. Sel. Mat. Fys. Med.*, 14N6, 1–39. [,206(1936)].

Whittet D. C. B., Martin P. G., Hough J. H., Rouse M. F., Bailey J. A., and Axon D. J. (1992), "Systematic variations in the wavelength dependence of interstellar linear polarization." ApJ, 386, 562–577.

Wilking B. A., Lebofsky M. J., and Rieke G. H. (1982), "The wavelength dependence of interstellar linear polarization - Stars with extreme values of lambda/max/." AJ, 87, 695–697.

Woltjer L. (1964), "X-Rays and Type I Supernova Remnants." ApJ, 140, 1309–1313.

Yakovlev D. G. and Pethick C. J. (2004), "Neutron Star Cooling." ARA&A, 42, 169–210.

Zampieri L., Turolla R., Zane S., and Treves A. (1995), "X-ray spectra from neutron stars accreting at low rates." ApJ, 439, 849–853.

Zane S., Cropper M., Turolla R., Zampieri L., Chieregato M., Drake J. J., and Treves A. (2005), "XMM-Newton Detection of Pulsations and a Spectral Feature in the X-Ray Emission of the Isolated Neutron Star 1RXS J214303.7+065419/RBS 1774." ApJ, 627, 397–403.

Zane S., Nobili L., and Turolla R. (2011a), "The magnetar emission in the IR band: the role of magnetospheric currents." *Astrophysics and Space Science Proceedings*, 21, 329.

Zane S., Rea N., Turolla R., and Nobili L. (2009), "X-ray spectra from magnetar candidates - III. Fitting SGR/AXP soft X-ray emission with non-relativistic Monte Carlo models." MNRAS, 398, 1403–1413.

Zane S. and Turolla R. (2006), "Unveiling the thermal and magnetic map of neutron star surfaces though their X-ray emission: method and light-curve analysis." MNRAS, 366, 727–738.

Zane S., Turolla R., Nobili L., and Rea N. (2011b), "Modeling the broadband persistent emission of magnetars." *Advances in Space Research*, 47, 1298–1304.

Zane S., Turolla R., Stella L., and Treves A. (2001), "Proton Cyclotron Features in Thermal Spectra of Ultramagnetized Neutron Stars." ApJ, 560, 384–389.

Zane S., Turolla R., and Treves A. (2000), "Magnetized Atmospheres around Neutron Stars Accreting at Low Rates." ApJ, 537, 387–395.

Zavlin V. E. (2009), "Theory of Radiative Transfer in Neutron Star Atmospheres and Its Applications." volume 357 of *Astrophysics and Space Science Library*, 181. Astrophysics and Space Science Library.

Zel'dovich Y. B. and Shakura N. I. (1969), "X-Ray Emission Accompanying the Accretion of Gas by a Neutron Star." Soviet Ast., 13, 175.

Zhang S. N., Feroci M., Santangelo A., Dong Y. W., Feng H., Lu F. J., Nandra K., Wang Z. S., Zhang S., Bozzo E., et al. (2016), "eXTP: Enhanced X-ray Timing and Polarization mission." In *Space Telescopes and Instrumentation 2016: Ultraviolet to Gamma Ray*, volume 9905 of Proc. SPIE, 99051Q.